DISSERTATION

submitted to the

Combined Faculties for the Natural Sciences and for Mathematics
of the Ruperto-Carola University of Heidelberg, Germany
for the degree of
Doctor of Natural Sciences

Put forward by
Dipl. Phys. Thomas Reichel
Born in Mannheim-Neckarau

Oral examination: 24.07.2013

Groundwater Degassing and Separation of Argon from Air for ^{39}Ar Dating with ATTA

Zusammenfassung

Ein Aufbau zur Wasserentgasung mittels eines kommerziellen Membrankontakors mit einer hohen, maximalen Wasserflussrate (183 L/min) und ein Aufbau zur Argonabtrennung aus Luft wurden mit dem Ziel entwickelt, Grundwasser mittleren Alters über ^{39}Ar-Messungen mit ATTA (atom trap trace analyis) zu datieren. Für die Entgasungsanlage wurden Entgasungseffizienzen für verschiedene Elemente und Isotope bestimmt (etwa 88 % für Sauerstoff, 84 % für Helium, 87 % für Neon, 90 % für Argon, 87 % für Krypton, and 82 % für Xenon). Der Aufbau zur Abtrennung von Argon ähnelt dem von Riedmann [2011] entwickelten und besteht hauptsächlich aus neun gaschromatographischen, parallel geschalteten Säulen, die mit Zeolith Li-LSX als selektivem Adsorptionsmaterial gefüllt sind, und aus einem Quadrupolmassenspektrometer, welches die Zusammensetzung des aus den Säulen herausströmenden Gases misst. Proben von mehr als 63 LSTP Luft können in einem Durchgang separiert werden. Temperaturen zwischen -130 and -135°C erwiesen sich für die stark temperaturabhängige Argonabtrennung als am günstigsten. Die erreichte Argonreinheit liegt zwischen 98 und 99.6 % und die Ausbeute zwischen 96.5 und 99.2 %. Isotopenfraktionierungen, welche das ^{39}Ar/^{40}Ar-Verhältnis und somit das ^{39}Ar-Alter verzerren würden, sind sowohl bei der Entgasung als auch bei der Separation vernachlässigbar klein. Erste Proben wurden in Feldeinsätzen genommen, separariert, und mit ATTA datiert.

Abstract

A setup for water degassing employing a commercial membrane contactor with high maximum water flow rate (183 L/min) and a setup for argon separation from air were developed, with the aim of dating groundwaters of intermediate age with ^{39}Ar, using atom trap trace analysis (ATTA). For the degassing setup, degassing efficiencies for different elements and isotopes were determined (around 88 % for oxygen, 84 % for helium, 87 % for neon, 90 % for argon, 87 % for krypton, and 82 % for xenon). The setup for argon separation is similar to the one constructed by Riedmann [2011] and consists mainly of nine gas chromatographic columns installed in parallel and filled with zeolite Li-LSX as selective adsorbent, and a quadrupole mass spectrometer to observe the composition of the gas leaving the columns. Samples of more than 63 LSTP air can be separated in one run. The argon separation strongly depends on temperature, with temperatures between -130 and -135°C being the most favorable. Argon purities ranging from 98 to 99.6 % and argon recoveries between 96.5 and 99.2 % are achieved. Isotope fractionation during degassing and separation, which could change the ^{39}Ar/^{40}Ar ratio and hence distort the ^{39}Ar age, is negligible. First samples were taken in the field, separated, and dated with ATTA.

Contents

Chapter 1

Introduction

Sustainable management of freshwater resources and the adaption to climate change are some of the most pressing challenges to mankind, as these are the main influence factors on economic and food security. Groundwater is a primary source of fresh water in many parts of the world, with some regions becoming overly dependent on it and consuming the groundwater faster than it is naturally replenished [Rodell et al., 2009]. The increasing depletion of massively exploited groundwater systems is observed in numerous highly-productive agricultural areas, mainly as a result of water abstraction for irrigation purposes. For example, the groundwater of the Indian states Rajasthan, Punjab, and Haryana was depleted at a mean rate of (4 ± 1) cm/year equivalent height of water between August 2002 and October 2008, resulting in a total net groundwater loss of $109 \, \mathrm{km}^3$ for that period (which is double the capacity of India´s largest surface-water reservoir) [Rodell et al., 2009]. From October 2003 to March 2010, California´s Central Valley lost groundwater at a rate of (2.0 ± 0.4) cm/year and $20.3 \, \mathrm{km}^3$ in total [Famiglietti et al., 2011]. In portions of the Tigris and Euphrates River Basins and western Iran, the rate of groundwater loss was (1.7 ± 0.2) cm/year between January 2003 and December 2009, which means a total groundwater loss of $(91.3 \pm 10.9) \, \mathrm{km}^3$ [Voss et al., 2013]. In the parts of North China investigated by Feng et al. [2013], the groundwater depletion was (2.2 ± 0.3) cm/year between 2003 and 2010, which is equivalent to $(8.3 \pm 1.1) \, \mathrm{km}^3$/year.

Groundwater models can help to manage the exploitation of water reservoirs in a sustainable way. These models have to be calibrated by use of isotope and chemical tracers. The tracer age is the quantity which is directly measured, and which, under favorable conditions, represents the groundwater age [Zuber et al., 2011]. The groundwater age is directly measurable only by tracer methods and is generally defined as the time span since the last contact of water with the atmosphere [Zuber et al., 2011]. Dating can be based on production rate, input function, and/or decay of the tracer. Ranges and types of selected environmental tracers were compiled by Newman et al. [2010] and are shown in Figure 1.1. In the important range of 50-1000 years, covering environmental processes such as deep ocean circulation, vertical mixing of lakes, and recharge of groundwaters of intermediate age, the radioactive ^{39}Ar (half life 269 years) is the only reliable water age tracer. As a noble gas isotope, degradation and sorption are of minor importance. Since only the ratio of ^{39}Ar to the stable ^{40}Ar is required for dating, ^{39}Ar is insensitive to excess air, degassing, or incomplete gas extraction yield [Loosli et al., 2001; Corcho Alvarado et al., 2007]. It proves being exceedingly helpful in oceanographic multi-tracer studies (for ex-
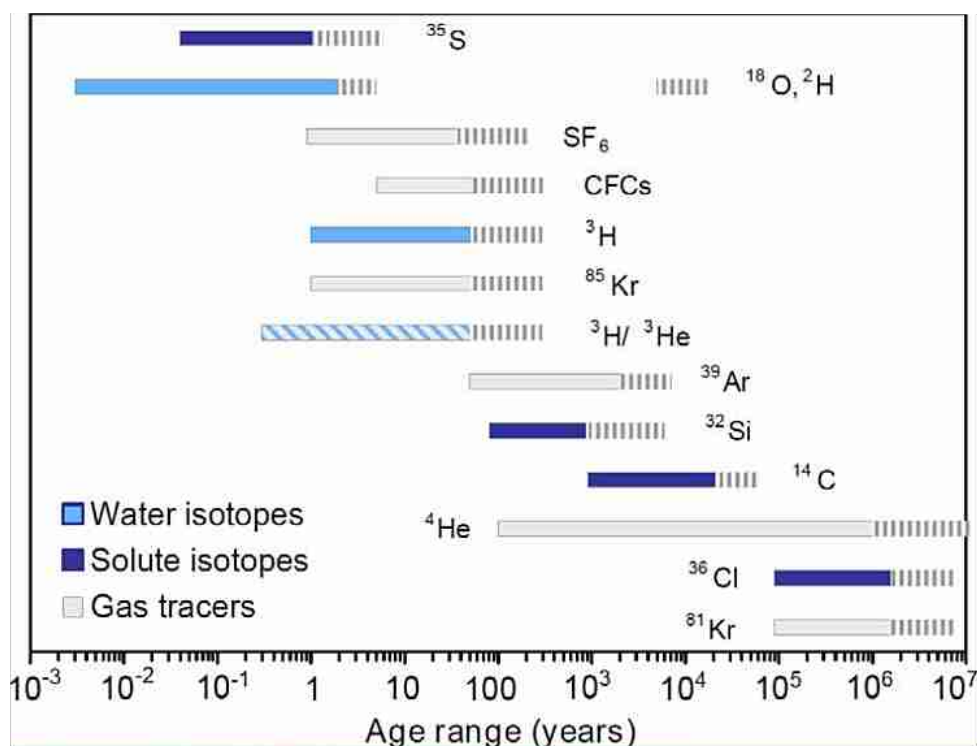
Figure 1.1: Time ranges and types of selected environmental tracers, taken from Newman et al. [2010].

ample [Loosli, 1989; Schlosser et al., 1994, 1995; Collon et al., 2004]) and enables constraining the age groundwaters of intermediate age as well as mixing of different groundwaters (for example [Loosli, 1983; Forster et al., 1983; Loosli, 1992; Purtschert et al., 2001; Corcho Alvarado et al., 2007; Sültenfuss et al., 2011]. In the study of Nolte et al. [2006], argon was extracted from biotites separated from Hiroshima granite samples. Then, by measuring the ^{39}Ar activity produced by the capture of the fast neutrons from the A-bomb on potassium, the neutron dose to the survivors could be determined. Another field of application is the background determination of the argon detectors for WIMP (Weakly Interacting Massive Particles). These consist of around 10 tons of liquid argon, which is in particular an excellent material for use as a detector of ionizing particles [Galbiati et al., 2008].

However, due to the extremely low isotopic abundance of ^{39}Ar of around $8 \cdot 10^{-16}$ in the atmosphere and the long half life, the detection demands efforts. Currently, the detection of ^{39}Ar is only practical by radioactive low-level decay-counting (LLC) in the subsurface laboratory of the university of Bern [Sültenfuss et al., 2011], requiring 0.3-2 LSTP of argon and to degass around 1-5 tons of water in the field and taking up to 6 weeks measurement time [Loosli, 1983]. Because of the great efforts in the field and laboratory, the number of ^{39}Ar determinations is often restricted to few samples (see Forster et al. [1983]). Collon et al. [2004] reduced the required argon volume to 2 ccSTP by employment of accelerator mass spectrometry (AMS) using the Argonne ATLAS heavy ion accelerator in combination with a gas-filled magnetic spectrograph, counting atoms instead of decays and reducing the time required for the measurements to around 8 h. However, further application of this technique has been difficult due to its dependence on the use of a large accelerator, of which access (beam time) is limited [Jiang et al., 2011]. A promising

new measurement technique is atom trap trace analysis (ATTA), where single atoms are trapped by magneto-optical forces with extremely high selectivity and are detected via their fluorescence light. For ^{81}Kr, the applicability of ATTA has been demonstrated by Sturchio et al. [2004], who dated 210000 - 1000000 year old groundwater below the Sahara. Recently, the Heidelberg ATTA group reached sufficiently high ^{39}Ar counting rates to enable the dating of groundwaters of intermediate age. This thesis is about developing and testing a setup for groundwater degassing and a setup for argon separation from degassed air, in order to establish together with the ATTA group a line for ^{39}Ar dating in Heidelberg as alternative to LLC in Bern.

Chapter 2

Theory

2.1 Water Dating with ^{39}Ar

2.1.1 Argon – Production and Abundance

After nitrogen and oxygen, the noble gas argon is the third most abundant gas in dry atmospheric air (see Table 2.1 for elemental and isotope abundances). While ^{36}Ar and ^{38}Ar are primordial, ^{40}Ar is produced in the silicate Earth (crust and mantle) by radioactive decay of ^{40}K and released to the atmosphere over the history of Earth [Sano et al., 2013]. The atmospheric inventory comprises approximately half of the total ^{40}Ar produced by potassium decay over Earth history, assuming the canonical value of 240 ppm for the K content of the bulk silicate Earth [Bender et al., 2008]. The modern outgassing rate $(1.1 \pm 0.1) \, 10^8$ mol/a was determined by Bender et al. [2008] by measuring the ^{40}Ar/^{38}Ar ratio of fossil air from up to 779 ka old ice core samples. However, the rate of increase of the atmospheric ratio of (0.066 ± 0.007) ‰/Ma is far too low to affect ^{39}Ar dating. The radioactive isotopes ^{37}Ar (half life 35.1 d) and ^{39}Ar (half life 269 a) are produced by neutron induced reactions [Porcelli et al., 2002]. ^{37}Ar, originating from the ^{40}Ca(n,α)^{37}Ar reaction, has natural and anthropogenic (underground nuclear tests) sources. Applications as tracer are the investigation of atmospheric circulation and mixing [Loosli, 1992] or the verification of the Comprehensive Nuclear-Test-Ban Treaty [Riedmann, 2011]. ^{39}Ar has predominantly natural sources [Florkowski and Rozanski, 1986] and is produced in the stratosphere by cosmic-ray secondary neutrons with energies higher than 12.8 MeV via the ^{40}Ar(n,2n)^{39}Ar reaction (neutrons in rocks have lower energies) [Andrews et al., 1989]. Sub-surface ^{39}Ar-production can result from ^{38}Ar(n,γ)^{39}Ar, ^{42}Ca(n,α)^{39}Ar, and ^{39}K(n,p)^{39}Ar reactions [Andrews et al., 1989], with the last reaction being the main source in normal granite [Forster et al., 1983]. The neutrons originate from the spontaneous fission of U and the (α,n) reactions within the rock matrix of the α-particle emitted by natural decay series of U and Th [Loosli et al., 1989]. Hence, the sub-surface production is affected by the abundance and spatial distribution of uranium and thorium in the rock matrix. In addition, it scales with the concentration of the target nuclei (K, Ca) and the mean free path of the neutrons, which is inversely proportional to the concentration of adsorbing elements in the rock [Loosli

Constituent	Volume Mixing Ratio	Isotopes	Relative Abundances
N_2	0.781		
O_2	0.209		
Ar	$(9.34\pm0.01)\cdot10^{-3}$	^{36}Ar (stable)	$(3.384\pm0.006)\cdot10^{-3}$
		^{37}Ar (35.1 d)[1]	
		^{38}Ar (stable)	$(6.36\pm0.02)\cdot10^{-4}$
		^{39}Ar (269 a)[1]	$8.1\cdot10^{-16}$
		^{40}Ar (stable)	$\equiv1$
Ne	$(1.818\pm0.004)\cdot10^{-5}$	^{20}Ne (stable)	9.80 ± 0.08
		^{21}Ne (stable)	$(2.90\pm0.03)\cdot10^{-2}$
		^{22}Ne (stable)	$\equiv1$
He	$(5.24\pm0.05)\cdot10^{-6}$	^{3}He (stable)	$(1.399\pm0.013)\cdot10^{-6}$
		^{4}He (stable)	$\equiv1$
Kr	$(1.14\pm0.01)\cdot10^{-6}$	^{78}Kr (stable)	0.6087 ± 0.020
		^{80}Kr (stable)	3.9599 ± 0.0020
		^{81}Kr ($2.1\cdot10^{5}$ a)[1]	
		^{82}Kr (stable)	20.217 ± 0.004
		^{83}Kr (stable)	20.136 ± 0.021
		^{84}Kr (stable)	$\equiv100$
		^{85}Kr (10.76 a)[1]	
		^{86}Kr (stable)	30.524 ± 0.025
Xe	$(8.7\pm0.1)\cdot10^{-8}$	^{124}Xe (stable)	2.337 ± 0.008
		^{126}Xe (stable)	2.180 ± 0.011
		^{128}Xe (stable)	47.15 ± 0.07
		^{129}Xe (stable)	649.6 ± 0.9
		^{130}Xe (stable)	$\equiv100$
		^{131}Xe (stable)	521.3 ± 0.8
		^{132}Xe (stable)	660.7 ± 0.5
		^{134}Xe (stable)	256.3 ± 0.4
		^{136}Xe (stable)	217.6 ± 0.3

Table 2.1: Noble gas isotope composition of the (dry) atmosphere after Porcelli et al. [2002] and Florkowski and Rozanski [1986][1].

et al., 1989; Corcho Alvarado et al., 2007]. The ^{39}Ar activity in groundwater originating from sub-surface production depends furthermore on the escape rate of ^{39}Ar from the rock into the water phase [Loosli et al., 1989; Corcho Alvarado et al., 2007]. In an average granite, escape factors of 0.4 % were found to be typical [Lehmann and Purtschert, 1997]. The part of the underground produced ^{39}Ar in groundwater seems to mainly originate from the fracture fillings, as Lehmann and Purtschert [1997] found lower overall escape factors for the produced ^{39}Ar in a system with lower potassium concentration in the fillings than in the bulk material. Sub-surface production is particularly present in groundwaters from crystalline and Permian formations [Loosli, 1992]. ^{39}Ar can only be used for groundwater dating where measurements and/or calculations have shown that the sub-surface produced ^{39}Ar activity is small compared to the atmospheric cosmic-ray produced content [Loosli et al., 2001]. For example, this can be done by analyzing drill core samples for U, Th, and K [Forster et al., 1983]. When there are water samples from the investigated aquifer having ^{39}Ar activities below 5 % modern, the sub-surface production is probably negligible [Loosli, 1992].

2.1.2   Dating with ^{39}Ar

This section introducing dating with ^{39}Ar is based mainly on Loosli [1983] and Loosli et al. [1989].

^{39}Ar is a radioactive isotope with an half-life $\tau_{1/2}$ of 269 years, which is produced by cosmic rays in the stratosphere by the ^{40}Ar(n,2n)^{39}Ar process. Based on observed ^{14}C fluctuations in tree rings over the last 1000 years, the corresponding variations during that time interval in the atmospheric ^{39}Ar/^{40}Ar ratio were estimated to be up to 7 %, which is practically negligible for usual dating purposes. Since the exchange times between the stratosphere and the troposphere and between the hemispheres are relatively short compared to $\tau_{1/2}$, there is a homogeneous ^{39}Ar concentration in the troposphere which is defined as "100 % modern". By measuring tropospheric air samples taken in 1940, 1959, 1961, 1971, 1974, 1975 and 1979, an upper limit of 5 % modern was found for the anthropogenic contributions from nuclear tests and nuclear industry. This can also be neglected. As a noble gas, argon is not involved in any chemical reactions and can be regarded as an ideal conservative tracer in the sense that there are no sinks or sources and that the tracer moves together with the water. However, in aquifers in granite rock formations there can be significant contributions from ^{39}K(n,p)^{39}Ar reactions, with the neutron mainly being produced by (α,n) reactions. Beside this exception, ^{39}Ar is well suited to date ice, ocean water, or groundwater in the range of around 50-1000 years. Section 2.1.4 addresses to the different measurement techniques coping with the extremely low atmospheric ^{39}Ar/^{40}Ar ratio of around 10^{-15}.

As for other radioactive isotopes produced by cosmic rays, the ^{39}Ar/^{40}Ar ratio starts decreasing when the argon is sealed off from the atmosphere and the replenishment of ^{39}Ar ends. This happens for example, when air is enclosed in firn, air is dissolved in water of the groundwater recharge area of a confined aquifer, or air equilibrated ocean water sinks below the mixed layer (the estimated mean residence time for argon in the mixed ocean layer of around 1 month can be neglected compared to its half-life). Once sealed off, the initially enclosed amount $n_{39}(0)$ of ^{39}Ar (from time t=0) follows the radioactive decay curve, reaching the amount $n_{39}(t)$ after time

t:

$$n_{39}(t) = n_{39}(0) \cdot \exp(-t/\tau), \tag{2.1}$$

with the mean lifetime $\tau = \tau_{1/2}/\ln(2)$. It is often beneficial to measure with respect to an established standard. The atmospheric $^{39}Ar/^{40}Ar$ ratio $R_{39/40}^{atm}$ is well-known and has not changed significantly in the last 1000 years, making it the perfect standard. The amount n_{40} of enclosed ^{40}Ar atoms does not change over time (no decay, negligible subsurface production rate), and the equation above can be written in terms of $R_{39/40}^{atm}$ simply by dividing by n_{40}:

$$R_{39/40}(t) = \frac{n_{39}(t)}{n_{40}} = \frac{n_{39}(0)}{n_{40}} \cdot \exp(-t/\tau) = R_{39/40}^{atm} \cdot \exp(-t/\tau). \tag{2.2}$$

The time t since enclosure is then simply:

$$t = \tau \cdot \ln\left(R_{39/40}^{atm}/R_{39/40}(t) \right). \tag{2.3}$$

2.1.3 Maximally Acceptable Sample Contamination

For the component selection and to assess leak rates, it is essential to know which relative contamination of the sample with ambient air still can be tolerated. Since $R_{39/40}(t)$ is at best 10^{-15}, one can use the following approximations:

$$n_{40} = n_{Ar} - n_{39} \approx n_{Ar} \qquad \text{and} \qquad R_{39/40}(t) = \frac{n_{39}(t)}{n_{40}} \approx \frac{n_{39}(t)}{n_{Ar}}, \tag{2.4}$$

with the total amount n_{Ar} of argon. Having a sample (index s, age t) with a relative contamination of $x\,\%$ (index c, age 0), the $^{39}Ar/^{40}Ar$ ratio of the contaminated sample becomes:

$$R_{39/40}(t) = \frac{(1-x) \cdot n_{39,s} + x \cdot n_{39,c}}{(1-x) \cdot n_{40,s} + x \cdot n_{40,c}} \approx (1-x) \cdot R_{39/40}^{atm} \cdot \exp(-t/\tau) + x \cdot R_{39/40}^{atm}. \tag{2.5}$$

The apparent age t' of the contaminated sample is:

$$t' = -\tau \cdot \ln\left((1-x) \cdot \exp(-t/\tau) + x \right). \tag{2.6}$$

Deviations $(t\text{-}t')$ from the true sample age t are listed in Table 2.2 for different t and different relative contaminations with ambient air. Even for relative contaminations of $2\,\%$ the deviations are still small compared to the typical statistical errors for low level counting.

2.1.4 Measurement of ^{39}Ar

Low Level Counting (LLC) Since more than 30 years argon samples have been measured in the subsurface laboratory of the university of Bern/Switzerland by detecting the ^{39}Ar-β-activity using high-pressure proportional gas counters (10–30 bar). To reduce the background, the laboratory is situated 30 m below ground and built of specially selected concrete having a low radioactivity. In addition, the counters are surrounded by a layer of lead, with an extra layer

Relative Contamination	True Sample Age [years]						
with Ambient Air [%]	50	100	250	400	600	800	1000
0.1	0.1	0.1	0.4	0.7	1.4	2.7	4.7
0.2	0.1	0.2	0.7	1.4	2.9	5.3	9.3
0.5	0.3	0.6	1.8	3.5	7.1	13.1	22.9
1	0.5	1.1	3.5	6.9	14.1	25.7	44.5
2	1.1	2.3	7.0	13.7	27.7	49.9	84.4
5	2.7	5.7	17.2	33.5	65.8	114.4	184.3
10	5.3	11.2	33.6	64.3	122.0	202.7	308.7
Typical LLC Errors [years]	20		30		80		

Table 2.2: The deviations from the true sample age (in years) for different sample ages and different relative contaminations with ambient air. The last line lists typical statistical errors for low level counting (LLC), taken from Loosli et al. [1989].

separating the main counter from the anticoincidence counter. The statistical error is about 7 % for samples in the optimal dating range of a few hundred years. Further uncertainties such as memory effects or not perfect stability and reproducibility of the equipment are reduced by frequent blank measurements, external calibration of the proportional counters with γ-sources every other day, spectrum identifications, and statistical tests of the read-out during a series of measurements [Loosli, 1983]. Samples sizes range from 0.3–2 LSTP argon, requiring to degas 1–5 m^3 of water and involving measurement times between 1 and 6 weeks. For dating ocean water or glacier ice with ^{39}Ar, the required sample size is too large. Another complication is that krypton has to be separated preferably completely from the argon fraction, as the ^{85}Kr activity per volume of modern air is about 40 times larger than the ^{39}Ar-activity [Loosli, 1989]. ^{85}Kr and ^{39}Ar are both β^- emitters with similar beta energy and therefore indistinguishable by proportional counting.

Accelerator Mass Spectrometry (AMS)

According to Lu and Wendt [2003], compared to LLC, mass spectrometry (MS), which separates and detects individual atoms of a chosen charge-to-mass ratio, has the advantage of potentially counting all atoms and not only the decaying portion. For long-lived isotopes such as ^{39}Ar this is a huge improvement. Instead of the radioactive background, the background of atoms with nearly identical charge-to-mass ratios matters, limiting the detection via MS to isotopic abundances higher than 10^{-9}. AMS extends this limit by additional discriminations and by performing MS at higher energies (several MeV). Isotopes such as ^{10}Be, ^{14}C, ^{26}Al, ^{36}Cl, ^{41}Ca, and ^{129}I are commonly analyzed with AMS employing tandem accelerators. In the first acceleration stage, atomic isobars are removed by exploiting the stability of the negatively charged ions (for example ^{14}C$^-$ is stable, whereas ^{14}N$^-$ is not). During the second stage of acceleration, when the accelerated beam passes through a thin foil to strip away some electrons, molecules disintegrate and molecular isobars are consequently filtered out. For high-energy ions, energy-loss measurements can be applied for further discrimination. However, noble gases do not form negatively charged ions and can not be analyzed using tandem accelerators. Collon et al. [2004] employed a high energy linear accelerator (the Argonne ATLAS heavy ion accelerator)

and separated ^{39}Ar from ^{39}K by acceleration of ^{39}Ar^{8+} ions to 232 MeV and using a gas-filled spectrograph as final step of discrimination. With AMS, the counting time is reduced to around 8 h and the sample size to around 2 ccSTP.

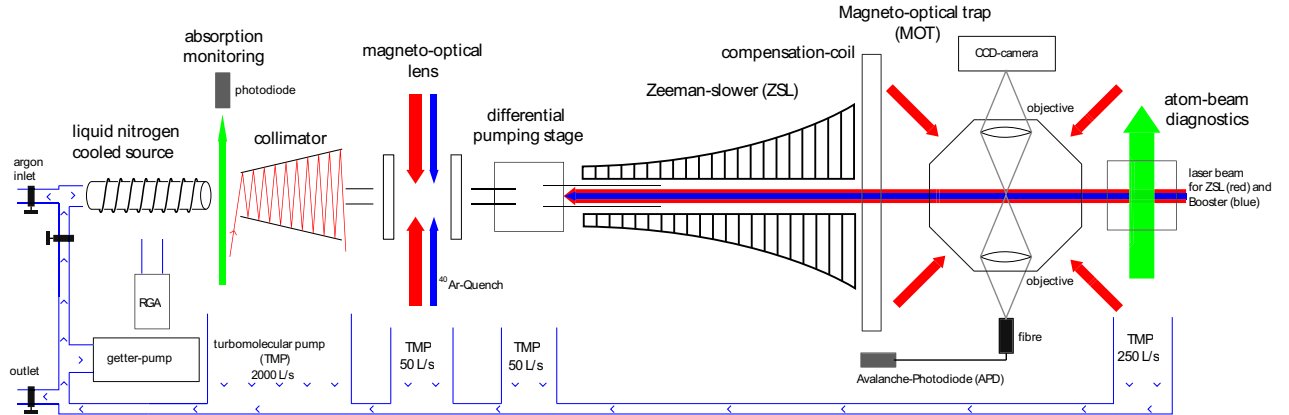**Atom Trap Trace Analysis (ATTA)**

Figure 2.1: The ATTA setup of the Heidelberg group, taken from Ebser [2012].

An upcoming alternative is the tabletop sized atom trap trace analysis – a measurement technique, whose acquisition cost is several orders of magnitude less than that of AMS. Like in AMS, potentially all atoms can be detected and not only the decaying portion as for LLC, which is a huge advantage for detection of the long-lived ^{39}Ar. Small differences in the atomic transition frequency between isotopes of the same element are exploited to trap a selected isotope by magneto-optical forces and detect it by fluorescence light, without the interferences from any other isotopes, isobars, atomic or molecular species [Lu et al., 2012]. The superior selectivity arises from the fact that numerous scattering events of the isotope with photons of the resonance frequency of a chosen transition are required to slow down, trap, and detect the isotope. ATTA was first developed by Chen et al. [1999], detecting ^{81}Kr and ^{85}Kr. Sturchio et al. [2004] dated up to 1 million year old groundwater applying ATTA to ^{81}Kr measurements. For ^{39}Ar, all laser frequencies necessary for the implementation of ATTA were firstly determined by Welte et al. [2009] by hyperfine spectroscopy of the 1s$_5$-2p$_9$ transition of ^{39}Ar. In a short-term experiment, Jiang et al. [2011] showed for the first time that ^{39}Ar from modern air samples can be detected with ATTA.

The functional principle is explained on the basis of the Heidelberg ATTA setup displayed in Figure 2.1 and described in Welte [2011]. Metastable atoms, which are required for atom optical manipulation, are produced in a radio-frequency driven gas discharge ("the source"). The beam of metastable atoms emerging from the source is collimated and focused on the magneto-optical trap (MOT). Then, the atoms are transversally slowed by a magneto-optical lens to further reduce the divergence and longitudinally decelerated by a Zeeman slower, as the MOT can only trap atoms with a certain maximum velocity. The measurements are then performed by fluorescence detection of single ^{39}Ar atoms in the trap. The ^{39}Ar count rate $\dot{N}_{det}$ is given by Welte et al. [2010]:

$$\dot{N}_{det} = I^* \cdot R \cdot \eta_{coll} \cdot \eta_{ZS} \cdot \eta_{MOT} \cdot \eta_{HFS} \cdot \Delta\Omega_{MOT} \,, \tag{2.7}$$

where I^* is the metastable beam intensity, R the isotopic ratio in a recent sample, η_{coll} the collimation enhancement, η_{ZS} the Zeeman slower efficiency, η_{MOT} the estimated MOT capture efficiency, η_{HFS} the reduction factor due to hyperfine ground state splitting to five levels and only repumping from one, and $\Delta\Omega_{MOT}$ the solid angle covered by the MOT.

For a high $\dot{N}_{det}$, a high I^* is required, and thus a high purity of the separated argon, a high production of metastable atoms, and a high sample throughput of the ATTA vacuum system. However, to reduce collisional losses due to background gas, a vacuum level of at least $2 \cdot 10^{-5}$ mbar has to be maintained at the trap chamber. The Heidelberg ATTA group implemented the high throughput by installing a 200 l/s turbo molecular pump at the source chamber and by realizing a steep pressure gradient between the sample reservoir (10^{-2} mbar) and the MOT chamber ($\sim 10^{-8}$ mbar) by several differential pumping stages (see Figure 2.1).

An improvement of the Heidelberg ATTA setup is the employment of an additional near-resonant sideband of the Zeeman slower laser beam, enabling higher final velocities of the Zeeman slower and effectively increasing the longitudinal velocity capture range of the trap. This further reduces the divergence of the beam and increases the loading rate of the trap. The source of the metastable atoms is liquid nitrogen cooled to reduce the thermal velocity of the atoms. Additionally, metastable ^{40}Ar atoms, which are also produced in the source, are optically pumped back to the ground state, which eliminates the fluorescence background of these atoms in the MOT. A getter pump prevents degradation of the sample gas due to outgassing from the vacuum chambers when operating in recycling mode. In principle, recycling of the sample would be possible, effectively reducing the required sample size to less than 1 ccSTP. So far background effects resulting from the tests performed with argon highly enriched in ^{39}Ar make this impossible.

As explained, ATTA basically can tolerate all kinds of sample contamination from other isotopes or elements due to its high selectivity. However, the counting rate $\dot{N}_{det}$ is proportional to the beam intensity I^* of metastable argon atoms, which is proportional to the purity of the argon sample as the excitation efficiency depends on the purity. Hence, it is important for the setup for argon separation developed in this work to achieve a high argon purity.

2.2 Other Age Tracers employed in this Study

For the determination of groundwater age, i.e. the time elapsed since infiltration of the water, beside ^{39}Ar, the radioactive age tracers Tritium (^{3}H) and ^{14}C were employed in this thesis. Using ^{3}H to identify young groundwaters (<50 years) and ^{14}C for groundwaters older than 1000 years, the range covered by ^{39}Ar (50-1000 years) is complemented. ^{3}H and ^{14}C were employed qualitatively in the sense of "tendentially younger" or "tendentially older". Hence, only the required basics regarding these tracers are treated in the following, summarizing the theory compiled by Mook and de Vries [2001].

2.2.1 Tritium

Tritium (^{3}H) is naturally produced by cosmic rays in the upper atmosphere in the ^{14}N(n,^{3}H)^{12}C reaction. It is a radioactive isotope with a half-life of 12.32 years and purely decays by β^-

emission to ^{3}He. Its activity is typically given in Tritium Units ($1\,TU = 0.118Bq/L$). In the 1960s, due to the nuclear bomb tests, the tritium contents of precipitation increased a 1000-fold in the northern hemisphere. A large part of the tritium produced this way has been injected into the stratosphere and returns to the troposphere each year during spring and early summer. This explains the highly variable ^{3}H content of precipitation in the northern hemisphere (see Figure 2.2), which decreases slower than what would be expected after the residence time of H_2O in the troposphere of some weeks, to which ^{3}H is coupled. As for ^{39}Ar, the radioactive decay law is used for dating (compare Equation 2.1). However, unlike for ^{39}Ar (whose initial activity has been constant over the last 1000 years), no unambiguous assignment of an initial activity and thus age is possible from tritium analysis. Due to the variability of the input function, extrapolation of the measured tritium concentration often results in several possible water ages. Nevertheless, if a measurable ^{3}H activity (large than $1\,TU$) was determined for a water sample, the water is surely either younger than 50 years or a mixture of young and old water. By additionally measuring the daughter nuclide ^{3}He, the initial tritium concentration can be calculated from the sum of the ^{3}H and ^{3}He concentration. Tritium-^{3}He dating leads to much more precise water ages than the determination of tritium alone. Nevertheless, in the scope of this work only the tritium content was considered, as no precise dating of young groundwater was necessary.
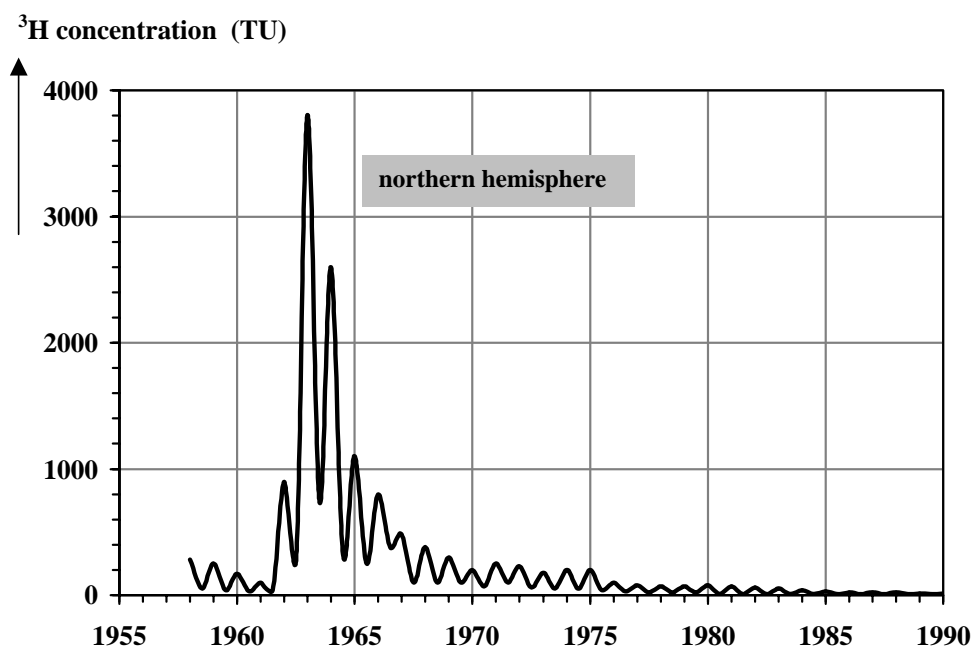
Figure 2.2: Smoothed curve of the average tritium concentration of precipitation over the continental surface in the northern hemisphere (taken from Mook and de Vries [2001]).

2.2.2 ^{14}C

Originating from the ^{14}N(n,p)^{14}C reaction, ^{14}C is naturally produced in the upper atmosphere by cosmic rays and very soon oxidized to ^{14}CO$_2$. It decays by β^- emission to ^{14}N and has a half-life of 5730 years. Longterm variability of the cosmic ray intensity and climate effects on

the size of the carbon reservoirs lead to a variability of its initial atmospheric activity over long time scales. This is corrected for by calibration with ^{14}C contents in tree rings of well known age. Like for tritium, the bomb tests in the 1960s caused the atmospheric ^{14}C concentration to increase, reaching twice the natural concentration at the peak maximum in 1963. Due to exchange with the ocean, it slowly decreases to the natural level. For groundwater dating, the anthropogenically produced ^{14}C is only important when mixing between old and young water occurs, as the tracer's dating range is around 1000 to 30000 years. Often the conventional ^{14}C age is given, which is the calculated age after the radioactive decay law (compare Equation 2.1) using the original (wrong) Libby half-life of 5568 years and expressed in years before 1950 (and without calibration). By calibration with tree ring data, this age can be converted to the correct age. However, isotope fractionation can further complicate dating with ^{14}C. In groundwaters, the matrix exchange with ^{14}C free carbonates can dilute the ^{14}C concentration. The stable isotope ^{13}C can be used to trace the fractionation, but the reliability of the obtained age depends on how well the carbon system in the individual aquifer is understood [Loosli et al., 2001]. The simplest model accounting for carbonate exchange issues from Vogel [1970]. If the measured isotope fractionation for ^{13}C from the well known value in the soil air is the same for the entire aquifer, a bias for the ^{14}C concentration and hence the age is assumed. Exact groundwater dating with ^{14}C is difficult. However, in this thesis it is only employed for the identification of old waters or mixing with old waters.

2.3 Noble Gas Temperature

The reconstruction of past climate conditions is essential for placing recent observed climate changes in a longer term context [Corcho Alvarado et al., 2009]. However, due to the lack of instrumental climate records before the mid 19*th* century, one has to draw on natural climate archives. Noble Gas Temperature (NGT) is a measure of the soil temperature during infiltration of groundwater and is related to the surface air temperature. Having a low temporal resolution, NGT records can be used to estimate local low-frequency temperature variations, but not decadal variability [Corcho Alvarado et al., 2009]. This section treats the theory on which NGT is based, starting with Henry´s law.

2.3.1 Henry´s Law

The partitioning of a gas between a gas phase and a water phase depends on temperature and salinity and is described by Henry´s law. For a given temperature, the relation between the concentration of dissolved gas in water and the concentration of the gas in the atmosphere above the water is linear. Depending on in which units the gas amount in the respective phase is expressed (partial pressure, volumetric or gravimetric concentration, mole fraction), the value of the proportionality constant varies. This short introduction uses the same terms as Aeschbach-Hertig [2004], who gives a more complete overview of the different solubility coefficients and their conversions. When the gas concentrations in the gas phase (C_g) and in the water phase (C_w) are expressed in $\mathrm{mol\,L^{-1}}$, the Henry constant K_H is "dimensionless" ($\frac{mol/L_g}{mol/L_w}$) and Henry´s

law reads:

$$C_g = K_H \cdot C_w = \frac{1}{L} \cdot C_w \,, \tag{2.8}$$

with the Ostwald-solubility L, which is the inverse of K_H. Another way to formulate Henry´s law is using the partial pressure p in atm of the gas above the liquid:

$$p = k \cdot C_w = \frac{1}{K} \cdot C_w \,, \tag{2.9}$$

with the Henry constant k and the Ostwald-solubility K, which is again the inverse of the Henry constant. A relation between k, and K_H can be deduced using the ideal gas law:

$$k = \frac{p}{C_w} = \frac{C_g \cdot RT}{C_w} = K_H \cdot RT, \tag{2.10}$$

with the ideal gas constant R, the temperature T in Kelvin, and the water concentrations still in $\mathrm{mol\,L^{-1}}$. Another form of expressing dissolved equilibrium concentration in water, which is used in some of the papers on noble gas solubilities cited in this work ([Weiss, 1970, 1971; Weiss and Kyser, 1978]), is the atmospheric equilibrium concentration C^* in units of ccSTP/kg. It specifies the amount of gas dissolved in one kg of water in equilibrium with air when the atmospheric pressure above the water is one atmosphere. A conversion to the dimensionless Henry coefficient K_H can be achieved the following way:

$$C_w[ccSTP/kg] = \frac{p}{(P_{St} - p_v) \cdot x_g} \cdot C^* = \frac{C_g[mol/L_g] \cdot RT}{(P_{St} - p_v) \cdot x_g} \cdot C^* \,, \tag{2.11}$$

with the water vapor p_v, the standard pressure $P_{St} = 1013.25\,\mathrm{mbar} = 1\,\mathrm{atmosphere}$, the partial pressure p of the gas, and its volume or mole fraction x_g in air. The relation between $C_w[ccSTP/kg]$ and $C_w[mol/L_w]$ is just:

$$C_w[ccSTP/kg] = \frac{C_w[mol/L_w] \cdot RT_{St}}{P_{St} \cdot \rho_w} \,, \tag{2.12}$$

with the water density ρ_w and standard temperature $T_{St} = 273.15\,\mathrm{K}$. The dimensionless Henry coefficient reads:

$$K_H = \frac{C_g[mol/L_g]}{C_w[mol/L_w]} = \frac{(P_{St} - p_v) \cdot x_g}{P_{St} \cdot \rho_w \cdot C^*} \cdot \frac{T_{St}}{T} \,. \tag{2.13}$$

2.3.2   Noble Gas Temperature (NGT)

According to Henry´s law, which was introduced in the last section, the concentration of a gas dissolved in water is linearly proportional to the partial pressure of that gas above the water. The proportionality constant, regardless of the form Henry´s law is expressed in, depends on temperature and salinity. For a given gas concentration, in principle, the groundwater recharge temperature (or NGT) can be calculated using this proportionality, if the salinity and the partial pressure at the place of recharge are known. Only the noble gases (He, Ne, Ar, Kr, and Xe) are suited for this purpose, as they are chemically inert and have well known sources and sinks.

Recharge altitude (i.e. partial pressure) and salinity at recharge location are assumed, and subsurface produced radiogenic ^{40}Ar is subtracted in order to obtain the gas concentration in the water at the recharge [Loosli et al., 2001]. As the correction for helium is usually impossible, helium is often disregarded in the calculation of the NGT [Loosli et al., 2001]. However, since the temperature sensitivity of the solubility strongly increases with the noble gas mass (meaning helium is the least temperature sensitive), the loss of information is limited. The finding that most groundwaters contain an additional component of dissolved atmospheric gases in excess of the equilibrium concentration and the radiogenic component further complicates the calculation of the NGT. This additional component is called excess air and may have atmospheric composition or be fractionated with respect to air [Aeschbach-Hertig and Solomon, 2013]. Supersaturations of 10-50 % for Ne are frequently observed [Loosli et al., 2001]. In some cases deficits of dissolved gases are encountered, which can be caused by degassing of the groundwater into expanding bubbles of biogenic methane or N_2 from denitrification [Aeschbach-Hertig et al., 2008]. For the determination of the temperature dependent equilibrium component (and thus the NGT), models describing gas concentrations in groundwater are used. These characterize the processes leading to the observed gas excess or deficit. In inverse modeling [Aeschbach-Hertig et al., 1999], the parameters of the applied model are varied until the deviations of the modeled concentrations from the measured concentrations reach a minimum. By comparing these deviations with the uncertainties of the measured concentrations, the goodness of the achieved fit can be quantified [Aeschbach-Hertig and Solomon, 2013]. By Monte Carlo simulations, consisting of a variation of the measured concentrations within their respective measurement uncertainties followed by inverse fits of the data with the models, a higher accuracy can be achieved.

The models describing the noble gas concentrations with the equations characterizing them are discussed in detail in Aeschbach-Hertig and Solomon [2013]. Here only a short description of the most important models is given.

The simplest model is the **Unfractionated Air** (UA) model, assuming that, in addition to the equilibrium concentration, per amount of water a certain amount of gas is dissolved, whose composition is atmospheric. The physical process behind this model is a rise of the groundwater table, which causes bubbles of atmospheric air to become trapped in the water. The bubbles dissolve completely in the water due to the increased hydrostatic pressure. Beside the equilibration temperature, the additional amount of gas per amount of water is a model parameter.

The **Oxygen Depletion** (OD) model assumes that oxygen is depleted in the unsaturated zone and not replaced by the same amount of CO_2, which increases the partial pressures of the noble gases. Then, the water table rises, and gas bubbles of atmospheric composition are trapped and completely dissolved. Hence, the OD model corresponds to the UA model with the recharge altitude as free parameter to adjust the partial pressures to higher values. The adjustment of the recharge altitude is assumed to be the same for all samples in an area of investigation, to account for equal oxygen depletion in that area.

The **Partial Re-equilibration** (PR) model, as the UA model, assumes an increase of the water table, as well as trapping and complete dissolution of bubbles of atmospheric composition. However, in a re-equilibration process of the groundwater with the atmospheric air in the unsaturated zone, the excess dissolved gas concentration partly diffuses out. As the diffusion coefficients in water of the lighter noble gases are higher than the ones of the heavier (see Table 3.7), the excess is lost to a higher extend for the lighter noble gases. The additional amount of gas per amount of water and the grade of re-equilibration are model parameters.

In the **Closed Equilibration** (CE) model as in the UA model, bubbles of atmospheric composi-

tion become trapped by rising water. However, the hydrostatic pressure increase is not sufficient for a complete dissolution. The bubbles are compressed and only a part of that gas is dissolved. Between the compressed bubbles and the surrounding water a new gas solution equilibrium is established. The model parameters are the volume ratios of gas to water before and after the equilibration. Loss of dissolved gases can be described with expanding instead of shrinking bubbles [Aeschbach-Hertig et al., 2008]. As mentioned, contact of the water with bubbles of biogenic methane for example can cause the noble gases to partly outgas, when equilibrating with the bubbles.

Having the lowest solubility among the atmospheric noble gases, the relative influence of excess air on Ne is the highest. As discussed in the different models, excess air is caused by fluctuations of the water table. Hence, the relative Ne excess ΔNe is essentially a measure of the amplitude of water table fluctuations in the recharge area and hence the variability of precipitation [Aeschbach-Hertig et al., 2002].

Sun et al. [2010] investigated the influence of the employed model on the derived NGT by applying the different models on artificial sets of noble gas concentrations. Each sets was produced with a different model. For each set, the noble gas concentrations were varied within assumed "measurement uncertainties" using Monte Carlo simulations. They found that even if an incorrect model was used (for example, the PR model applied on a set produced using the CE model), a 20°C change in recharge temperature is still displayed correctly within about 1°C. Smaller changes in the recharge temperature are expected to be even more accurate. However, there are significant offsets between the models which can introduce apparent temperature variations. Estimating changes in the recharge temperature using NGT is only robust, if the same model is used for the analysis of the entire data set.

In principle, if all effects influencing noble gas concentrations during recharge are correctly accounted for [Aeschbach-Hertig and Solomon, 2013], NGTs provide a record of the absolute past long-term mean water table temperature (WTT) during groundwater recharge [Cey, 2009]. The difficulty is to convert this temperature to mean annual air temperature (MAAT) [Aeschbach-Hertig and Solomon, 2013]. The relation between WTT and MAAT may have changed over time due to changing climatic conditions, causing soil cover (vegetation, snow) also to change. Cey [2009] investigated the coupling of WTT and MAAT with numerical modeling experiments. He found only modest WTT changes (around 0.2°C) in response to moderate changes in precipitation amount ($\pm$20%) and water table depth (1-2 m). However, variation of the air temperature changed the duration of snow cover, which caused a significant change in the relation of WTT and MAAT. For example, for assumed 5-7°C cooler temperatures during the Last Glacial Maximum, the MAAT would be underestimated by around 1.4°C at sites of seasonal snow cover [Cey, 2009]. Fortunately, at snow free sites, the decoupling is insignificant with respect to the precision of NGTs [Cey, 2009].

The attainable precision of NGTs, which is mainly determined by the precision of noble gas measurements, affects the field of application. To resolve the glacial/interglacial temperature increase of 4.5-7°C observed in European aquifers [Corcho Alvarado et al., 2011], moderate precision is required. In contrast, the temperature variations of around 1-1.5°C in the Holocene (past 11000 years) are more difficult to resolve with the noble gas thermometer. Corcho Alvarado et al. [2009] for example, found the NGTs of an European aquifer to range from 9.6 to 10.9°C in the past 400 years, which were determined with $\pm$0.2°C precision.

2.4 Water Degassing with Membrane Contactors

This section provides a short overview on hollow fiber membrane contactors with a focus on the dependencies of the degassing efficiency. It is based on the work of Wiesler [1996], Stanojevic et al. [2003], Kartohardjono and Chen [2005], Melin and Rautenbach [2007], and Peng et al. [2008].

Membrane contactors are devices using membranes to provide a high interfacial area per volume between two components (liquid/liquid, liquid/gas, or gas/gas), with one component preferentially moistening the membrane. The mass transfer across the membrane is accomplished without dispersion of one phase within another. Unlike conventional membrane applications such as microfiltration or reverse osmosis, it is driven by a concentration rather than by a pressure gradient [Kartohardjono and Chen, 2005]. Compared to traditional contactors like mixer-settler cascades, packed columns or spraying towers, membrane contactors have, besides the lower investment costs, some important advantages. Per unit volume, they have a higher interfacial area (5000 - 30 000 $\mathrm{m^2/m^3}$ [Melin and Rautenbach, 2007]), which is well defined and constant (not changing with the flux). The flow rates of the two phases can be changed independently, allowing the ratio of the phases to be freely selected. Without any dispersion between the phases, emulsions, flooding and foaming are not occurring either and there is no need to separate the phases again after the contactor. Beyond that, membrane processes usually scale linearly [Kartohardjono and Chen, 2005] and a scale-up can easily be achieved by serial or parallel connection of additional membrane contactors. Among the disadvantages of membrane contactors, one can count the additional transfer resistance caused by the membrane itself, the loss of efficiency due to flow channeling, the shorter lifetime, clogging of the pores, and fouling. These disadvantages usually are manageable and overcompensated by the advantages [Melin and Rautenbach, 2007]. Different membrane configurations exist, like hollow fiber, flat sheet, rotating annular, and spiral wound, having applications in wastewater treatment, volatile organic compound (VOC) removal from waste gas, osmotic distillation, fermentation, pharmaceuticals, absorption of gaseous components into liquids (as carbonation of beverages), protein extraction [Stanojevic et al., 2003], or removal of dissolved components (oxygen, carbon dioxide, VOC, water) from liquids [Peng et al., 2008].

2.4.1 Hollow Fiber Membrane Contactors (HFMC)

For mass transfer between gas and liquid phase, membrane contactors usually utilize microporous hydrophobic hollow fiber membrances [Peng et al., 2008], as the pores are filled with gas and the contribution of the membrane to the total resistance of the mass transfer can hence be neglected [Stanojevic et al., 2003]. Forcing water to enter the pores would require a pressure equal to that given by the Young-Laplace equation modified for use with hydrophobic membranes [Wiesler, 1996; Melin and Rautenbach, 2007]:

$$P = -2\sigma\cos\theta/r \, , \tag{2.14}$$

where σ is the surface tension of water, θ the contact angle, and r the radius of the pores in the microporous membrane. For example, this breakthrough pressure exceeds 10 bar for a hydrophobic polypropylene membrane with a pore size of 0.05 $\mathrm{\mu m}$ [Wiesler, 1996]. The best known and

industrially most often employed membrane contactor is Liqui-Cel from Membrana (Figure 2.3) [Melin and Rautenbach, 2007], which also was chosen for the degassing setup developed in this work. As for the majority of hollow fiber membrane contactors (HFMC), the liquid flows on the *shellside* (outside the hollow fibers) in order to avoid huge pressure drops caused by the 200 µm inner diameter of the fibers. It enters and leaves the contactor via the central distribution and collection tube, respectively. The tubes are separated by a baffle to inhibit flow channeling. The hollow fibers, hosting the gas phase on the inside (on the *lumenside*), are knitted into some kind of mat which is wound around both tubes. When the two phases are flowing in opposite directions to each other (countercurrent mode), the gas transfer between the phases is higher than in cocurrent mode (the two phases flowing in the same direction). Liqui-Cel achieves even a higher local mass transfer than the one obtained with just countercurrent [Stanojevic et al., 2003] by having the phases flow in opposite directions and additionally having the water flow perpendicular to the fibers (cross-countercurrent). The two gas ports are connected with the lumenside of the hollow fibers, one of them acting as inlet and the other as outlet in gas absorption processes. Vacuum, a sweep gas, or any combination of those are in contact with the gas ports for gas stripping.
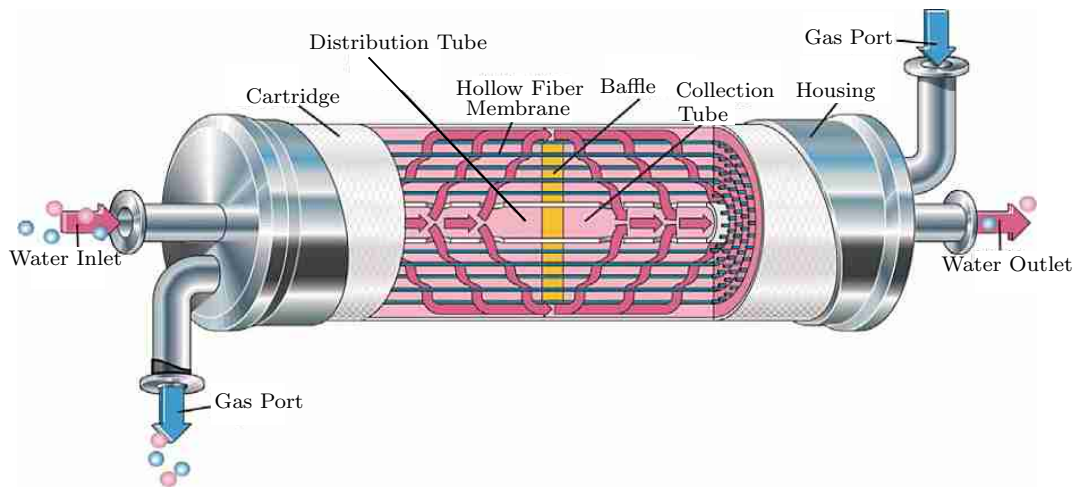
Figure 2.3: A sketch of the Liqui-Cel Extra-Flow contactor used in this work is shown here (after Membrana [2012]). For the purpose of gas stripping, the gas ports can be connected to any combination of vacuum and sweep gas.

2.4.2 Mass Transfer in HFMC and Degassing Efficiency

As already mentioned, the driving force for mass transfer across the membrane in HFMC is the concentration gradient. According to the Henry´s law (see Section 2.3.1 for more details), in equilibrium, the concentration C_l of gas dissolved in a liquid is proportional to its concentration C_g in the atmosphere above the liquid:

$$C_l = L \cdot C_g, \tag{2.15}$$

with the dimensionless Ostwald-solubility L. When decreasing C_g by applying vacuum or a sweep gas on the lumenside, the gas dissolved in the liquid will partly outgas (cross the membrane) in

order to establish a new equilibrium with the lower partial pressure on the gas phase. For a gas stripping setup, the degassing efficiency η is a measure of performance:

$$\eta = 1 - \frac{C_{l,\omega}}{C_{l,\alpha}}, \tag{2.16}$$

with $C_{l,\alpha}$ and $C_{l,\omega}$ standing for the concentrations of dissolved gas in the liquid at the entrance and the exit of the membrane contactor, respectively. For a strongly diluted substance system in steady state and running in cross-countercurrent mode through a membrane contactor, Melin and Rautenbach [2007] derived the following equation for the dimensioning the axial length l of the membrane by setting up a mass balance:

$$l = \frac{\overline{u}}{k \cdot a} \cdot \frac{1}{1 - L \cdot \frac{\dot{V_l}}{\dot{V_g}}} \cdot \ln\left(\frac{C_{l,\alpha} - LC_{g,\omega}}{C_{l,\omega} - LC_{g,\alpha}}\right), \tag{2.17}$$

with the volume flow rates $\dot{V_l}$ and $\dot{V_g}$ of the liquid and the gas phase, respectively, the velocity $\overline{u}$ of the fluid inside the contactor, and the specific surface a of the contactor (the ratio of the total membrane surface to the shellside volume). Although the setup developed in this work employs the vacuum mode, this is still a good approximation for checking the dependencies of degassing, as the first half of the contactor can be considered running in cross-countercurrent mode and the other half in cross-parallelflow. The overall mass transfer coefficient k describes how quickly a mass can move through a medium and is the inverse of the total transport resistance from liquid to gas phase, which is the sum of the individual resistances:

$$\frac{1}{k} = \frac{1}{k_l} + \frac{1}{k_m} + \frac{1}{k_g}, \tag{2.18}$$

with the mass transfer coefficients of liquid phase k_l, membrane k_m, and gas phase k_g. The resistance of the membrane and the gas phase are much smaller than $\frac{1}{k_l}$ and can be neglected, hence $k \approx k_l$ [Wiesler, 1996; Kartohardjono and Chen, 2005; Melin and Rautenbach, 2007]. For a HFMC running in cross-counterflow mode with water on the shellside, the expression for k_l reads:

$$k \approx k_l = 1.4 \cdot \frac{D}{d} \cdot \left(\frac{d \cdot \overline{u}}{D}\right)^{1/3}, \tag{2.19}$$

with the outer diameter d of the hollow fiber and the diffusion coefficient D of the gas in water [Wiesler, 1996; Melin and Rautenbach, 2007]. Equation 2.17 now can be rearranged in order to obtain an expression for the degassing efficiency:

$$\eta = 1 - \frac{C_{l,\omega}}{C_{l,\alpha}} = 1 - \frac{LC_{g,\alpha}}{C_{l,\alpha}} - \left(1 - \frac{LC_{g,\omega}}{C_{g,\alpha}}\right) \cdot \exp(-x), \tag{2.20}$$

with the argument x of the exponential function:

$$x = l \cdot k_l \cdot a \cdot (1 - L \cdot \frac{\dot{V_l}}{\dot{V_g}}) \cdot \frac{1}{\overline{u}} = 1.4 \cdot l \cdot a \cdot (1 - L \cdot \frac{\dot{V_l}}{\dot{V_g}}) \cdot \left(\frac{D \cdot A_l}{d \cdot \dot{V_l}}\right)^{2/3}. \tag{2.21}$$

The expression for k_l from Equation 2.19 was plugged in and the following relation was used:

$$\overline{u} = \frac{\dot{V}_l}{A_l} \, ,$$

(2.22)

with the cross sectional area A_l which is available for the water flow in the membrane contactor. For a given HFMC and sampling water, C_l, d, l, a and A_l are fixed. For the purpose of maximizing the degassing efficiency, this leaves the following tuneable parameters: the Ostwald-solubility L, the diffusion constant D of the gas in water, the concentrations $C_{g,\alpha}$ and $C_{g,\omega}$ of the gas at the entrance and the exit of the lumenside, and the volumetric flow rates $\dot{V}_g$ and $\dot{V}_l$ of the gas and the liquid phase, respectively. L and D both depend on temperature. While L decreases with rising temperature, D increases with T [Cussler, 2005; Gerthsen et al., 1977]:

$$D = \frac{k_B \cdot T}{6\pi\mu R_0} = \frac{k_B \cdot T}{6\pi\mu_0 \exp(b/T) R_0} \, ,$$

(2.23)

with the Boltzmann constant k_B, the radius R_0 of the dissolved gas particles, the dynamic viscosity μ of the liquid, and the constants μ_0 and b. μ decreases exponentially with rising T, causing D to rise even faster with increasing temperature. These temperature dependences of L and D lead to an increase in the degassing efficiency η with increasing temperatures. However, due to its high specific heat capacity, it would require too much energy to warm the water prior to degassing. η is strongly rising with decreasing $C_{g,\alpha}$ and slightly rising with increasing $C_{g,\omega}$. In vacuum mode, only the first half of the chosen HFMC can be considered running in counterflow mode (for which the equations are derived). $C_{g,\omega}$ is therefore not located at the exit but rather in the middle of the contactor, and $C_{g,\alpha}$ at both gas exits. Hence $C_{g,\omega}$ can not be increased without also increasing $C_{g,\alpha}$, since both depend on the pressure at the gas ports. Beyond that, the degassing efficiency strictly derived for vacuum mode is very likely to decrease with increasing $C_{g,\omega}$. η also decreases with increasing water flow rate $\dot{V}_l$. As the amount of gas extracted from water per time is the product of η and $\dot{V}_l$, the water flow rate should only be limited where η drops sharply with $\dot{V}_l$. Furthermore, the degassing efficiency rises with increasing gas flow rate. Together with the strong dependence of η on $C_{g,\alpha}$, this means that a low pressure at the gas ports and therefore a high performance of the vacuum pumps are essential for a good degassing efficiency.

2.5   Adsorption of Gases on Surfaces

This sections aims at giving an introduction to the adsorption of gases on surfaces without going too much into the details and focusing on the knowledge needed to understand this work. Among other sources, it is essentially based on the work of Yang [2003], Keller and Staudt [2005], and Ruthven [2006].
Section 2.5.1 introduces some basic terms, while Section 2.5.2 summarizes the effects on which gas separation can be based on. To understand which quantities affect the gas separation and how, the simplest adsorption isotherm able to describe the adsorbent material used is discussed in Section 2.5.3. Section 2.5.4 gives an overview of the composition of the physical forces acting on the adsorbed molecules. Activated carbon is introduced shortly in Section 2.5.6, whereas Section 2.5.5 addresses zeolites in detail.

2.5.1   Introduction

The adhesion of molecules of gas, liquid, or dissolved solids to a surface is called *adsorption* and occurs in principle at any pressure and temperature. This results in a film of *adsorbate* on the surface of the *adsorbent.* The gas or liquid whose molecules are interacting with the surface of the adsorbent is called *adsorptive.* Adsorption normally is exothermic, whereas the reverse process (*desorption*) is endothermic. Adsorption is not to be confused with *absorption*, where molecules of gases or liquids are dissolved in another liquid or solid material. Depending on the nature of the surface forces leading to adsorption, one distinguishes between physisorption and chemisorption. In the case of physisorption, the adsorbed molecules are weakly bound by van der Waals and electrostatic forces (see Section 2.5.4 for more details) and can be desorbed reversibly by lowering the adsorptive gas pressure or increasing the temperature without changing structure or composition of the adsorbent. This allows using the adsorbent nearly unlimited times in cycles of employment and regeneration. In contrast, the adsorption in chemisorption systems is irreversible and much stronger, involving a substantial degree of electron transfer or electron sharing, similar to the formation of chemical bonds. Having in mind the huge amounts of air the device for argon separation will have to process, a adsorbent was chosen, which can be regenerated. For that reason only physisorption will be discussed in the following. Beside gas separation, typical applications of adsorbents are cleaning, drying or gas storage processes.

2.5.2   Gas Separation Processes

The separation of a gas from a mixture can be achieved by exploiting one or more of the following physical effects Keller and Staudt [2005]:

1. Mixture adsorption equilibria (the gas is much more (or much less) adsorbed than all the others).

2. Adsorption kinetic effects (the gas diffuses much faster (or much slower) within the adsorption material than all the others).

3. Molecular sieve effects (either the gas or all the others are too voluminous too reach the adsorption sites).

4. Boiling point (the gas has a much higher (or much lower) boiling point than all the others).

Having kinetic diameters lying close together (N_2: 3.64 Å, O_2: 3.43 Å, Ar: 3.83 Å [Peter et al., 2011]), these gases can not be separated by molecular sieve effects. The commercial gas separation processes pressure swing adsorption and vacuum swing adsorption rely on the first two effects listed above, but have either a low yield or low purity (compared to the process developed in this work). Cryogenic distillation, the separation process most often deployed in large-volume pure gas production, takes advantage of the differences in the boiling points of the gases in the mixture. The required equipement, though, is quite costly and purity comes again at the cost of yield. The process chosen in this work is based on mixture adsorption equilibria. This chapter will be restricted to the theory needed to understand the latter.

2.5.3   Adsorption Isotherms

The predominant scientific basis for adsorbent selection is the equilibrium isotherm [Yang, 2003]. The amount of adsorbed gas per gram of adsorbent at equilibrium is a function of temperature and pressure. For constant temperature, this relation is called the adsorption isotherm. Together with other representations of gas adsorption equilibria data, an isotherm is schematically shown on the left hand side in Figure 2.4. Due to the complexity of interactions of the adsorbed molecules with the atoms and molecules of the adsorbent material, it is still not possible to calculate adsorption isotherms either "ab initio" by statistical molecular methods or by phenomenological methods based on a few macroscopic or microscopic data of the adsorptive-adsorbent system Keller and Staudt [2005]. However, one can measure gas adsorption equilibria data, choose the analytical isotherm best fitting it, and then extrapolate the isotherm to other pressures and temperatures. According to the recommendations of the International Union of Pure and Applied Chemistry (IUPAC, Sing et al. [1985]), the majority of physisorption isotherms may be classified into the 6 types shown in Figure 2.5. Type I isotherms describe the gas adsorption equilibria of adsorbent materials with narrow pore spectra as the zeolite used in this work. They can be represented by the Langmuir isotherm Langmuir [1916], which will be derived hereafter following Do [1998] for process design. In view of space limitations we do not consider them here but refer to the literature [7.2, 7.5, 7.10, 7.11].
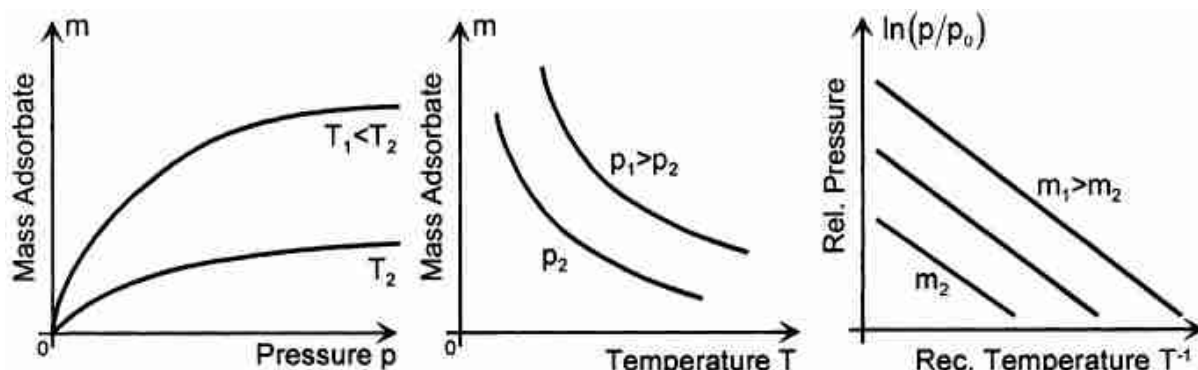
Figure 2.4: Gas adsorption equilibria data represented as isotherms (T = const), isobars (p = const), and isosteres (loading = const), taken from Keller and Staudt [2005].

Langmuir Approach

The Langmuir approach for pure component adsorption is a kinetic theory where, in equilibrium, the rate of desorbing molecules is equal to the rate of the adsorbing ones. It is based on the following assumptions:

1. The number of adsorption sites is fixed and they are localized.

2. Each site can only accommodate one molecule (monolayer adsorption).

3. The adsorption energy is constant over all sites (homogeneous surface).

4. Interactions between the adsorbate molecules are small compared to adsorbate - adsorbent interactions and can be neglected.
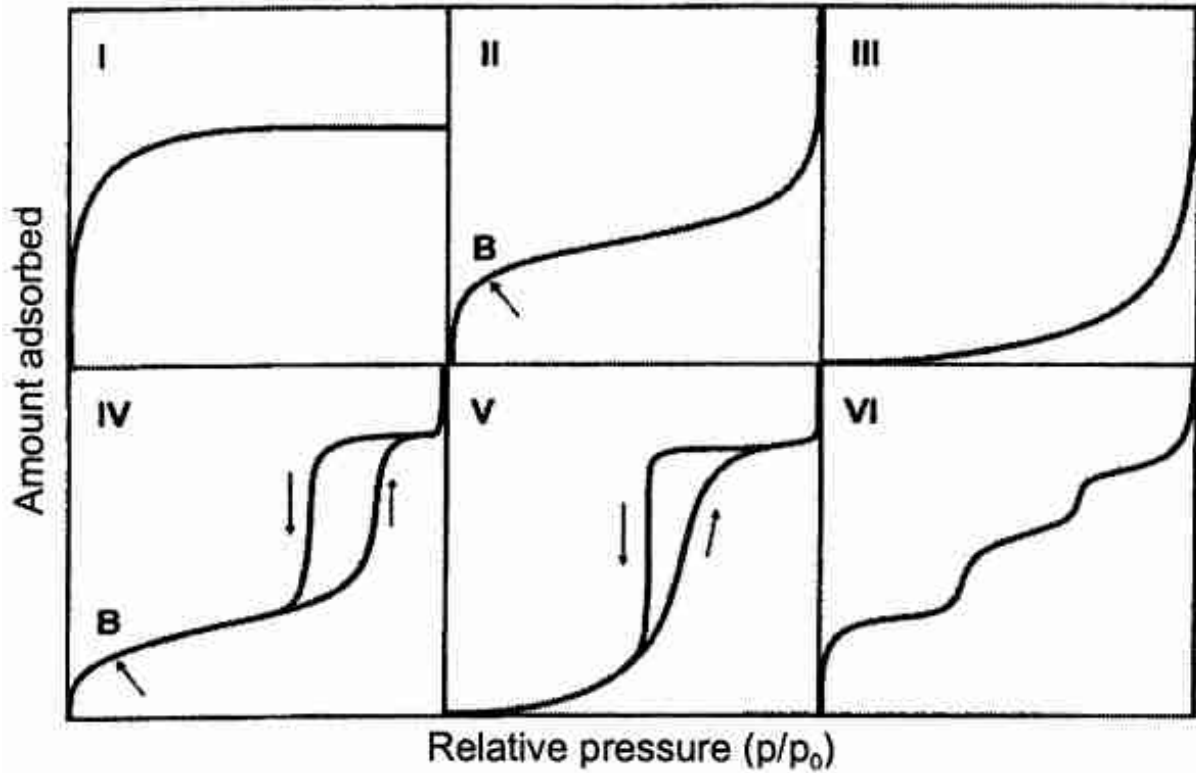
Figure 2.5: Gas physisorption isotherms can be classified into the main types shown here (figure taken from Keller and Staudt [2005]).

According to the kinetic theory of gas, the rate of impinging molecules on a surface in mole per unit time and unit area is:

$$R_i = \frac{p}{\sqrt{2\pi MRT}}, \tag{2.24}$$

with the pressure p, the molar mass of the adsorptive M, the ideal gas constant R, and the temperature T (in Kelvin). Considering not all molecules striking the surface will be adsorbed and already occupied sites are not available for adsorption, the rate of adsorption R_a is obtained by including the sticking probability s and the fraction of occupied sites θ in the equation above:

$$R_a = (1-\theta)sR_i = (1-\theta)\frac{sp}{\sqrt{2\pi MRT}} = (1-\theta)k_a p. \tag{2.25}$$

k_a is called the rate constant of adsorption. The rate of desorption from the surface is attained by multiplying the rate of desorption k_d from a completely covered surface by the fractional coverage:

$$R_d = \theta k_d = \theta k_{d\infty} \exp\frac{\Delta H}{RT}, \tag{2.26}$$

where ΔH is the isosteric heat of adsorption (the enthalpy change for physical adsorption), which is negative [Yang, 2003]. $k_{d\infty}$ is the rate constant for desorption at infinite temperature

and is the inverse of average residence time of adsorption at that temperature, $\tau_{d\infty}$. The average residence time of adsorption can now be defined as:

$$\tau_d = \tau_{d\infty} \exp \frac{-\Delta H}{RT} . \tag{2.27}$$

For physical adsorption, this residence time typically ranges between 10^{-13} to 10^{-9} seconds. As will be later demonstrated, the Arrhenius dependence on temperature of τ_d can be exploited to separate even species only slightly differing in ΔH. Eventually, by equating the rates of adsorption and desorption (at equilibrium both rates are the same), one arrives at the Langmuir equation in terms of fractional loading:

$$\theta = \frac{bp}{1 + bp} . \tag{2.28}$$

The affinity (or Langmuir) constant b, which is defined as the ratio of the rate constants of adsorption and desorption, is a measure for the adsorption strength:

$$b = \frac{k_a}{k_d} = \frac{s \exp \frac{-\Delta H}{RT}}{k_{d\infty}\sqrt{2\pi MRT}} . \tag{2.29}$$

The higher b is (i.e. the more negative ΔH), the more of the adsorptive is adsorbed at the same pressure and the stronger the attraction between the adsorbate molecule and the surface. For data correlation, it is beneficial to have the Langmuir equation written in the form of amount adsorbed in mole per unit mass:

$$n = n_{max}\frac{bp}{1 + bp} , \tag{2.30}$$

where n_{max} is the maximum amount adsorbed per unit mass corresponding to a complete monolayer coverage.

Henry´s Law

At low pressures, as should all isotherms, the Langmuir isotherm reduces to a linear form [Yang, 2003]. Similar to the Henry´s Law describing the solubility of a gas in a liquid, where the concentration of the gas dissolved in the liquid is equal to the Henry constant times the pressure above the liquid, here the amount adsorbed is equal to the Henry constant K times the pressure of the adsorptive:

$$n = Kp = n_{max}bp . \tag{2.31}$$

The amount adsorbed then increases linearly with pressure.

Langmuirian Multicomponent Theory

As argon is separated from air in this work, the Langmuir equation has to be extended for mixtures. Together with the presumption that there are no interactions between the different

gas species, the same assumptions are made as for the Langmuir approach for the pure component adsorption. In a multicomponent gaseous system containing N species, again, the rate of adsorption of the species i, $R_{a,i}$, is proportional to its rate constant of adsorption $k_{a,i}$, its partial pressure p_i, and the total fraction of empty adsorption sites:

$$R_{a,i} = (1 - \sum_{j=1}^{N} \theta_j) k_{a,i} p_i = (1 - \sum_{j=1}^{N} \theta_j) \frac{s_i p_i}{\sqrt{2\pi M_i RT}} , \qquad (2.32)$$

with the molar mass M_i and the sticking probability s_i of component i, and the fraction of the sites occupied by species j. The rate of desorption of the species i, $R_{d,i}$, is proportional to its rate constant of desorption $k_{d,i}$ and its fraction of occupied sites:

$$R_{d,i} = \theta_i k_{d,i} = \theta_i k_{d\infty,i} \exp \frac{\Delta H_i}{RT} , \qquad (2.33)$$

with the isosteric heat of adsorption ΔH_i and the rate constant of desorption at infinite temperature $k_{d\infty,i}$ of species i. By equating the rates of adsorption and desorption of species i and summing over all species, Do [1998] arrives at the extended Langmuir equation in terms of fractional loading of species i:

$$\theta_i = \frac{b_i p_i}{1 + \sum_{j=1}^{N} b_j p_j} , \qquad (2.34)$$

where b_i is again the ratio of the rate constant of adsorption to that of desorption:

$$b_i = \frac{k_{a,i}}{k_{d,i}} = \frac{s_i \exp \frac{-\Delta H_i}{RT}}{k_{d\infty,i} \sqrt{2\pi M_i RT}} . \qquad (2.35)$$

The extended Langmuir equation, too, is preferentially expressed in the form of amount adsorbed in mole per unit mass:

$$n_i = n_{max} \frac{b_i p_i}{1 + \sum_{j=1}^{N} b_j p_j} , \qquad (2.36)$$

with the monolayer saturation capacity n_{max}, which has to be the same for all species Do [1998].

Langmuir-Freundlich (Sips-) Equation for Multicomponent Adsorption

The Langmuir-Freundlich- or Sips-equation is the result of an empirical approach based on the Langmuir equation avoiding indefinite increase in adsorption with pressure [Sips, 1948],[Yang, 2003]:

$$n_i = n_{max} \frac{b_i p_i^{1/z_i}}{1 + \sum_{j=1}^{N} b_j p_j^{1/z_j}} , \qquad (2.37)$$

with the parameters z_i describing effects of heterogeneity. This equation has been very useful for practical design and process simulation [Yang, 2003] and it proved to give excellent predictions for adsorption equilibria data for a mixture of nitrogen, oxygen and argon on molecular sieve 5A [Miller et al., 1987]. With the aid of the Sips-isotherm, the criteria for the adsorbent selection for the separation of Argon from air will be developed in the following.

Separation Factor (Selectivity)

The separation factor or selectivity S_{ik} is a measure of how suitable an adsorbent is for the separation of the species i and k. It is the ratio of the amounts adsorbed with respect to the partial pressures:

$$S_{ik} = \frac{n_i/p_i}{n_k/p_k} = \frac{n_i p_k}{n_k p_i} \, . \tag{2.38}$$

For the Sips-equation it reads:

$$S_{ik} = \frac{b_i p_k^{1-1/z_k}}{b_k p_i^{1-1/z_i}} = \frac{s_i k_{d\infty,k} \sqrt{M_k}}{s_k k_{d\infty,i} \sqrt{M_i}} \frac{p_k^{1-1/z_k}}{p_i^{1-1/z_i}} \exp \frac{\Delta H_k - \Delta H_i}{RT} \, . \tag{2.39}$$

Let species i be the one preferentially adsorbed (i.e. with the more negative ΔH. Then S_{ik} is increasing with decreasing temperature (since $\Delta H_k - \Delta H_i > 0$). The higher the difference between the isosteric heats of adsorption is, the more distinct is this temperature sensitivity of the separation factor. An adsorbent only weakly interacting with argon (having a less negative ΔH_{Ar}) and strongly binding nitrogen and oxygen (possessing more negative ΔH_{N_2} and ΔH_{O_2}) would result in high $S_{N_2,Ar}$ and $S_{O_2,Ar}$ for example.

Isosteric Heat of Adsorption

The isosteric heat of adsorption ΔH is defined as the heat ∂Q released upon adsorption of an infinitesimal amount ∂m_a of gas molecules at constant pressure p, temperature T, and mass of adsorbent M_s [Chakraborty et al., 2006]:

$$\Delta H = - \left(\frac{\partial Q}{\partial m_a} \right)_{pTM_s} \, . \tag{2.40}$$

The conventional way to determine the isosteric heat of adsorption is applying the Clausius-Clapeyron equation as approximation, which describes the temperature dependence of the equilibrium vapor pressure [Ruthven, 2006]:

$$\left(\frac{\partial \ln p}{\partial T} \right)_\theta = \frac{\Delta H}{RT^2} \, . \tag{2.41}$$

Assuming that the heat of adsorption is independent of temperature, integration of the equation above yields:

$$\ln p = -\frac{\Delta H}{RT} + constant \, . \tag{2.42}$$

Plotting now the isostere as $\ln p$ vs $1/T$, ΔH can easily be calculated from the slope. A more rigorous way to derive an expression for ΔH can be found in Chakraborty et al. [2006]. For Langmuirian systems a homogenous surface, monolayer adsorption and negligible interactions between adsorbate molecules are assumed. Therefore the isosteric heat of adsorption should be independant of loading, which is not true for most real systems. Some adsorbents show less negative ΔH with increasing loading as sites with higher attraction forces are occupied first. For others the isosteric heat becomes more negative with increasing loading since the adsorbate-adsorbate interactions are stronger than the adsorbate - adsorbent interactions. In some cases both effects compensate, resulting in an essentially constant heat of adsorption.

2.5.4   Physical Adsorption Forces

According to Yang [2003], at low coverages, the isosteric heat of adsorption ΔH is related to the adsorbate - adsorbent interaction potential ϕ by:

$$\Delta H = \phi - RT + F(T) \, , \tag{2.43}$$

with $F(T)$ accounting for the vibrational and translational energies of the adsorbate molecule. For ambient temperatures and all the more for lower temperatures, $\Delta H \approx \phi$. When choosing an adsorbent for a separation process, it is useful to look at the fundamental properties of the target molecule (polarizability, magnetic susceptibility, permanent dipole moment, and quadrupole moment) compared with the other species in the mixture. Depending on those properties, the single contributions to ϕ can be more or less important:

$$\phi = \phi_D + \phi_R + \phi_{Ind} + \phi_{F\mu} + \phi_{\dot{F}Q} \, . \tag{2.44}$$

The dispersion energy ϕ_D and the close-range repulsion energy ϕ_R form the Lennard-Jones potential, which is nonspecific and present in all adsorbate-adsorbent systems. With charges on the surface of the adsorbent, there are also the interactions ϕ_{Ind} between an induced dipole and the electric field, the interactions $\phi_{F\mu}$ between a permanent dipole and the electric field, and the interactions $\phi_{\dot{F}Q}$ between a quadrupole and the electric field gradient (given that the adsorbate molecule has a permanent dipole and/or quadrupole). The most important property determining ϕ_D, ϕ_R, and ϕ_{Ind} is the polarizability α, which unfortunately is nearly the same for N_2, O_2, and Ar (1.74, 1.58, and 1.63 in units of $10^{-24}cm^3$, respectively, [Yang, 2003]). Since all are nonpolar, there is no contribution from $\phi_{F\mu}$ for those gases. However, they differ in the quadrupole moment Q. Q_{N_2} is around four times Q_{O_2}, and Q_{Ar} is zero. Keeping in mind that the separation performance rises with increasing differences in the isosteric heats of adsorption ΔH, and $\Delta H \approx \phi$, one should aim to maximize those differences for the gases in the mixture. $\phi_{\dot{F}Q}$ is directly proportional to Q and to the electric field gradient $\dot{F}$. In order to separate argon from nitrogen and oxygen for ^{39}Ar-dating, an adsorbent with a high electric field gradient therefore should be selected. Zeolites, having the cations dispersed above the negatively charged oxides on their surfaces, are the only such adsorbents [Yang, 2003].

2.5.5   Zeolites

This section, summarizing the most important information about zeolites (in regard to this work), is based on Yang [2003].

Zeolites are crystalline aluminosilicates of alkali and earth alkali elements occurring in nature or produced synthetically. SiO_4 and AlO_4 tetrahedra, their primary structural units, are joined by a shared oxygen and build secondary polyhedral units such as cubes, hexagonal prisms or octahedra. In turn, the secondary units are assembled in a regular three-dimensional crystalline framework containing pores which can be accessed by molecular sized windows. In addition, there are exchangeable extra framework cations, balancing the -1 electric net charge of the aluminium atoms in AlO_2. That is why the number of extra framework cations rises with increasing exchange of Si with Al. The adsorption properties and the aperture sizes of the zeolite depend on the number and kind of these cations. Hence the adsorption properties can be custom-tailored by adapting the chemical composition, which reads in the hydrated form:

$$M_{x/n}^{+n}[(AlO_2)_x^{-1}(SiO_2)_y] \cdot zH_2O \,, \qquad (2.45)$$
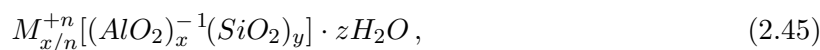
where x and y are integers with y/x equal to or greater than 1, n is the valence of cation M, and z is the number of water molecules in each unit cell [Yang, 2003]. The water can easily be removed by heating and evacuating, leaving the aluminosilcate frame nearly unchanged. The unit cells of types A, X and Y, the dominant zeolites in commercial use for adsorption and ion exchanges, are shown in Figure 2.6 in line representation. The Al and Si atoms are located wherever lines are joining, and lines represent shared oxygen molecules. The truncated octahedron or sodalite cage, the structural unit of these zeolites, is illustrated in Figure 2.6a. Figure 2.6b shows the unit cell of type A zeolite, and Figure 2.6c the unit cell of type X and Y. Figure 2.6d depicts the locations of the exchangeable extra framework cations for type A, and Figure 2.6e the locations of the cations for type X and Y. Since a zeolite of type X proved to serve well for the setup for argon separation, the following discussion will be focused on that type.

Zeolite Type X

The structure of the aluminosilicate framework of type X zeolite is identical to that of natural occurring faujasite. 192 (Al,Si)O_4 tetrahedra belong to each unit cell, and the Si/Al ratio ranges from 1 to 1.5 (1 is the minimum as Al-O-Al bridges are forbidden after Loewenstein´s rule). The sodalite cages are joined by 6-member prisms. Among any known zeolite, type faujasite has the largest central cavity volume, accounting for about 50% of the void fraction in dehydrated form. The free diameters of the aperture formed by the 12-oxygen ring and of the central cavity are 7.4 Å and 13.7 Å, respectively. The major locations for the exchangeable extra framework cations are shown in Figure 2.6e. Location I is situated at the center of the 6-member prism and I´ is located inside the sodalite cage opposite to I. The sites II and II´ are further away from the central cavity, in other ways resembling I and I´. III and III´ are located at the 12-oxygen aperture. With 16 I, 32 I´, 32 II, 32 II´, 48 III, and 32 III´ sites per unit cell, there are more sites than cations occupying them. I, I´and II´ are not exposed and can not interact with adsorbate molecules. Water, possibly being small enough to pass through the 6-oxygen ring (which has a diameter of 2.8 Å), may be an exception. Sites II and III are exposed to the cavity and are occupied by alkali metal cations (Li, Na, Ka, Rs, Cs). However, alkaline earth metal cations (Be, Mg, Ca, Sr, Ba) lean towards filling out site II only.
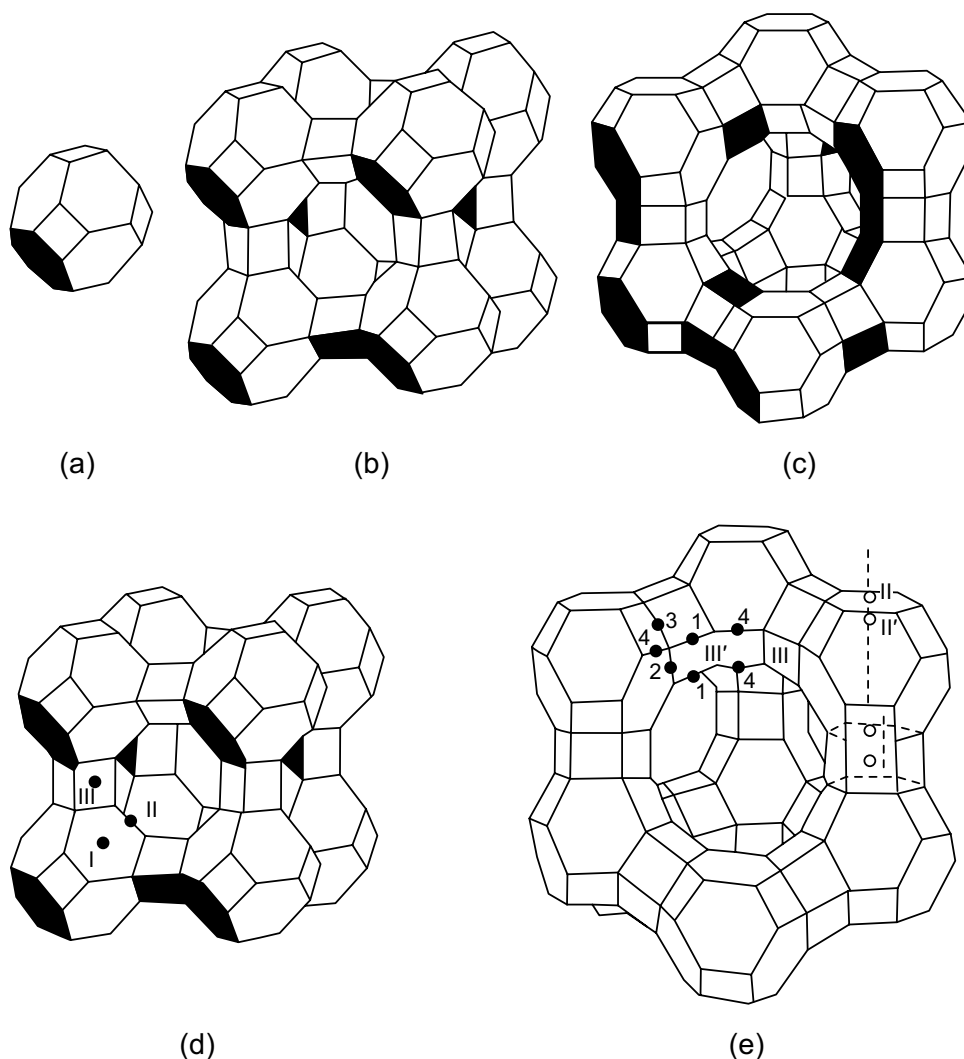
Figure 2.6: Zeolites in line representation. Al and Si are located at line junctions, while lines represent shared oxygens. (a) sodalite cage; (b) unit cell of type A; (c) unit cell of types X and Y; (d) cation sites in type A; (e) cation sites in types X and Y; taken from Yang [2003].

Molecular Sieving

Molecular sieving, i.e. size exclusion of adsorptive molecules, is a zeolite property resulting from the uniform molecular sized apertures of the aluminosilicate framework. For example, zeolite 3A excludes all hydrocarbons, N_2, O_2, and essentially all permanent gases except ammonia [Yang, 2003]. This makes it an excellent choice for drying gases under reactive conditions. Molecular sieving depends on temperature, as aperture size decreases with falling temperature. However, as has already been discussed in Section 2.5.2, the kinetic diameters of N_2, O_2, and Ar lie too close together to exploit this effect.

Interactions with Cations

Al and Si are barely exposed and the surface of the framework virtually consists of the more

abundant and much more polarizable oxygen atoms, which are hence dominating the Van der Waals interactions with the adsorbate molecules. For adsorbate molecules with a permanent dipole or quadrupole moment, the contribution to the total interaction potential from the interactions with the cations located above the oxide surface can be dominant, though. Sites are occupied by cations in such a manner that the free energy of the system is minimized. It should be remembered that there are more possible sites than cations occupying them (for zeolite X, 192 sites face a maximum of 96 cations). Unfortunately, the sites with the lowest energy (I, I´, and II´) are not exposed to the central cavity, but preferentially occupied. For example, the N_2/O_2 selectivity of low silica zeolite X (LSX, Si/Al = 1) can be significantly improved by exchange of Na^+ with Si^+. However, no improvement is observed until 70 % of the Na^+ cations have been exchanged. After that, a linear increase in N_2 adsorption with cation exchange is seen and exposed sites start getting occupied. How different ionic radii and charges of cations affect the electrostatic interactions becomes clear when looking at the following dependencies:

Field-Induced Dipole:

$$\phi_{Ind} \propto \frac{q^2 \alpha}{r^4} , \qquad (2.46)$$

Field-Dipole:

$$\phi_{F\mu} \propto \frac{q\mu}{r^2} , \qquad (2.47)$$

Field Gradient - Quadrupole:

$$\phi_{\dot{F}Q} \propto \frac{qQ}{r^3} , \qquad (2.48)$$

with $r = r_i$ (ionic radius) $+ r_j$ (adsorbate molecule), the electronic charge of the ion q, the polarizability α, the electric field F, the permanent dipole moment μ, and the permanent quadrupole moment Q. Yang [2003] compiled a summary for some isolated ions and their interactions with N_2, O_2 and Ar (see Table 2.3). For argon, the van der Waals forces (ϕ_D and ϕ_R) are much smaller than the interactions ϕ_{Ind} between the electric field and the induced dipole. ϕ_{Ind} increases with the charge q and decreases strongly with the ionic radius ($\phi_{Ind} \propto r^{-4}$). As divalent ions only have a slightly bigger radius but twice the charge, ϕ_{Ind} is much larger for them as for monovalent ions ($\phi_{Ind} \propto q^2$). For N_2 and O_2, the total interaction potential ϕ_{total} is much higher for the smaller ion (Li^+) than for the bigger ion (Na^+). For the same ion, ϕ_{total} is higher for N_2. This is mainly due to its 4 times higher quadrupole moment, as the sizes, polarizabilites, and magnetic susceptibilities of N_2 and O_2 do not differ much.
Summing up, in order to separate argon from air, the exchanged cation should be as small as possible and monovalent, i.e. Li^+. Then ϕ_{Ind} is not too high for Ar and $\phi_{\dot{F}Q}$ is at a maximum for N_2 and O_2.

2.5.6   Activated Carbon

As has been motivated in the last sections, zeolites are the only adsorbents appropriate to separate argon from air. Another adsorbent employed in this work is activated carbon. Only these

Molecule or Ion	r [$\mathring{A}$]	$10^{24}\alpha$ [cm^3]	$10^{30}\chi$ [cm^3/molc]	Q [esu]	$-(\phi_D + \phi_R)$ [kJ/mol]	ϕ_{Ind} [kJ/mol]	ϕ_{tot} [kJ/mol]
Ar	1.92	1.63	0				
O(O$_2$)	1.73	1.58	-1.3				
N(N$_2$)	1.89	1.74	-4.7				
Ar-Ion:							
Li+	0.78	0.029	-0.99	0	0.21	21.3	21.5
Na+	0.98	0.180	-6.95	0	0.67	16.0	16.6
K+	1.33	0.840	-27.54	0	1.80	10.2	12.0
Ca^{2+}	0.99	0.471	-22.1	0	2.13	63.5	65.6
Sr^{2+}	1.13	0.863	-46.17	0	3.26	52.7	55.9
Ba^{2+}	1.35	1.560	-76.4	0	4.22	40.7	44.9
O$_2$-Li+							32
O$_2$-Na+							20
N$_2$-Li+							51
N$_2$-Na+							36

Table 2.3: The interaction energies ϕ between molecules and isolated ions (taken from Yang [2003]). α is the polarizability, χ the magnetic susceptibility, and Q the quadrupole moment.

two materials are treated in this work. For more details and a broader overview of currently used adsorbents, the reader may consult Yang [2003].

Activated carbon possesses the largest surface area among all adsorbents. Its surface is non-polar and virtually only interacting via the nonspecific, weak van der Waals forces. Adsorbed molecules therefore desorb already to a great extend at room temperature and almost completely at moderately high temperatures (100°C), making it an excellent adsorbent for transferring samples from one device to another. Carbonaceous matters such as wood, peat, coals, petroleum coke, bones, coconut shell, and fruit nuts serve as raw materials. Gas activation, one of the two standard activation processes, comprises initial treatment of the raw materials, pelletizing, carbonization and partial gasification. The bulk of the volatile matter is removed at 400 - 500 °C during carbonization. Then porosity and surface area evolve at 800-1000 °C under the influence of a weakly oxidizing gas in the course of partial gasification. Activated carbon manufactured by this process is deployed mainly for gas and vapor adsorption processes.

2.6 Adsorption Chromatography

The separation of argon from the air degassed from groundwater is realized in this work by gas chromatographic adsorption on solid adsorbents (zeolite Li-LSX, activated charcoal). Chromatography is a physical separation method where the *analyte* (the components which have to be separated) is distributed between a mobile and a stationary phase. The method is called adsorption chromatography when the stationary phase is represented by a film of adsorbate on a solid adsorbent and gas chromatography when the mobile phase is a gas. The tubing contain-

ing the adsorbate is called *column* and the adsorbate filling of the column is called *bed*. The gas carrying along the analyte through the column without or only weakly interacting with the bed is the *carrier gas*. In this study, helium is employed as inert carrier gas. To achieve the separation, the differing adsorption probabilities and durations of the gas species constituting the analyte are exploited. The (average) time required to travel through the chromatographic column for a totally unretained compound is called *hold-up time* t_M[1]. For any other species, the (average) time needed to pass through the column is called the *retention time* t_R, which is t_M plus the *adjusted retention time* t'_R. In adsorption chromatography, t'_R corresponds to (average) total time the respective species spent as adsorptive during the travel through the column. This adjusted retention time t'_R is lesser for argon than for nitrogen, oxygen, and CO_2 on the employed zeolite Li-LSX. Hence, argon leaves the column first and can be trapped before the other species arrive. A simple model is introduced in the next section for the understanding of the separation process.

2.6.1 Theory of Plates

After the theory of plates, a theoretical plate is the hypothetical zone where the mobile phase equilibrates with the stationary. The separation performance of a chromatographic column increases with its number of theoretical plates. For three different species and a column with 200 plates, the relative concentrations were calculated for the different steps of movement and equilibration of the mobile phase with the stationary. The first plate represents the inlet of the column, while the last represents the outlet (containing the composition of the gas leaving the column). In each step, the mobile phase of nth plate travels into the $n + 1$th plate, and then equilibrates with the stationary phase of that plate. During the first ten steps, relative concentrations of 0.7 for species 1, 0.2 for species 2, and 0.1 for species 3 move into the first plate. At all other steps, relative concentrations of zero arrive at the first plate. The equilibria between mobile and stationary phase were set to 0.1:0.9 for species 1, 0.35:0.65 for species 2, and 0.5:0.5 for species 3 (meaning that species 1 is the one most adsorbed and species 3 the one the least adsorbed). The relative concentrations of the mobile phase for the steps 100, 200, 300 and 400 are plotted in Figure 2.7 (the respective relative concentrations of the stationary phase can be simply deduced from the equilibrium ratios). As only 1/10 of species 1 is located in the mobile phase, species 1 takes the longest time to travel through the column and its relative concentration in the mobile phase is not much higher than the one of the other species (although with 70 %, species 1 is the most abundant), while the least adsorbed species (3) is the fastest. Due to the repeatedly occurring steps of movement of the mobile phase and subsequent equilibration with the stationary phase, a separation between the different species occurs. However, for the same reason, the peaks are Gaussian broadened. The separation between the different species is the better, the more different the adsorption behavior is. Species 1 (90 % adsorbed) is easier to separate from species 2 (65 % adsorbed) than species 3 (50 % adsorbed) from species 2.

---

[1]Nomenclature after the recommendations of the International Union of Pure and Applied Chemistry [IUPAC, 2001].
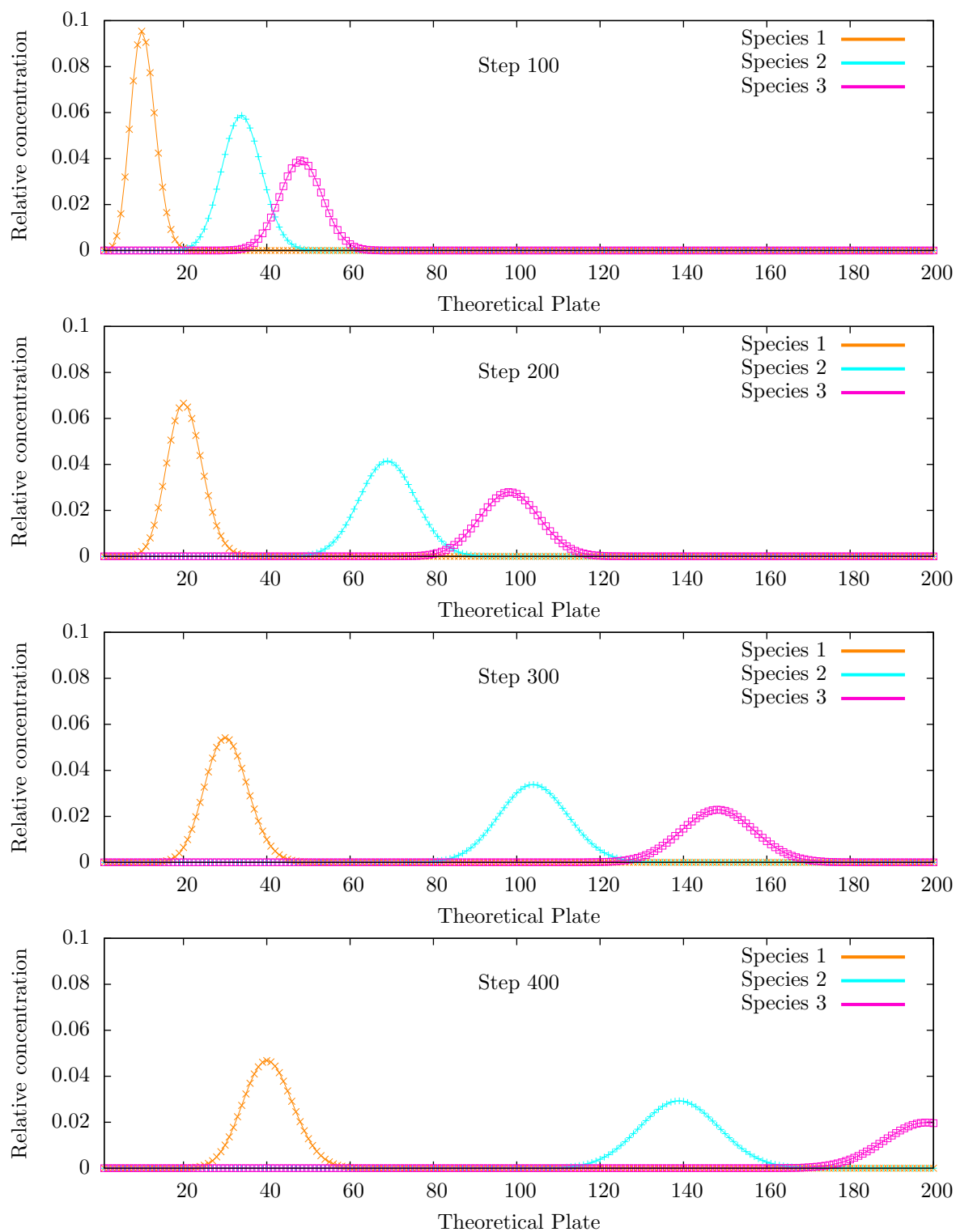
Figure 2.7: The relative concentrations of three different species in the mobile phase of the theoretical plates of a column at different steps of movement and subsequent equilibration of the mobile phase with the stationary phase in the theoretical plates.

The impact of the number of plates on the separation performance can also be illustrated using Figure 2.7. As the composition of the gas leaving the column is given by the last plate, the composition of the gas leaving a column having only 40 theoretical plates is seen in the 40th plate. In the 100th step, species 3 still has not totally left the 40th plate of the column, while species 2 already starts emerging at that plate. A complete separation of these species is consequently only possible with more than 40 plates. The parameters affecting the number of theoretical plates in a chromatographic column are discussed in the next section.

2.6.2   Separation Performance
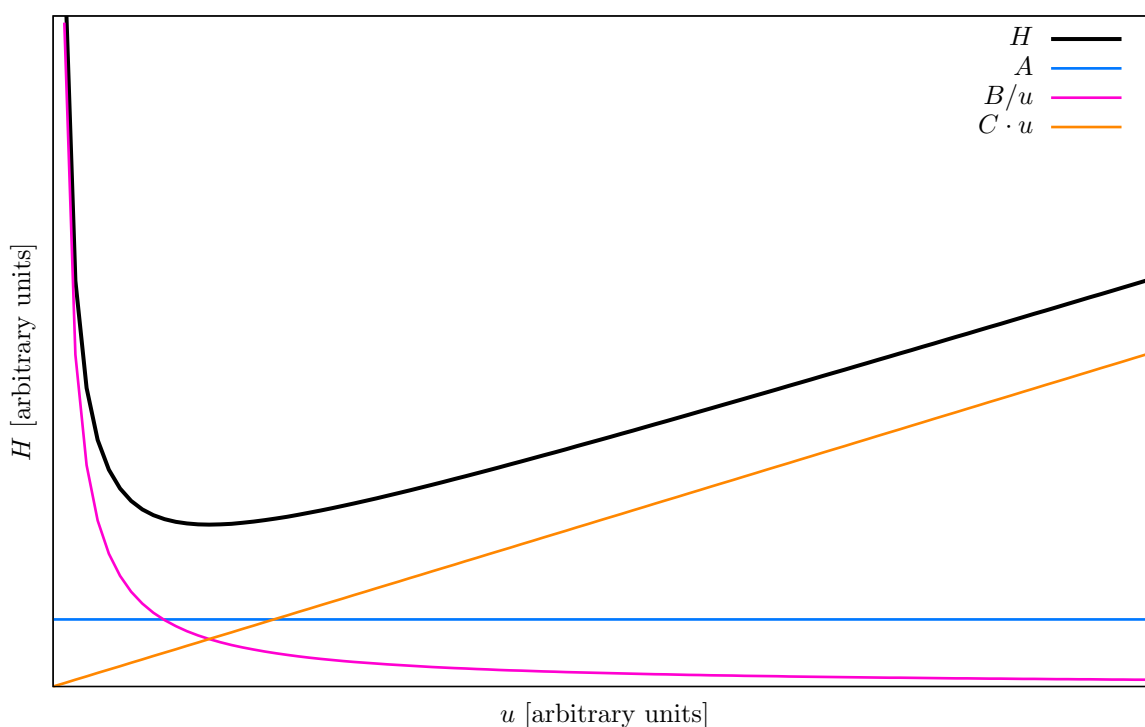
Figure 2.8: The Height Equivalent to a Theoretical Plate H as function of the linear gas velocity u after the Van Deemter equation. The term A accounts for the not perfectly homogeneous packing of the column, B is the diffusion term, and C considers the non instantaneous equilibration of the mobile phase with the stationary.

As was motivated in the last section, the separation performance increases with the number N of theoretical plates of the employed chromatographic column. For a given column of length L, N is equal to L divided by the Height Equivalent to a Theoretical Plate (HETP, or shorter H):

$$N = \frac{L}{H}\,. \tag{2.49}$$

The Van Deemter equation yields the following expression for H [Keulemans and Cremer, 1959; Ettre et al., 1996]:

$$H = A + \frac{B}{u} + C \cdot u, \tag{2.50}$$

where u is the linear gas velocity. The term A takes into account the not perfectly homogeneous packing of the column bed and reads $2 \cdot \lambda \cdot d_p$, with the packing factor λ ranging from 1 to 2, and the particle diameter d_p of the filling. B considers the diffusion of the analyte and is equal to $2 \cdot \gamma \cdot D_m$, where γ is the tortuosity factor for the column bed and D_m is the diffusion constant of the analyte in the mobile phase. At higher linear gas velocities, the diffusion of the analyte matters less and less. C describes the non instantaneous equilibration between the mobile and the stationary phase and reads $\omega \cdot d_p^2 / D_m$, with another packing factor ω ranging from 0.02 to 5 and accounting for radial diffusion. The higher u is, the less complete is the equilibration. Figure 2.8 shows H as function of u after the Van Deemter equation. At low linear gas velocities, the diffusion term dominates. With increasing u the influence of the diffusion decreases and H rises linearly with u due to the less and less complete equilibration. Chromatographic columns are mainly operated at linear gas velocities slightly above the optimum u, as not to risk operating at the left branch of the hyperbola, which is usually far steeper than the right.

For a given column, beside the temperature, u is one of the most important operation parameters. In the steady state, the particle flow $\dot{n}$ [particles per time] is the same for each cross section of the column. Assuming that the mobile phase behaves as ideal gas and the temperature T and the cross section A available for the flow are the same at any place x in the column, one arrives at the following equation:

$$const = \dot{n} \cdot \frac{R \cdot T}{A} = P_x \cdot \frac{\dot{V}_x}{A} = P_x \cdot u_x, \tag{2.51}$$

with the ideal gas constant R and the pressure P_x at place x. The behavior of the pressure in the column can be calculated after Keulemans and Cremer [1959] using Darcy´s law:

$$u = -\frac{k}{\mu} \frac{dp}{dx}, \tag{2.52}$$

with the permeability k of the column and the dynamic viscosity μ of the mobile phase. Knowing from Equation 2.51 that $P_x \cdot u_x$ is constant over the entire column, one can express the linear gas velocity u_x at any place x of the column with the linear gas velocity u_{out} and the pressure P_{out} at the outlet of the column:

$$u_x = u_{out} \frac{P_{out}}{P_x} = -\frac{k}{\mu} \frac{dp}{dx}. \tag{2.53}$$

Integration from the inlet of the column (x=0) to x and from the pressure P_{in} at the column inlet to P_x yields:

$$u_{out} \cdot P_{out} \cdot x = \frac{k}{2\mu} (P_{in}^2 - P_x^2). \tag{2.54}$$

The unknown parameters k/μ can be eliminated by plugging into the equation above the column length L for x and the pressure P_{out} at the outlet of the column for P_x. Then, solving the result

for k/μ and plugging this again in the equation above yields:

$$\frac{x}{L} = \frac{P_{in}^2 - P_x^2}{P_{in}^2 - P_{out}^2} . \tag{2.55}$$

This equation can be simply solved for P_x:

$$P_x = \sqrt{P_{in}^2 - \frac{x}{L}(P_{in}^2 - P_{out}^2)} . \tag{2.56}$$

With P_{out} and the linear gas velocity u_{out} at the outlet of the column, an expression for u_x is obtained:

$$u_x = u_{out}\frac{P_{out}}{P_x} = \frac{u_{out}P_{out}}{\sqrt{P_{in}^2 - \frac{x}{L}(P_{in}^2 - P_{out}^2)}} . \tag{2.57}$$

u_{out} can be calculated by integrating Equation 2.53 from $P_x = P_{in}$ to P_{out} and from $x = 0$ to L:

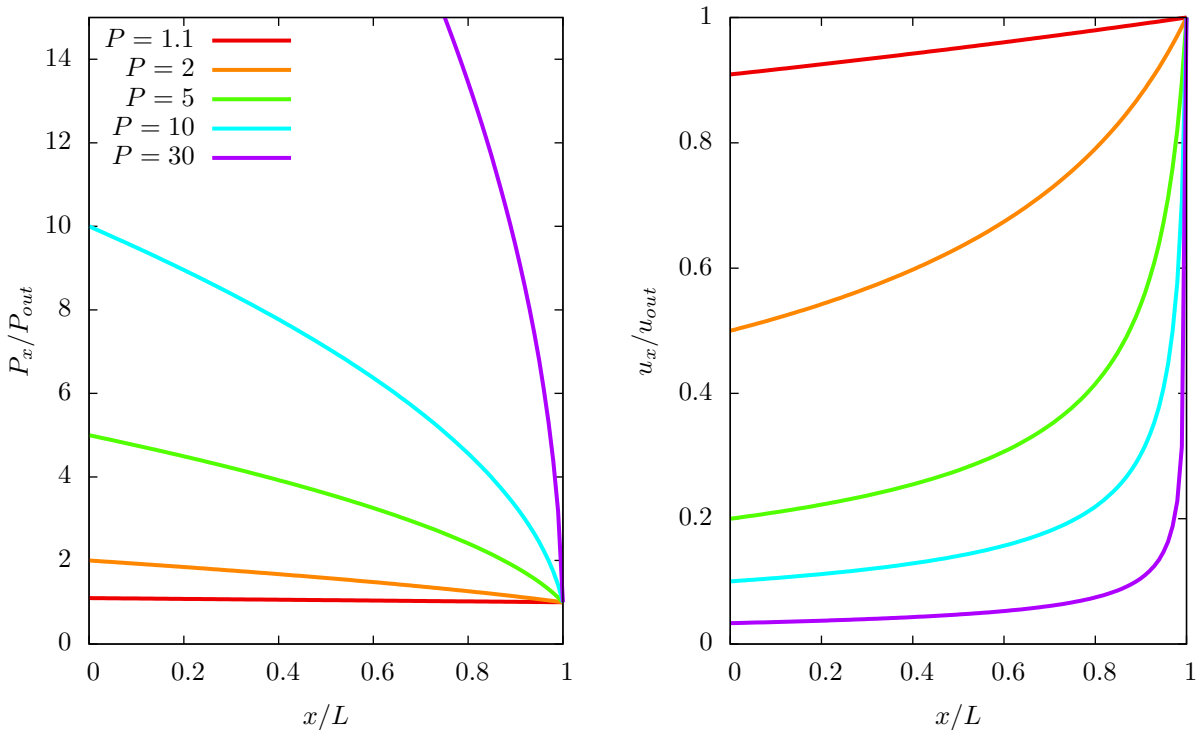$$u_{out} = \frac{k}{2\mu L}\left(\frac{P_{in}^2}{P_{out}} - P_{out}\right) . \tag{2.58}$$

Figure 2.9: The behavior of the pressure P_x and of the linear gas velocity u_x as function of the relative location in the column x/L for different pressure ratios P of the pressures at the column in- and outlet (after Keulemans and Cremer [1959]).

Figure 2.9 shows the behaviors of P_x/P_{out} and u_x/u_{out} as function of x/L for different pressure ratios $P = P_{in}/P_{out}$. The higher P is, the more heterogeneous is the distribution of P_x and u_x. In order to avoid parts of the column operating at unfavorable u_x, low P should be preferred. When the aim is to speed up the separation, the particle flow $\dot{n}$ [particles per time] through the column given by Equation 2.51 has to be increased:

$$\dot{n} = const = \frac{A}{R \cdot T} \cdot P_{out} u_{out} = const \cdot (P_{in}^2 - P_{out}^2) . \tag{2.59}$$

This should be always done by increasing P_{in} instead of decreasing P_{out}:

$$\Delta \dot{n} = \Delta_{P_{in}} \frac{\partial \dot{n}}{\partial P_{in}} = \Delta_{P_1} \cdot 2 P_{in} \tag{2.60}$$

$$\Delta \dot{n} = \Delta_{P_{out}} \frac{\partial \dot{n}}{\partial P_{out}} = - \Delta_{P_{out}} \cdot 2 P_{out} . \tag{2.61}$$

To achieve the same increase in $\dot{n}$, the pressure change $\Delta_{P_{out}}$ of P_{out} would have to be much higher than $\Delta_{P_{in}}$, since P_{in} is always greater than P_{out}. Another reason for changing $\dot{n}$ by adjusting P_{in} is that the pressure ratio P, which should be kept low, reacts much more sensible to changes of P_{out}:

$$\Delta_{in} P = \Delta_{P_{in}} \frac{1}{P_{out}} \tag{2.62}$$

$$\Delta_{out} P = - \Delta_{P_{out}} \frac{P_{in}}{P_{out}^2} . \tag{2.63}$$

Furthermore, the diffusion constant D_m of the analyte in the mobile phase is inversely proportional to the pressure Ettre et al. [1996], which also supports increasing P_{in} instead of decreasing P_{out}.

Short Summary of Recommendations regarding Separation Parameters

The separation of the different species of an analyte by means of a chromatographic column is the more complete the more different the adsorption behavior of those species is and the higher the number of theoretical plates of the column is. Looking back at equation for the selectivity S_{ik} (2.39), which describes how well two species i and k can be separated with a certain adsorbent, the following dependence of the adsorption behavior is seen:

$$S_{ik} = \frac{n_i/p_i}{n_k/p_k} \propto \exp \frac{\Delta H_k - \Delta H_i}{RT} .$$

n_i is the amount adsorbed of species i at the partial pressure p_i above the adsorbent and at temperature T, ΔH_i is the the isosteric heat of adsorption, which is negative, and R is the ideal gas constant. If species i is the one preferentially adsorbed, i.e. with the more negative ΔH, then the achieved separation gets better with increasing S_{ik}, i.e. with falling temperature. Hence, for a given column and differing isosteric heats of adsorption for the species of the analyte, the separation can be further enhanced by reducing the temperature of the column.
In addition, the separation performance can be increased by operating the column at the optimal linear gas velocity u_{opt}, which results in the maximum number of theoretical plates for that

column. Most columns are run at slightly higher velocities than u_{opt} as not to risk falling in the steeper left branch of the Van Deemter equation, where the number of plates sharply decreases. Several considerations have shown that u should be always increased by rising the inlet pressure of the column and not by decreasing the outlet pressure.

Chapter 3

Setup for Degassing Groundwater

Figure 3.1: The final setup for water degassing during a field trip, which is supplied with power by the alternating current generator (A). The water pump MP1, submersed in the well (B), is controlled by an adjustable converter (C). The water is pumped through the water filters (D) and degassed by the membrane contactor (E). The outlet of the vacuum pump (F) is connected with the compressor (G), which compresses the gas in the sample cylinder (H) to a pressure of up to 7 bar. Control parameters are read out by an analog to digital converter (I) and displayed with LabView software on a laptop (J).

3.1   Construction of the Setup

3.1.1   Requirements for the Setup

To facilitate an efficient and safe sampling for ATTA, the setup for degassing groundwater developed in this work should fulfill the following requirements:

- High degassing efficiency ($> 80\%$) and high water flow rates ($\approx 50\,\mathrm{L\,min^{-1}}$) should be possible at the same time in order to limit the sampling time to 1 or 2 hours (as between 1 and $3\,\mathrm{m^3}$ water have to be degassed to obtain $60\,\mathrm{LSTP}$ gas containing around $0.6\,\mathrm{LSTP}$ argon).

- The water system should have a low pressure drop, allowing to reach the desired water flow rates without additional pumps besides the submersible sample pump.

- It should be possible to operate the degassing setup in the field under various climatic conditions ($1\text{--}40\,^\circ\mathrm{C}$, extreme low or high humidities, rain).

- The setup should be robust and easy to ship. The single parts should only weigh as much as two persons still can carry and should be fast to reassemble in the field. This enables sampling remote wells not directly accessible by roads.

- The temperature of the sampled water, the pressure at the gas ports and the water inlet of the membrane contactor, the pressure in the sample container, the water flow rate, and the total water volume should be displayed and logged.

- Leak testing of the setup should be possible in the field without great efforts.

- Compression of the degassed gas into sample containers up to some bars should be possible in order to get along with smaller containers.

- All this should be implemented with the very minimum of the required resources.

After Section 2.1.3, maximally a relative sample contamination of 2% can be tolerated without falsifying the age of around 800 old groundwater by more than 50 years. The maximally acceptable leak rate of the setup for water degassing is calculated using rather unfavorable operation parameters as safety measure. A low water flow rate $\dot{V_l}$ of $20\,\mathrm{L\,min^{-1}}$ and a degassing efficiency η of 75% are assumed, as well as air equilibrated water containing a gas concentration C_l of around $20\,\mathrm{mLSTP/L}$. Most wells sampled so far contained even more gas per liter of water. The flow rate $\dot{V_g}$ of degassed air is:

$$\dot{V_g} = \eta \cdot \dot{V_l} \cdot C_l = 0.3\,\mathrm{LSTP/min}\,. \tag{3.1}$$

With the maximum tolerable sample contamination of 2%, this corresponds to an acceptable leak rate of $0.1\,\mathrm{mbar\,L\,s^{-1}}$. The components were selected considering these requirements.

| Company | DIC | | Membrana | |
| Series | Separel | | Liqui-Cel Extra Flow | |
Model	EF-040P	4x28	6x28	10x28
Max. water flow rate V_l [L min^{-1}]	83	113	183	950
η_{O_2}(25 °C,V_l=80 L min^{-1},P_{lumen}=67 mbar) [%]	93.5	81	≈ 90	≥ 95
ΔP @ max. V_l [mbar]	n.a.	650	800	400
Operating temp. [°C]	2–50	1–70	1–70	1–70
Weight (dry) [kg]	n.a.	4.1–6.4	10.4	33–93
Membrane area [m^3]	40	20	42	130
Membrane material	PMP	PP	PP	PP
Membrane type	SS	X40	X40	X40
Housing material	PVC	PP/FRP/SS	ABS	FRP/SS
Hollow fiber OD/ID [µm]	215/135	300/200	300/200	300/200
Length [mm]	673	890	1012	1186
Diameter [mm]	180	114	168	279.4
Volume shellside/lumenside [L]	6.6/n.a.	4.2/1.1	6.7/2.3	23.4/9
Relative cost [1]	1.8	n.a.	1	n.a.

Table 3.1: The data compiled here are taken from Membrana [2007b],Membrana [2007c],Membrana [2007a], Membrana [2012], and DIC Corporation, [2007]. The degassing efficiency η_{O_2} of the 6x28 Extra-Flow contactor in vacuum mode is an estimation based on a comparison of the η_{O_2} of the Extra-Flow contactors above in vacuum and combo mode (the data sheet of the 6x28 contactor only has data for combo mode). While "SS" in line "Membrane type" actually is a type, "SS" in line "Membrane material" is a material code for stainless steal. The maximum operation temperature as well as the dry weight depend on the housing material.

3.1.2   Component Selection

Membrane Contactor

Concerning membrane contactors, it was found that Membrana and DIC are the most prominent manufacturers having the best supply with data sheets. Membrane contactors of these companies also have applications in the work of Probst [2007] and Ohta et al. [2009]. An overview of the products best fitting the requirements is compiled in Table 3.1. The Liqui-Cel 6x28 Extra-Flow contactor was chosen for the degassing setup since it allows higher water flow rates and has a better degassing efficiency than the 4x28 contactor without being much heavier (which was the reason to discard the 10x28 contactor). Besides, compared to EF-040P from DIC, the 6x28 Extra-Flow membrane contactor costs much less, has a comparable degassing efficiency, and a more complete data sheet as well as detailed operating instructions are available. Contactors of the Extra-Flow series are distributed with either X40 or X50 fibers. Having a porosity of 25 %, X40 fibers are best suited for degassing oxygen and let less water vapor pass the membrane than X50 fibers [Ulbricht, R., 2009]. The latter have a porosity of 40 % and are suitable for degassing waters with huge amounts of dissolved gases or CO_2. To keep the condensation of water vapor in the system as low as possible, and since Ar in its properties is more alike O_2 than alike CO_2, the 6x28 Extra-Flow membrane contactor with X40 fibers is better suited.

Gas Pumps

For the degassing setup, a pump is needed for vacuum generation at the gas ports of the membrane contactor and to compress the sample gas into containers. The sealing of the pump should be oil-free in order to avoid oil vapor in the system. Additionally, the pump should have a very low leak rate and tolerate the condensation of water vapor. Membrana, the manufacturer of the chosen membrance contactor, uses a model on the basis of measured data to compute the required suction capacity of the pump. To keep a vacuum of 66 mbar at the gas ports of the chosen 6x28 Extra-Flow membrane contactor for 15 °C water temperature, a suction capacity of $50\,\mathrm{L\,min^{-1}}$ is needed [Ulbricht, R., 2009]. Usually liquid ring pumps are deployed in industrial degassing applications. As they are sealed through a water film, there are no problems caused by condensation. Unlike for most industrial applications, the gas degassed from sample water is no waste product and possible sources of contamination have to be considered. Since gas exchange between the degassed gas and the water film will occur, utilizing liquid ring pumps for the setup is no option. Usual oil-free air compressors have to be discarded as well, because they always have leak rates which increase with the lifecycle and they cannot cope with high humidities of the pumped medium [Richardt, 2009]. Gas-tight pumps can only be membrane pumps [Richardt, 2009]. Pumps of the manufacturer KNF Neuberger have been chosen as already good experiences have previously been made [Reichel, 2009], their products are the most solid and suitable for field applications, the communication is fast, and their quotations are lower compared to the competitors. However, no single membrane pump was found being able to generate the required vacuum of 66 mbar and compress the sample gas to a pressure of 7 bar at the same time for a volume flow of $50\,\mathrm{L\,min^{-1}}$. For that reason, two pumps were ordered (see Table 3.2 for specifications). As the degassing performance of the membrane contactor essentially depends on the vacuum at the gas ports, the membrane pump with the highest suction capacity available was chosen for the vacuum generation (N0150.3AP.9E). Another membrane pump having a lower suction capacity above 50 mbar but a higher below was discarded, because pumping in the range of the partial pressure of water causes much more water vapor to pass the membrane. For the compression of sample gas, the membrane pump with the highest outlet pressure (7 bar) and the highest suction capacity at that pressure was chosen (N145.1.2AP.9E). Even at the maximum outlet pressure, the compressor still has a better suction performance [L(STP)/min] than the vacuum pump at inlet pressures below 250 mbar. Because of that, it is unlikely that the maximum overpressure at the outlet of the vacuum pump of 0.1 bar will be exceeded when both pumps are connected in series. Actually, as the compressor is overdesigned compared to the vacuum pump, the latter will benefit from pressures below atmospheric pressure at its outlet, reaching an even lower vacuum.

Water Filter

For degassing groundwater with the 6x28 Liqui-Cel Extra-Flow membrane contactor, a 5 µm cascade filter is recommended [Ulbricht, R., 2009] to prevent the accumulation of suspended particles in the membrane. An inexpensive and satisfying solution was found using "Causa"-filters from Infiltec GmbH (see Table 3.3 for specifications). The cascade filter was implemented by installing a prefilter (25 µm-Causapure) and a secondary filter (5 µm-Causagard) in series. Together, their initial flow resistance is still less than 1 mbar/(L/min). The housing is the same for both filter cartridges, allowing for water flows up to 76 L/min. As all filter cartridges of Infiltec are standardized to fit these housings, one can easily employ other kinds of cartridges if

Model	N0150.3AP.9E	N145.1.2AP.9E
Achievable vacuum [mbar]	20	n.a.
Suction capacity at 66 mbar [L/min] / [L(STP)/min]	≈40 / ≈2.5	n.a.
Maximum overpressure at outlet [bar]	0.1	7
Suction capacity at 7 bar oulet pressure [L(STP)/min]	n.a.	15
Engine power [W]	1000	350
Starting current [A]	7	3
Current consumption [A]	2.3	2.1
Ingress protection rating	IP54	IP54
Weight [kg]	28.5	15
Operating temp. [°C]	5 - 40	5 - 40
Maximum leak rate [mbar·L/s]	$6 \cdot 10^{-3}$	$6 \cdot 10^{-3}$

Table 3.2: Specifications of the employed membrane pumps from KNF Neuberger. The data are taken from KNF Neuberger GmbH, [2009], KNF Neuberger GmbH, [2008], and Reitzel [2010].

required.

Pressure Gauges

The pressures at the gas ports and the water inlet of the membrane contactor, as well as of the gas in the sample cylinder have to be measured and logged. Pressure gauges with built-in displays and/or data logging function proved to be much too expensive. Instead, pressure transducers with analog output are used. They are read out, displayed, and logged using an analog to digital converter (RedLab 1208LS) and LabVIEW software running on a labtop. The most inexpensive pressure transducers still fulfilling the operating conditions were quoted by WIKA Alexander Wiegand SE & Co. KG (see Table 3.4 for specifications). For monitoring the pressure at the gas ports, a transducer with the range 0-1.6 bar was installed, for the other positions transducers with the range 0-10 bar.

Temperature Sensor

For the same reasons as for the pressure gauges, a temperature sensor with an analog output was chosen and read out, displayed, and logged, using an analog to digital converter (RedLab 1208LS) and LabVIEW software running on a laptop. The used resistance thermometer TR30 from WIKA Alexander Wiegand SE & Co. KG has a measuring range of -50 - 150 °C (see Table 3.4 for other specifications).

Water Flow Meter

Being more than one order of magnitude cheaper than other water flow meters, an usual residential water meter is used for the setup for water degassing. As only the total water volume flown through the water meter is displayed, one has to divide the volume flowed through in a certain time by the time to get the average water flow rate. The residential water meter ETK/ETW Modularis from Rossweiner Armaturen und Messgeräte GmbH & Co. oHG has an accuracy of ±1 %. Its flow resistance increases exponentially with water flow, reaching around 180 mbar at 30 L/min, 500 mbar at 60 L/min, and 1000 mbar at 80 L/min [Rossweiner GmbH & Co. oHG,].

Filter Cartridge	Causapure 25 µm	Causagard 5 µm
Max. water flow rate V_l [L/min]	76	76
Flow resistance [mbar/(L/min)]	≈ 0.4	≈ 0.4
Absorption capacity [g]	260	140
Operating temp. (cartridge) [°C]	1–60	1–80
Operating temp. (housing) [°C]	1–52	1–52
Max. diff. pressure at 20 °C [bar]	3.2	4.2
ID / OD [mm]	28 / 63	28 / 63
Length [mm]	508	508
Cartridge material	PP	PP
Housing material	PP	PP
Cartridge weight (dry) [kg]	0.28	0.36
Housing weight (dry) [kg]	2	2
Particle size [µm]	Filtration efficiency [%]	
1	0	75.9
3	0	91.2
5	18	> 99.9
10	37	> 99.9
20	56	> 99.9
30	83	> 99.9
50	95	> 99.9

Table 3.3: Specifications of the water filters of the degassing setup. The date are taken from Infiltec GmbH, [2010c], Infiltec GmbH, [2010a], and Infiltec GmbH, [2010b].

	Pressure transducer A-10	Resistance thermometer TR30
Operating temp. [°C]	0–80	-40–85
Analog output	1–5 V	4–20 mA
Non-linearity [% full range]	±0.5	n.a.
Accuracy [% full range]	±1	±0.1
Supply voltage [VDC]	8–30	10–36
Ingress protection rating	IP67	IP67

Table 3.4: Specifications of the pressure transducer type A-10 and resistance thermometer TR30 from WIKA Alexander Wiegand SE & Co. KG . The date are taken from WIKA Alexander Wiegand SE & Co. KG, [2009a] and WIKA Alexander Wiegand SE & Co. KG, [2009b].

Measurement range	0–1.6 bar	0–10 bar	− 50–150°C
Resolution	3.9 mbar	24.4 mbar	0.24 °C
Accuracy	±16 mbar	±100 mbar	±0.2 °C

Table 3.5: The measurement range of the sensors employed in the setup for water degassing, the resolution resulting from the data read-out using the analog to digital converter RedLab 1208LS, and the accuracy of the sensors is listed. Looking at the latter, it is clear that the achieved resolution is more than sufficient.

3.1.3 Electronics - Data Read-Out

As already mentioned, the analog signals of the pressure gauges and the temperature sensor are read out and converted to digits using a RedLab 1208LS analog to digital converter, then displayed and logged with LabVIEW software running on a labtop. The RedLab 1208LS has 8 singled-ended 11 bit inputs with an input range ±10 V. In order not to miss cable breaks or other failure, for the pressure transducers 1–5 V outputs were chosen instead of the also available 0–10 V output. The same is true for the resistance thermometer, where a 4–20 mA output was ordered, which can be transformed into 2–10 V using a 500 Ω resistance. Taking these outputs instead of the 0–10 V results in worse resolutions, which are still more than sufficient in regard to the accuracy of the sensors (see Table 3.5). A LabVIEW program developed by Schäfer [2009] has been adapted, reading out and logging the measurements of the sensors with 1 Hz and displaying the current value and the trend.

3.1.4 Design

For the connection, assembly and placing of the single components (membrane contactor, gas pumps, water filters), several considerations have to be taken into account [Membrana, 2012; Reitzel, 2010]. In systems with less than 10 membrane contactors, the contactors should be vertically mounted, which helps keeping the lumen free of water. The water has to enter the membrane contactor from the bottom and exit it from the top. In addition, the gas piping should be sloped away from the contactor to facilitate the draining of the condensed water on the lumen side. Also, the membrane pumps should be located at the highest position of the system to hamper the accumulation of condensate in the pumps. For that reason, the gas ports of the membrane contactor are connected with the pumps via a flexible tubing (Swagelok JNW2FH25-36.00), being sloped away both from the contactor and the pumps. As the tubing has an inner diameter of 25.4 mm and a length of 914 mm, the effective suction capacity of the pumps suffers only slightly from this connection and there is enough space for possible condensate to accumulate. Beyond that, the used flexible tubing possesses KF-25 flanges on the ends, enabling to join two parts of the setup within an instant. This also favors the splitting of the whole setup in several parts, making it easier to carry in the field. Neither the membrane contactor nor the water filters should be exposed to direct sunlight. It is recommended to store the contactor in an opaque box. Because of that, filters and contactor were mounted in a closable aluminium box with the dimensions 760 mm × 1160 mm × 400 mm (width × height × depth). This also facilitates the transport and shipping of the setup. To inhibit biological growth, the membrane contactor can be evacuated and sealed by closing valves V1, V2, and V3 (see Figure

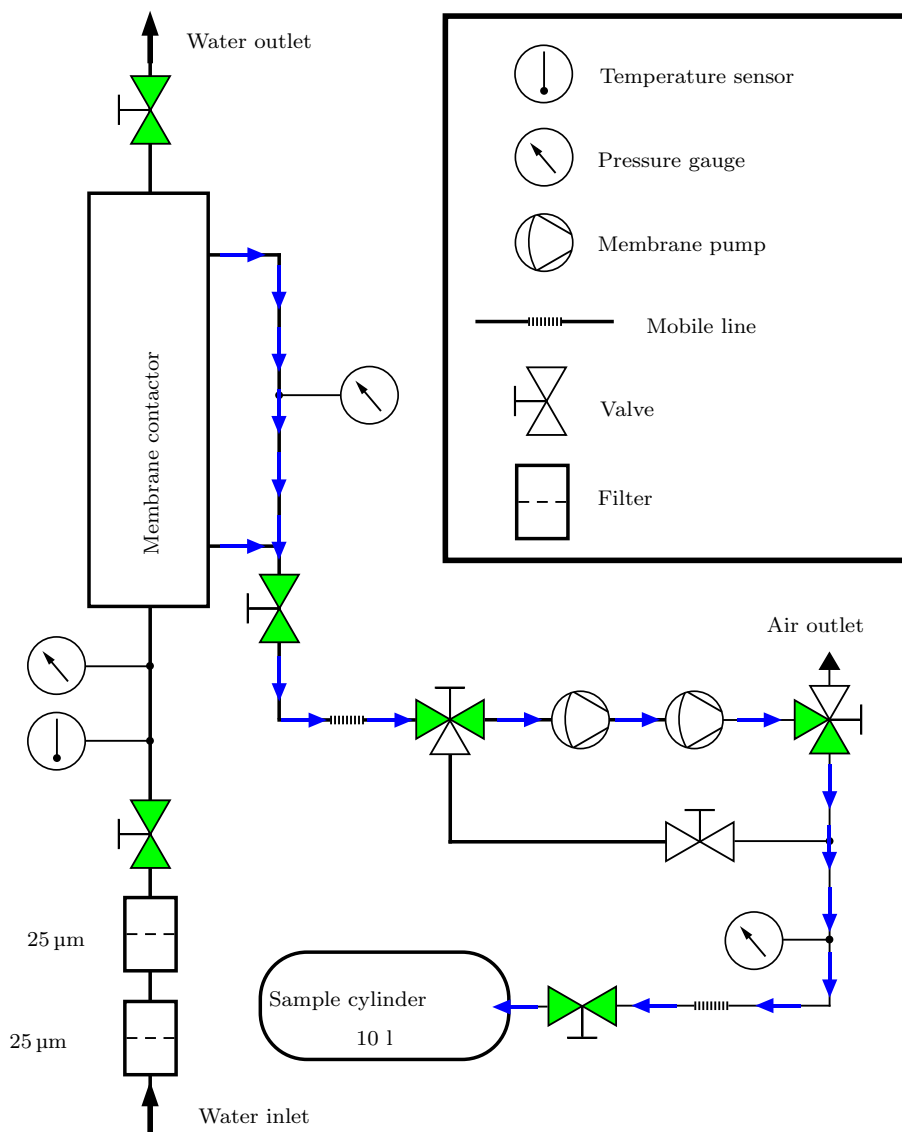3.2), holding the vacuum until next use.

Figure 3.2: Schematic of the setup for water degassing, showing the valve positions during degassing (open valves are filled with green, closed valves with white).

3.2 Test of the Setup

3.2.1 Operation Procedure for Water Degassing

The single steps during water degassing are listed here. Figure 3.2 shows a schematic of the setup.

Leak Testing

Initially, all valves are closed. The membrane contactor, isolated by the valves 1, 2 and 3, should be still evacuated since the last use. The sample cylinder contains around 2 bar nitrogen.

- The outlet of the membrane pumps is connected via valve 5 with the air outlet and the membrane pumps are turned on. The inlet of the pumps is connected via valve 4 with valve 3 (which stays closed). The pressure in the membrane contactor is checked. If it is not significantly above the pressure of the last shutdown, one can continue according to the next point. Otherwise valve 3 is opened and the contactor is evacuated to around 50 mbar. Then valve 3 is closed again and the pressure is monitored. Depending on the pressure increase, the degassing can be continued or the leak has to be identified.

- Valve 3 is opened to avoid pressure building up during the introduction of the water. The water outlet (valve 2) is opened, then valve 1 is gently opened and the water is slowly introduced without risking a water hammer. Shortly afterwards, valve 3 can be closed again. From this point on, the shellside of the contactor is flushed with sample water.

- The inlet of the pumps is connected via valve 4 and valve 6 with valve 7 (which stays closed). When the pressure before the sample container falls below 50 mbar, the inlet of the membrane pumps is connected via valve 4 with valve 3 (which stays closed). Then the pressure before the sample container is monitored. If no pressure increase occurs, one can continue.

- Valve 6 is closed and the outlet of membrane pumps is connected via valve 5 with valve 7 (which stays closed) and the pressure before the sample container is monitored. If the pressure does not rise any further after the initial pressure increase, the connection between the contactor and the pumps has no leaks and one can continue.

- The outlet of the pumps is connected via valve 5 with the air outlet. The inlet of the pumps is connected via valve 6 with valve 7, which stays closed until the pressure before the sample container falls below 50 mbar. Then valve 6 is closed, valve 7 is opened, and the pressure of the nitrogen in the container is checked. If the pressure is not much less than during the filling in the laboratory, the container apparently has no leaks and can be evacuated to around 50 mbar by opening valve 6. The nitrogen pumped out of the container serves to flush the volume of the pumps.

Water Degassing

- Valve 6 is closed and the inlet of the pumps is connected via valve 4 with valve 3, which can then be opened.

- 100 L of water are degassed to flush the nitrogen out of the pumps. In the case of air equilibrated water [Weiss, 1970], around 2 L gas are dissolved in that amount of water. Wells sampled so far contained even more gas per liter of water. This means, by degassing 100 L of water the combined volume of the pumps of around 0.68 L is at least replaced thrice.

- The outlet of the pumps is now connected via valve 5 with the sample container, filling it with the degassed air until a pressure of 7 bar is reached. Then the outlet of the pumps is again connected via valve 5 with the air outlet and valve 7 is closed.

Shutdown

The water inlet (valve 1) and the water outlet (valve 2) are closed and the contactor is evacuated to around 50 mbar, then valve 3 is closed. The flexible tubing between valve 3 and 4 is disassembled and ambient air is pumped to remove condensed water from the membrane pumps. For longer shutdowns, the water in the membrane contactor can be pushed out by opening valve 1 and 2 and by connecting the air outlet of the pump with valve 2 (using hoses not shown on Figure 3.2). This also causes the water filters to be backflushed and partly freed of accumulated particles. Later, valve 3 can be opened and valve 1 closed in order to flush out the possibly condensed water on the lumenside.

3.2.2 Oxygen Degassing Efficiency as Function of Different Parameters

As the concentration of oxygen in water is easy to measure using dissolved oxygen sensors, effects of the water flow rate, the water temperature, and the pressure at the gas ports on the oxygen degassing efficiency η_{O_2} were investigated at first.
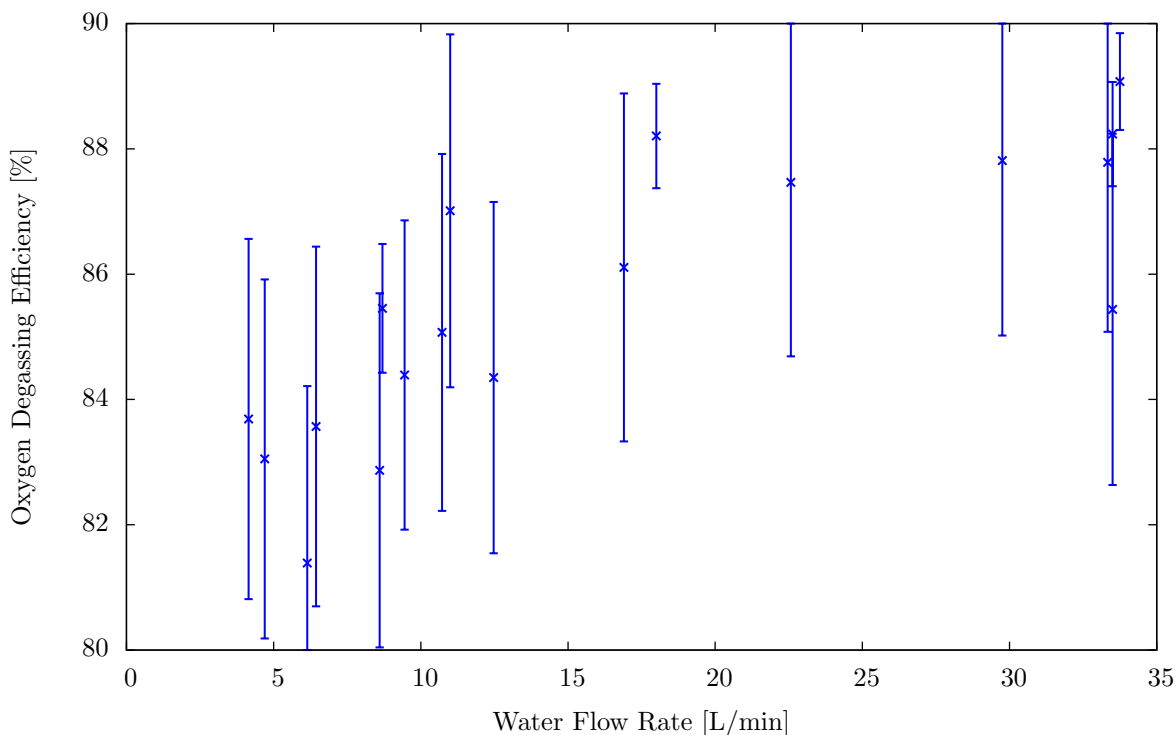

Figure 3.3: The oxygen degassing efficiency as a function of the water flow rate. Probably due to flow channeling in the contactor at lower flow rates, the degassing efficiency is lower than for higher flows.

$\eta_{\mathbf{O_2}}$ as a Function of Water Flow Rate

In order to determine η_{O_2} of the setup for water degassing, a barrel of around 125 L volume was filled with tap water. The oxygen concentration C_{barrel} in the barrel was measured using a Hydrolab MS5 oxygen probe (1–5 % measurement accuracy, depending on approach flow [Hach Company,, 2006]). For some of the experiments, a CellOx 325 dissolved oxygen sensor from WTW was used instead ($\pm 0.2\,\mathrm{mg\,L^{-1}}$ [WTW GmbH & Co. KG,, 2002]). The water was pumped through the setup at different water flow rates and degassed (each fill of the barrel with a fixed rate). The degassed water was fed into a bucket, where the oxygen concentration $C_{degassed}$ was measured. The degassing efficiency η is calculated as follows:

$$\eta = 1 - \frac{C_{degassed}}{C_{barrel}}. \tag{3.2}$$

Figure 3.3 shows the results. Surprisingly, η is higher for high water flow rates than for lower ones. After Equation 2.20 the inverse is expected (at higher flow rates the residence time of the water in the contactor and the contact with the gas phase is shorter). A possible reason might be flow channeling in the contactor at lower water flow rates, which decreases the effective membrane surface and thus the degassing efficiency. A stronger effect of back dissolution of oxygen at lower flow rates is also possible. The expected decrease of η with increasing water flow rate is likely to occur at flows closer to the maximum flow rate of the membrane contactor, which is $183\,\mathrm{L\,min^{-1}}$. With the used water pump only flow rates up to $33.5\,\mathrm{L\,min^{-1}}$ could be investigated. During the experiments, the water temperature ranged from 19 to 23 °C, the dissolved oxygen in the tap water was between 7.1 and $8.2\,\mathrm{mg\,L^{-1}}$, and the pressure at the gas ports lied between 40 and 60 mbar.

$\eta_{\mathbf{O_2}}$ as a Function of Water Temperature

The oxygen degassing efficiency of the setup for water degassing was investigated in the bachelor thesis of Kollefrath [2011] for temperatures between 10 and 20 °C at water flow rates of 7.8 and $32.4\,\mathrm{L\,min^{-1}}$. Due to the lower diffusivities at lower temperatures a decreasing η_{O_2} with sinking temperature is expected, but in this temperature range no temperature dependence of η_{O_2} was observed.

$\eta_{\mathbf{O_2}}$ as a Function of the Pressure at the Gas Ports

As the driving force for mass transfer across the membrane in hollow fiber membrane contactors is the concentration gradient, η_{O_2} should react very sensitively to an increase of the pressure at the gas ports of the contactor. This was investigated in the bachelor thesis of Kollefrath [2011] at a water flow rate of $16.8\,\mathrm{L\,min^{-1}}$. The results are listed in Table 3.6 and clearly indicate that a higher pressure dramatically decreases η_{O_2}.

Discussion

In the investigated range of water flow rates (4–$33.5\,\mathrm{L\,min^{-1}}$) η_{O_2} shows no significant dependence on the flow. The small decrease of η_{O_2} at very low flow rates might be due to flow channeling in the contactor or even an artifact caused by back dissolution of oxygen in the bucket at these low flows. Kollefrath [2011] found no significant change in η_{O_2} between 10 and 20 °C, but a strong decrease of η_{O_2} with increasing pressure at the gas ports of the contactor.

Pressure [mbar]	η_{O_2} [%]
50	77
80	67
95	64
120	59
160	55
180	52
200	48

Table 3.6: The oxygen degassing efficiency η_{O_2} of the setup for different pressures at the gas ports of the membrane contactor. The values are taken from the bachelor thesis of Kollefrath [2011].

All in all this indicates that the 6x28 Liqui-Cel Extra Flow membrane contactor with a maximum water flow of $183\,\mathrm{L\,min^{-1}}$ is a good choice. Afar from the maximum flow, η_{O_2}does not decrease with decreasing temperatures nor with increasing water flow rates as a benefit of the overdimensioning.

3.2.3   Degassing Efficiency for Different Isotopes

During a test campaign in the Schwetzinger Hard, water samples for noble gas measurements were taken from five wells. For two of these wells, also samples of the degassed water leaving the setup for water degassing were taken. The samples were measured with the sector field mass spectrometer MM5400 described in Wieser [2010]. The degassing efficiency of the measured isotopes is calculated as follows:

$$\eta = 1 - \frac{C_{degassed}}{C_{well}} \, , \tag{3.3}$$

with the concentration $C_{degassed}$ of the isotope in the degassed water and the concentration C_{well} of the isotope in the well water. Since the gas concentration in the degassed water is decreased, longer copper tubes were used for the degassed samples than for the well water. To increase the reliability of the data further, two samples of degassed water were taken per well. The results in % are listed in Table 3.7. Since η is expected to increase with increasing diffusion coefficient D of the gas in water and decreasing solubility (or increasing Henry coefficient K_H), D and K_H are also given. The heavier is the noble gas, the smaller is D and the larger is K_H. Hence η should decrease with increasing noble gas mass. For Ar, Kr, and Xe this relation seems to hold, with $\eta_{Ar} > \eta_{Kr} > \eta_{Xe}$. However, η_{He} and η_{Ne} show an unexpected behavior: $\eta_{Ar} > \eta_{Kr} \approx \eta_{Ne} > \eta_{He} > \eta_{Xe}$. Back diffusion of He and Ne from the atmosphere through the PVC-hose of the water outlet of the setup could be a possible reason.
The relative difference of the degassing efficiency of the argon isotopes $(1 - \eta_{^{36}Ar}/\eta_{^{40}Ar})$ is around $(0.9 \pm 0.4)\,\%$ for the first well. For the second well, it is $(0.3 \pm 0.4)\,\%$ and $(-0.1 \pm 0.4)\,\%$. For ^{39}Ar this difference would be even less, since ^{39}Ar differs less in mass from ^{40}Ar (and in D and K_H) than ^{36}Ar. Judging from these two wells, during degassing, no significant fractionation of ^{39}Ar and ^{40}Ar seems to occur, which would alter the isotope ratio and thus cause additional dating errors .

Sample	^{3}He	^{4}He	^{20}Ne	^{22}Ne	^{36}Ar	^{40}Ar	^{84}Kr	^{132}Xe
SH F10/2	83.5	83.1	86.73	86.84	89.3	90.16	87.0	82.1
SH F10/2	85.6	84.3	87.56	87.66	n.a.	90.96	88.4	83.6
SH F10/3	84.6	83.9	87.12	87.21	90.1	89.98	87.0	80.6
SH F10/3	85.0	84.1	87.49	87.55	90.2	90.45	87.4	81.8
Error	0.6	0.3	0.08	0.07	0.4	0.04	0.3	0.6
D	8.3^a	7.22^a	4.16^a	4.10^{a,b}	2.59^b	2.57^b	1.84^a	1.47^a
K_H	1.092E-1	1.073E-1	8.392E-2	8.375E-2	2.133E-2	2.130E-2	1.079E-2	5.541E-3

Table 3.7: The degassing efficiency for different noble gas isotopes in %. The errors are around the same for the samples and are also given in %. The diffusion coefficients D of the gases in water at $25\,°$C are given in $10^{-5}\,cm^2\,s^{-1}$ and are taken from Jähne et al. [1987]^a and Bourg [2008]^b. The dimensionless Henry coefficients K_H (the ratio of the volumetric concentrations of the gas in the atmosphere above the water to that in the water) for $6\,°$C are taken from Weiss [1971] for ^{4}He and ^{20}Ne, from Weiss [1970] for ^{40}Ar, from Weiss and Kyser [1978] for ^{84}Kr, and from Clever [1979] for ^{132}Xe. The Henry coefficients for the rare isotopes are calculated using the isotope fractionation factors reported in Benson and Krause Jr. [1980] for ^{3}He and in Beyerle et al. [2000] for ^{22}Ne and ^{36}Ar.

During this work, the water of several wells in the Hessisches Ried (HR), in the Fontainebleau Sands Aquifer near Paris (P4 and P5), and in the Schwetzinger Hard (SH) were degassed with the degassing setup for ^{39}Ar dating of the groundwater. For some of these wells, the noble gases in the water, in the degassed water, in the degassed air, and in the separated argon were measured with the sector field mass spectrometer MM5400 described in Wieser [2010]. The helium, neon and argon isotope ratios of these measurements are compiled in Table 3.8.

For all wells but HR 544264 no significant change in the ^{4}He/^{3}He ratio can be observed for the degassed air compared to the well water, so that the result of HR 544264 is likely an outlier. The much lower ^{4}He/^{3}He ratios of the separated argon arise from the use of helium as carrier gas in the setup for argon separation. This helium issues from underground gas deposits, which are enriched in radiogenic ^{4}He and thus have a lower ^{4}He/^{3}He ratio.

The ^{20}Ne/^{22}Ne ratios are close to the atmospheric value (9.8) for all water, degassed water, air and argon samples, with the exception of the separated argon of the wells HR 544259 (9.96) and HR 544264 (9.65), which might just be coincidence.

The ^{40}Ar/^{36}Ar ratios of the well water samples are close to the atmospheric value (295.5) for all but two wells. During the measurement run of the water samples from the Hessisches Ried, several failures occurred at the MM5400 and the overall precision of noble gas measurements was worse than usually. Because of that, the results of these water samples should not be overemphasized. The two samples per well scatter around the atmospheric value for HR 544255 (308.6 and 291.2) and for HR 544264 (279.8 and 325.3), though. The ^{40}Ar/^{36}Ar ratios of the degassed water and degassed air samples are in agreement within the errors with the atmospheric value. Exceptions are the degassed air samples of wells HR 544259 (292.8) and P5 (278.7). While the deviation from the atmospheric value of HR 544259 is still not significant, the degassed air of P5 was remeasured and a more atmospheric value was obtained (296.4). The ^{40}Ar/^{36}Ar ratios of the separated argon coincide with errors with the atmospheric value.

All this points at the conclusion that the few exceptions are outliers and no significant fractionation occurs for He, Ne and Ar neither during degassing nor during separation. For all wells

Sample Well	Kind of Sample	^{4}He/^{3}He	Δ^4He/^{3}He	^{20}Ne/^{22}Ne	Δ^{20}Ne/^{22}Ne	^{40}Ar/^{36}Ar	Δ^{40}Ar/^{36}Ar
Atm. value		7.1E+05	6.6E+03	9.80	0.080	295.5	0.5
HR 544255	well water	6.6E+05	4.0E+04	9.76	0.006	308.6	4.5
HR 544255	well water	6.7E+05	4.0E+04	9.78	0.006	291.2	4.0
HR 544255	degassed air	6.0E+05	1.9E+04	9.80	0.006	294.7	1.1
HR 544255	degassed air	5.7E+05	1.8E+04	9.80	0.005	295.1	1.1
HR 544255	separated Ar	5.7E+06	1.8E+05	9.77	0.006	296.2	1.1
HR 544259	well water	2.6E+06	1.6E+05	9.78	0.006	294.1	4.0
HR 544259	well water	2.6E+06	1.6E+05	9.81	0.006	294.7	4.0
HR 544259	degassed air	2.4E+06	7.7E+04	9.78	0.005	292.8	1.2
HR 544259	separated Ar	5.9E+06	1.9E+05	9.96	0.006	296.8	1.1
HR 544264	well water	2.6E+05	1.6E+04	9.81	0.008	279.8	3.8
HR 544264	well water	1.9E+05	1.2E+04	9.82	0.008	325.3	4.6
HR 544264	degassed air	6.5E+05	2.4E+05	9.80	0.005	295.8	1.1
HR 544264	separated Ar	6.3E+06	2.1E+05	9.65	0.005	295.8	1.1
P4	well water	6.6E+05	2.1E+04	9.79	0.062	294.5	2.4
P4	well water	6.4E+05	2.3E+04	9.78	0.037	293.5	3.4
P4	degassed air	6.3E+05	2.3E+04	9.77	0.005	295.8	1.1
P5	well water	7.5E+05	2.5E+04	9.79	0.064	294.0	2.6
P5	well water	6.8E+05	2.3E+04	9.78	0.035	289.2	3.3
P5	degassed air	6.8E+05	2.2E+04	9.77	0.005	278.7	1.1
P5	degassed air	7.0E+05	2.3E+04	9.78	0.005	296.4	1.2
SH F10/2	well water	6.0E+05	1.6E+04	9.78	0.004	296.8	1.9
SH F10/2	degassed water	6.2E+05	2.0E+04	9.82	0.004	295.5	2.0
SH F10/2	degassed water	6.5E+05	2.2E+04	9.81	0.004	296.2	2.0
SH F10/3	well water	7.7E+05	2.2E+04	9.79	0.004	296.0	2.0
SH F10/3	degassed water	8.1E+05	2.8E+04	9.82	0.004	295.8	1.9
SH F10/3	degassed water	8.2E+05	2.8E+04	9.83	0.005	293.8	2.0

Table 3.8: A compilation of noble gas isotope ratio data from well water, air degassed with the degassing setup from the well water, and argon separated from that air. The atmospheric values are taken from [Porcelli et al., 2002].

the temperature of the sampled water was between 10.7 and 12.8 °C. For higher temperatures fractionation effects are even less likely. At least for temperatures down to 10.7 °C fractionation during degassing can be excluded.

3.2.4   Extracted Gas Amounts per Liter of Water

During the first sampling trips in the Hessisches Ried and Schwetzinger Hardt, eight wells were sampled. The extracted gas amount per liter of water V_{gas}/V_{water}, the water flow rate F_{water}, the pressure at the gas ports of the membrane contactor $P_{gas\ port}$, the total extracted gas amount V_{gas}, the total amount of degassed water V_{water}, and the water temperature T_{water} during the sampling are compiled in Table 3.9. V_{gas}/V_{water} varies strongly for the different wells due to
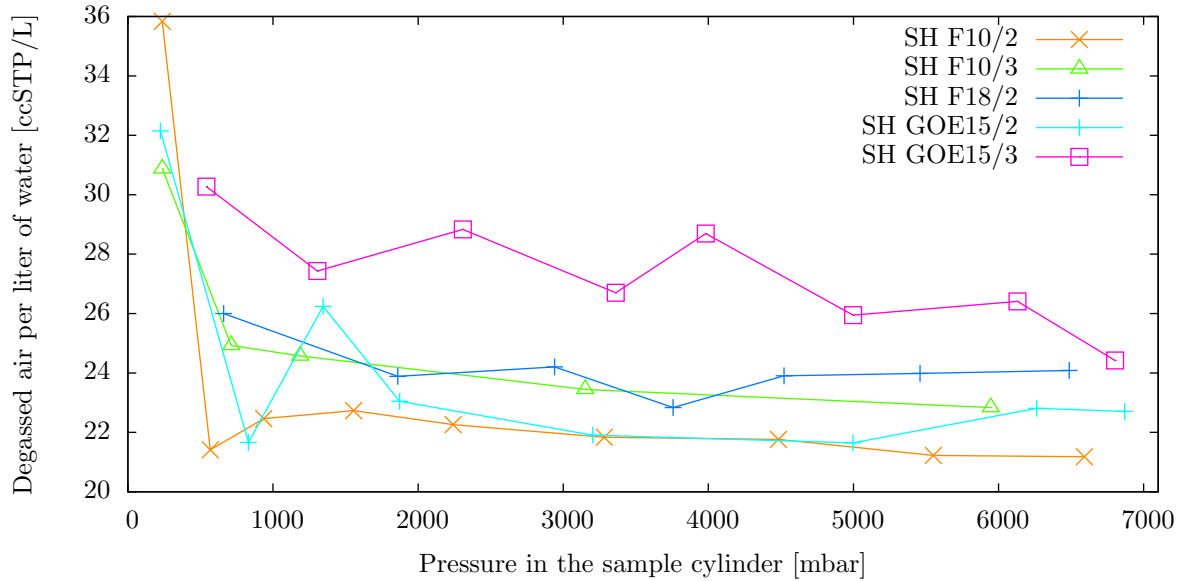
Figure 3.4: The extracted gas amount in ccSTP per liter of water during the sampling in the Schwetzinger Hardt. Around 100 L of water are degassed to flush the volume of the pumps before the sample cylinder is filled with degassed air. The apparently higher extracted gas amounts per liter of water at the beginning result from the degassed air in the pump volume at the beginning of the filling of the cylinder.

the differing gas contents of the wells. For wells with lesser V_{gas}/V_{water}, more water has to be degassed to reach the same V_{gas}. The lower values of $P_{gas\ port}$ belong to the beginning of the filling of the sample gas cylinder, and the higher ones to the end, when the pumps have to work against the higher pressure P_{sample} in the cylinder. $P_{gas\ port}$ increases also slightly with increasing V_{gas}/V_{water}, as more gas has to be pumped. That the variations of $P_{gas\ port}$ for an empty and full cylinder and for strongly varying V_{gas}/V_{water} still are small is a sign that the pumps are well dimensioned.

In Figure 3.4, V_{gas}/V_{water} is plotted versus the pressure in the sample cylinder for the five wells of the Schwetzinger Hardt. At the start of the filling of the sample cylinder, the pump volume is already filled with extracted gas from the flushing, thus V_{gas}/V_{water} only seems to be higher. Overall, V_{gas}/V_{water} is quite constant. For some wells, it decreases with time, which is probably caused by a decreasing degassing efficiency (P_{sample} and $P_{gas\ port}$ both increase during the filling of the cylinder, and the degassing efficiency strongly decreases with $P_{gas\ port}$). Although observable, this effect is still negligibly small due to the dimensioning of the pumps.

Well	F_{water} [L/min]	V_{gas}/V_{water} [ccSTP/L]	$P_{gas\ port}$ [mbar]	V_{gas} [LSTP]	V_{water} [L]	T_{water} [°C]
HR 544255	24.9	36.8	$42.8 - 55.6$	54.2	1472	11.8
HR 544259	n. a.	24.1	$51.3 - 55.6$	53.9	2240	12.6
HR 544264	22.8	55.0	$51.3 - 59.8$	54.2	985	11
SH F10/2	36.1	21.8	$30.0 - 51.3$	59.7	2668	11.3
SH F10/3	27.5	23.4	$38.5 - 51.3$	59.3	2489	12.8
SH F18/2	29	23.9	$38.5 - 51.3$	59.7	2461	10.7
SH GOE15/2	29.4	22.3	$38.5 - 51.3$	59.7	2632	11.2
SH GOE15/3	28.8	27.1	$38.5 - 55.6$	59.3	2152	12.8

Table 3.9: The water flow rate F_{water}, the extracted gas amount per liter of water V_{gas}/V_{water}, the pressure at the gas ports of the membrane contactor $P_{gas\ port}$, the total extracted gas amount V_{gas}, the total amount of degassed water V_{water}, and the water temperature T_{water} during the sampling trips in the Hessisches Ried and Schwetzinger Hardt.

Chapter 4

Setup for Argon Separation

4.1 Construction of the Setup

4.1.1 Requirements for the Setup

The setup for argon separation developed in this work should fulfill the following requirements:

- In order to enable comparison measurements between ATTA and the underground laboratory in Bern (low level counting, LLC), large air samples of around 60 LSTP, as required for LLC, have to be processed by the setup for argon separation. This should be possible in one run without splitting the samples.

- As little argon as possible should be lost during the separation.

- Since the count rate of ATTA depends on the argon purity and gettering is expensive, the purity of the separated argon should at least reach 95 %. Using the getter of the ATTA setup to remove the last 5 % impurity of up to 0.6 LSTP of separated argon then costs less than 5 \$ per sample.

- The setup should be able to process samples of different size.

- The operation parameters (the temperature of the separation columns, the pressures before and after the columns, the pressure in the sample container) should be displayed and logged.

- Leak testing of the setup should be possible before operation without great efforts.

- All this should be implemented with the very minimum of the required resources. Also, the helium and liquid nitrogen consumption should be as low as possible.
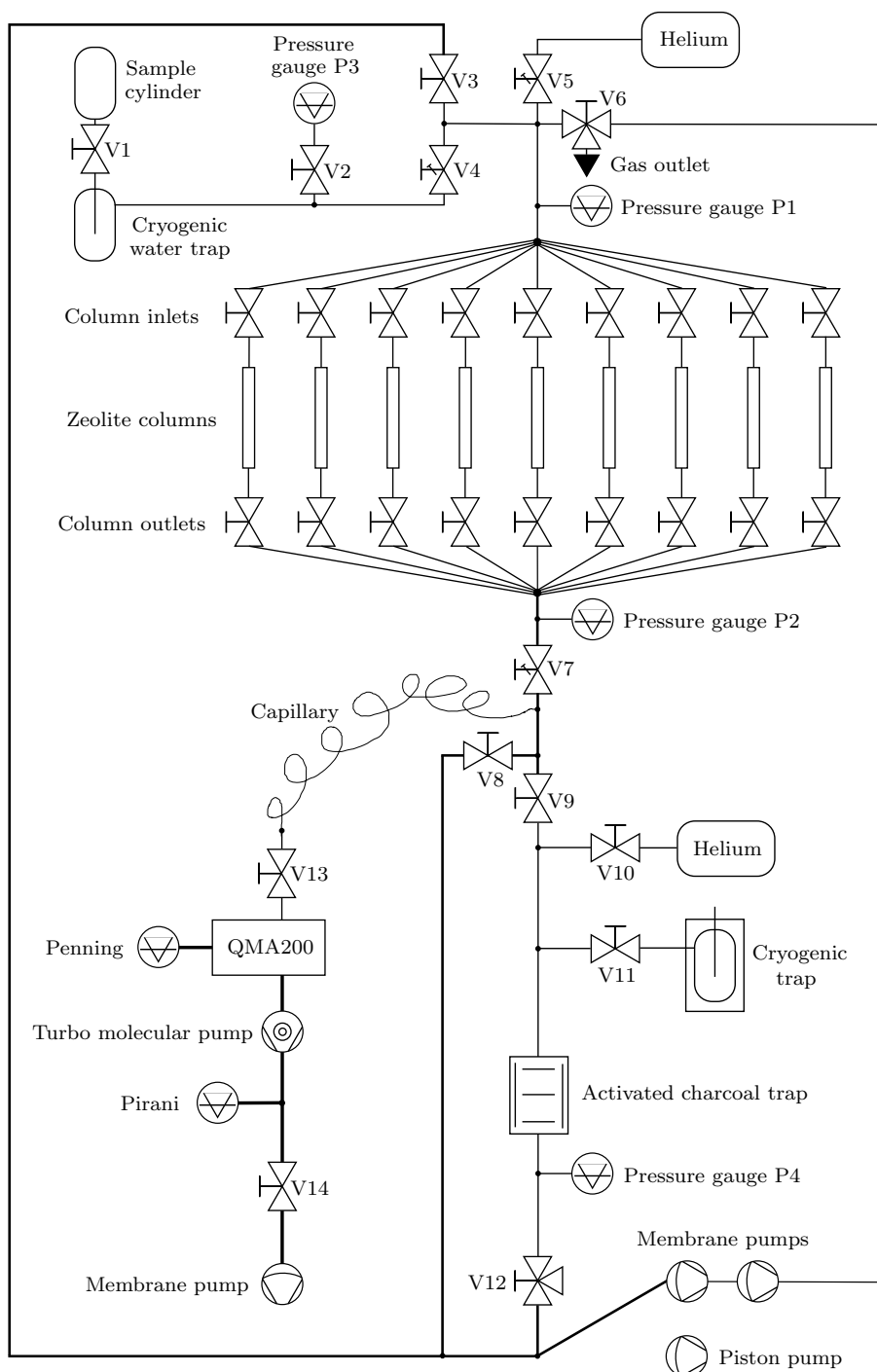
4.1.2 Design

Figure 4.1: A schematic of the setup for argon separation.

The design of the setup for argon separation resembles the one developed by Riedmann [2011] and is shown in Figure 4.1. The separation takes place in the zeolite columns, which are filled with an adsorbent. First, the sample gas is frozen over from the sample container to the cooled columns, passing through a water trap. Then the gas is flushed through the columns, using helium as carrier gas. The helium is recycled to keep the consumption low. As nitrogen and oxygen interact stronger with the adsorbent, argon leaves the columns first and is trapped in the cooled activated carbon trap (ACT). This separation strongly depends on temperature, which is adjusted by a combination of cooling with liquid nitrogen and heating via the ohmic resistance of the columns. The composition of the gas leaving the columns is observed with a quadrupol mass spectrometer (QMA200 from Pfeiffer Vacuum). When the entire argon peak is loaded on the ACT, the separation can be stopped. Thereafter, helium is pumped out of the still cooled ACT. Without this step, nitrogen and oxygen just would have been replaced by helium. Then the ACT is heated to around $100\,^\circ$C and the composition of the separated argon is checked again with the QMA200. Afterwards, the argon is frozen over to the cryogenic trap, which serves as transport vessel to the ATTA setup. The columns are regenerated at $220\,^\circ$C and the ACT at $100\,^\circ$C. Helium ports at two places enable flushing the columns and the ACT. During the separation, the membrane pumps of the setup for water degassing are used to recycle the helium (see Section 3.1.2 for technical data). The piston pump, having a far lower suction capacity but a much better end vacuum, is connected to the setup during regeneration.

4.1.3 Selection of the Adsorbent

As seen in Section 2.6.2, for a good separation, the adsorbate - adsorbent interaction potential ϕ should differ as much as possible for the different species of the analyte. In Section 2.5.4 it has been motivated why the adsorbent employed to separate argon from nitrogen and oxygen should be a zeolite: the quadrupole moment Q is virtually the only property affecting ϕ in which these gases differ, and zeolites, having cations dispersed above the negatively charged oxides on their surfaces, are the only adsorbents having an electric field gradient $\dot{F}$. The proportionality of the contribution $\phi_{\dot{F}Q}$ of the interaction between Q and $\dot{F}$ to the total ϕ is:

$$\phi_{\dot{F}Q} \propto \frac{qQ}{r^3}\,,$$

with $r = r_i$ (ionic radius) $+ r_j$ (adsorbate molecule), and the electronic charge of the ion q. To maximize $\phi_{\dot{F}Q}$, r_i should be as small as possible and q as high as possible. However, another contribution to ϕ increases with q^2 and at the same rate for all these species. Thus, the relative difference of the ϕ of the different gas species would decrease with higher than monovalent q and the separation performance would decrease. The smallest, monovalent ion Li$^+$ is consequently the best suited extra framework cation. Zeolites with the maximum number of Li$^+$ as extra framework cations are consequently the best choice. As pointed out in Section 2.5.5, the number of extra framework cations in zeolites increases with the exchange of Si for Al. Hence, the zeolite should have a preferable low silica (LS) content. Because of all that, zeolite Li-LSX is the optimum adsorbent for the separation of argon from air. This choice is confirmed by Kurzhals [2009] ("From my information, Li-LSX is state of the art in adsorptive gas separation.") and Yang [2003] ("Since the invention in 1989, LiLSX has been the sorbent of choice for air separation").

4.1.4   Shape and Filling of the Separation Columns

Riedmann [2011] found that around 3200 mL (or 1.71 kg) of zeolite Li-LSX (Zeox Z12-07 0.4–0.8 mm from Zeochem AG) are required to separate 80 L gas with the setup described in Section 4.1.2. One has to consider that the separation performance worsens with increasing inner diameter of the column [Grob, 1995]. As Riedmann [2011] still achieves a good separation with an inner diameter of 10 mm, that diameter is also used for the setup developed in this work. Compared to Riedmann [2011], a slightly shorter total filled column length of 38.05 m is chosen, corresponding to a filling quantity of 2988 mL and a separation capacity for 74.7 L gas. The segmentation in several smaller columns of equal size and shape is determined by the chosen dewar, which is raised over the columns from below and partly filled with liquid nitrogen (LN). Only at first, for a faster cooling to the target temperature, the columns have contact with the LN. Later, during the experiment, solely the swirled, cold nitrogen atmosphere cools the columns. Space for 30 L LN is left below the columns, allowing for an uninterrupted cooling during long experiments. Another factor affecting the shape of the columns is the minimal bending radius of the used tube, which is 38.4 mm [Dockweiler AG,, 1993]. It is imperative for all columns to have exactly the same shape and filling. Only then the peaks running through the different columns will merge at the confluence of the column exits, when the columns are arranged in parallel. Having only one column would cause a too high flow resistance. Another advantage of the splitting in several columns is the modularity [Riedmann, 2011]. By providing the in- and outlets of each column with valves, one can use any suitable number of columns for the separation, depending on the sample gas size. The Cryo Anlagenbau GmbH made by far the best quotation for the dewar, which is also the one used by Riedmann [2011] (800 mm inner height, 400 mm inner diameter). Using the same column inner diameter, almost the same zeolite quantity, and the same dewar, the geometry and arrangement of the columns is nearly that of Riedmann [2011]. It consists of nine equal sized and shaped columns, each having 3 elongated coils and a volume of 322 mL (see Figure 4.2). The columns were bent and produced by Dockweiler AG (Neustadt-Glewe), using stainless steel 316L cleaned after TCC.1 procedure. The filling of the columns was performed following the recommendations of Grob [1995] and von Holzen, W. [2009] to achieve a tight packing with minimal particle fracturing. Fine metal wool was fixed in one end of the precoiled column and a pump was connected. A funnel was attached to the other end. While pumping and gently tapping the column, small incremental amounts of zeolite were added, until the column was completely filled and the zeolite bed stopped moving during tapping. Then metal wool was also inserted in this end to fix the zeolite bed. On both ends, adapters to smaller diameters were welded and valves were mounted. This was repeated for all columns. Then the valves were joined using the material PEEK (polyether ether ketone) in order to insulate the columns electrically from each other and from the rest of the setup. This is of importance as the columns are heated via their ohmic resistance (see next section).

Figure 4.2: One of the nine columns before installation. The length of the column as it can be seen here is 528 mm, while the length before bending is 4229 mm. The inner and outer diameter of the tubing are 10 mm and 12 mm, respectively. Photo by [Dockweiler AG,, 2009].

4.1.5   Temperature Control of the Separation Columns

The operation temperatures of the columns during the separation process (≈ -130°C) differ vastly from those during the regeneration of the columns (≈ 220 °C). Especially during the separation a homogeneous cooling of all columns is required, or the argon peaks of the different columns will not converge and possibly merge with the oxygen peaks. As was experienced in an earlier work [Reichel, 2009], the use of a well mixed medium around the columns is the optimum for a homogeneous cooling or heating. However, media with the required temperatures are hard to come by (only -78°C can be reached with a dry ice isopropanol mixture and 100 °C with boiling water). Riedmann [2011] found an elegant solution: A dewar partly filled with liquid nitrogen (LN, -196°C) is raised over the columns, isolating them from the ambient temperature. In the middle of the columns a rotor swirls the nitrogen atmosphere in order to provide for a homogeneous temperature. At first, the bottom parts of the columns reach into the LN, which quickens the cooling. Later, after some LN evaporated and the columns do not tap into the LN anymore, the columns are solely cooled by the evaporating nitrogen. The stainless steel columns can be heated via their ohmic resistance R:

$$P = U \cdot I = R \cdot I^2, \tag{4.1}$$

with the electric power P, the voltage U, and the current I. To prevent electrical shorts, teflon spacers are fixed between the coils of the columns, sustaining temperatures from -200 to 260 °C. By applying a heating power equal to the cooling power of the nitrogen atmosphere, the target temperature can be held once it is reached. Also, when the dewar is lowered, the columns can be heated to more than 220 °C for regeneration by applying higher currents.

Figure 4.3: The setup for argon separation. During the separation, the dewar partly filled with liquid nitrogen is lifted in the upper position, insulating thermally and cooling the zeolite columns with a swirled, cold nitrogen atmosphere. When the columns are heated for regeneration, the dewar is moved back into the lower position as shown on the figure.

Implementation of the Temperature Control and the Heating

The heating is supplied by a 32 A power line (230 V alternating current). This supply is managed by an automated thyristor switch (ESGT-1Ph35 from RS Elektroniksysteme GmbH), controlling the power output by phase cutting. The thyristor itself is driven by a 0–10 V input signal. This signal either can be manually adjusted via a potentiometer or automatically by a PID controller (ENDA EUC442 PID Universal Regler). Three PT100 temperature sensors are installed at the columns and the PID controller can be connected to either of them via a switch. The controller compares the measured temperature with the entered target temperature and lowers or raises the input signal of the thyristor. The voltage output of the thyristor is then connected with the columns via a 6 kW transformer (coil ratio 1:7), transforming 230 V to around 33 V. Always three columns are connected in series, and the three triplets are then in parallel circuit. The total ohmic resistance of this assembly is equal to that of a single column, which is around 0.091 Ω. A total heating power of around 4.5 kW is possible with this configuration, being limited by the maximum current of the primary circuit (32 A). Heating the columns to the target temperature of 220 °C takes around 10–15 min and the complete power of the transformer (6 kW) can be used, without any fuses melting during this short term overcurrent. Keeping the columns then at that temperature requires only around 2.6 kW. For an arrangement of all columns in parallel circuit, the maximum current would be reached at lower voltages, resulting in a maximum heating power of only 0.5 kW. Likewise, the power of all columns in series would be limited by the higher ohmic resistance, reaching only 1.3 kW.

4.1.6 Dimensioning of the Fused Silica Capillary

In order to monitor the composition of the gas leaving the separation columns with the quadrupole mass spectrometer, low vacuum (10–1000 mbar) has to be connected with high vacuum (in this setup $\approx 1 \times 10^{-7}$–1×10^{-5} mbar) without significantly changing these pressures. A narrow capillary possessing a low conductance C is suitable for this task. The required theory is taken from Jousten [2005]. In the following a steady isothermal flow is assumed. C is defined as the throughput Q [mbar L s^{-1}] per pressure difference between the inlet pressure P_1 and the outlet pressure P_2, and is the inverse of the flow resistance R:

$$C = \frac{Q}{P_1 - P_2} = \frac{1}{R}. \tag{4.2}$$

The total flow resistance R of several resistances R_i in series or in parallel is calculated as for ohmic resistances:

$$R = \sum_{i=1} R_i = \sum_{i=1} \frac{1}{C_i} = \frac{1}{C} \qquad\qquad R_i \text{ in series}, \tag{4.3}$$

$$\frac{1}{R} = \sum_{i=1} \frac{1}{R_i} = \sum_{i=1} C_i = C \qquad\qquad R_i \text{ in parallel.} \tag{4.4}$$

The flow in long conductances can be laminar or turbulent. Depending on that, C is calculated for one flow type or the other. The Reynolds number Re can help to decide which is the case:

$$Re = \frac{\rho \cdot v \cdot d}{\mu}, \tag{4.5}$$

with the density ρ, the flow velocity v, and the dynamic viscosity μ of the flowing gas, and the characteristic length d of the conductance, which is here the inner diameter. For a tube with a round cross sectional area (such as the used capillary), the flow is laminar for $Re < 2300$, and turbulent for $Re > 4000$. v can be calculated using the volumetric flow rate $\dot{V} = Q/P$ [L s^{-1}] and the cross sectional area $A = \pi \cdot d^2/4$:

$$ v = \frac{\dot{V}}{A} = \frac{4}{\pi \cdot d^2} \cdot \frac{Q}{P} \, . \tag{4.6} $$

Plugging v into Equation 4.5 yields:

$$ Re = \frac{\rho \cdot v \cdot d}{\mu} = \frac{4}{\pi} \cdot \frac{\rho \cdot Q}{P \cdot \mu \cdot d} = \frac{32}{\pi^2} \cdot \frac{Q}{\mu \cdot \bar{c}^2 \cdot d} \, . \tag{4.7} $$

$\bar{c}$ is the mean gas velocity:

$$ \bar{c} = \sqrt{\frac{8 \cdot R \cdot T}{\pi \cdot M}} \, , \tag{4.8} $$

with the ideal gas constant R, the temperature T (in Kelvin), and the molar weight M of the gas flowing through the conductance. For a steady isothermal flow, Q and $\bar{c}$ are constant. Hence Re is the same everywhere and can be calculated for any place along the flow path. Since helium is employed as carrier gas during the separation and is the main constituent flowing through the conductance, all calculations will be carried out using the properties of helium (such as the dynamic viscosity for example). With a maximum pressure of 1×10^{-5} mbar and a volume flow rate of 50 L s^{-1} at the exit of the capillary (corresponding to the suction capacity for helium of the employed turbo molecular pump), Re is 0.14 at maximum (for a inner diameter of the capillary of 40 µm and 293 K). Therefore the flow is laminar and additional flow resistances caused by turbulence do not need to be considered.

During the experiment, the pressure in the capillary lies between 1×10^{-7} and 700 mbar. In the high pressure part of the capillary, collisions between the gas particles are far more frequent than between gas particles and the wall of the capillary. The gas can be considered to be continuous and the flow is viscous. In the lower pressure part, the mean free path of the gas molecules is in the range of the inner diameter of the capillary or even larger. The gas particles collide more often with the walls of the capillary than with other gas particles and the flow is molecular. Hence, in the capillary, the flow is neither purely viscous nor purely molecular. By assuming two tubes in parallel, one with a viscous conductance C_{visc}, and the other with a molecular conductance C_{mol}, one arrives at the following equation for the overall conductance of the capillary:

$$ C \approx C_{visc} + C_{mol} \, . \tag{4.9} $$

It describes the limiting cases correctly and is an approximation in the transient area. For a tube with a round cross sectional area it reads:

$$ C \approx \frac{\pi}{256} \cdot \frac{1}{\mu} \cdot \frac{d^4}{l} \cdot (P_1 + P_2) + \frac{\bar{c} \cdot \pi}{12} \cdot \frac{d^3}{l} \, , \tag{4.10} $$

with the pressures P_1 and P_2 at the entrance and at the exit of the capillary, and the length of the capillary l.
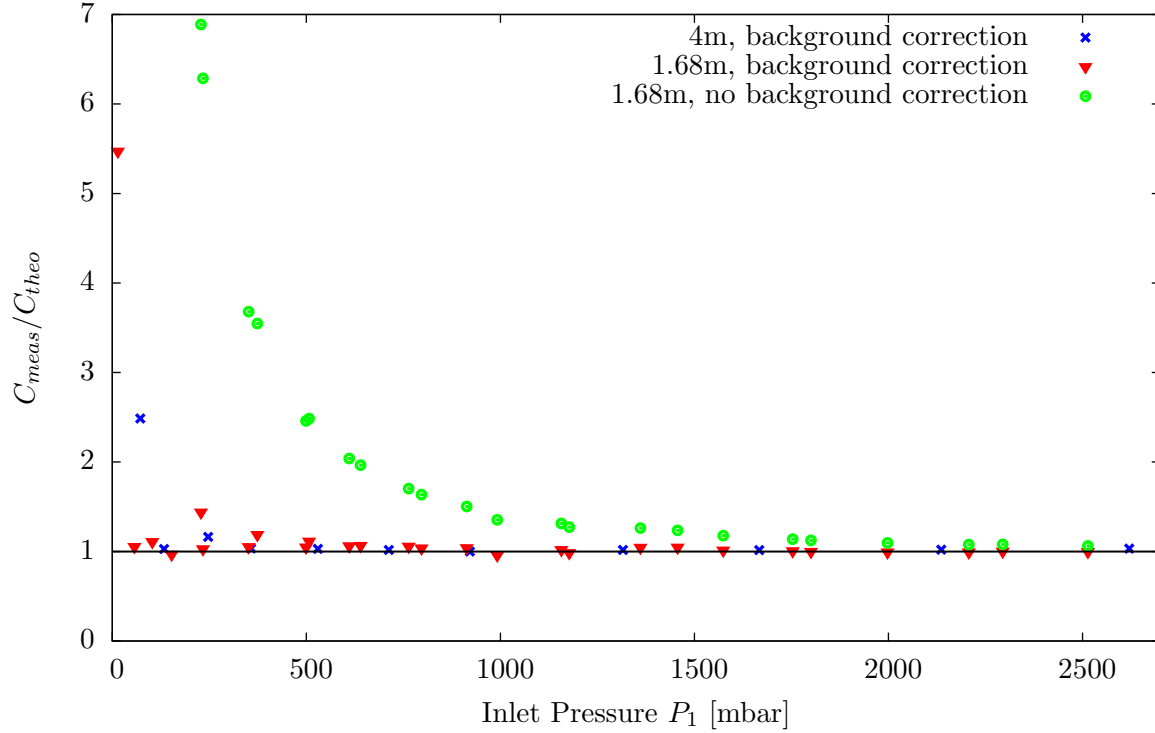
Figure 4.4: C_{meas}/C_{theo} for different capillary lengths, with and without correction for background gases in the high vacuum part of the setup. By fitting the ratio to a value of 1 the effective suction capacity S_{eff} of the turbo molecular pump at the measurement chamber of the quadrupole mass spectrometer can be determined.

The signal of the employed quadrupole mass spectrometer (QMA200 from Pfeiffer Vacuum) increases linearly with the pressure in the measurement chamber only up to a pressure of 5×10^{-7} mbar and flattens at higher pressures [Wonneberger, 2008]. P_2 should not exceed that pressure for the maximally occurring P_1, which is around 700 mbar during the separation. Equation 4.10 was solved for l. Then the l fulfilling the requirement concerning the pressures was calculated for the different inner diameters of the available capillaries. A fused silica capillary (ID 40 μm, OD 365 μm, length 4 m) was ordered from Postnova and installed using nanotight fittings (peek hex short 1/16", also from Postnova). Usually, such capillaries are employed in field flow fractionation experiments with pressures up to 100 bar. However no leaks were found and the fittings also seem to be suited for vacuum applications. P_2 can be neglected as $P_2 << P_1$, and the theoretical value C_{theo} after Equation 4.10 is for the chosen capillary:

$$C_{theo} \approx C_{visc} + C_{mol} = 4.22 \times 10^{-14} \cdot P_1 + 5.21 \times 10^{-12} \qquad [\mathrm{m^3\,s^{-1}}], \qquad (4.11)$$

with P_2 in mbar. The theoretical values calculated with this equation should be in agreement with the measured values yielded by Equation 4.2 ($C_{meas} = Q_C/(P_1 - P_2) \approx Q_C/P_1$). However, the throughput $Q_C = \dot{V} \cdot P$ flowing through the capillary is not well known. The only known volume flow rate $\dot{V}$ in the system is the suction capacity S of the turbo molecular pump ($50\,\mathrm{L\,s^{-1}}$ for helium), and the only pressures measured are P_{QMS} in the measurement chamber of the QMS

and P_1 at the entrance of the capillary. The effective suction capacity S_{eff} of the pump at the measurement chamber is lower than S due to the conductances connecting the pump with the chamber. The balance of the different throughputs flowing in and out of the measurement chamber is:

$$S_{eff} \cdot P_{QMS} = Q_C + Q_B, \tag{4.12}$$

with the constant flow Q_B of background gases, which is independent of the pressure. For different inlet pressures, P_{QMS} was measured, and C_{meas} as well as C_{theo} calculated. The ratio C_{meas}/C_{theo} was plotted versus P_1 in Excel (see Figure 4.4). Then S_{eff} and Q_B were fitted until C_{meas}/C_{theo} reached around 1 for each inlet pressure of the capillary. Realistic values were obtained for S_{eff} $(26.9\,\mathrm{L\,s^{-1}})$ and Q_B $(1.81 \times 10^{-5}\,\mathrm{mbar\,L\,s^{-1}})$.

Later in this work it was found that the nonlinearity of the quadrupole mass spectrometer QMA200 is the same for each monitored mass and that the measured composition of the gas is independent of the pressure in the measurement chamber (at least for pressures well above the background pressure). In order to increase the amount of the gas in the measurement chamber originating from the capillary with respect to the background gas, the capillary was shortened to a length of 1.68 m (which is the minimum distance between the separation line and the port of the measurement chamber of the QMA200). This increased the conductance to:

$$C_{theo} \approx C_{visc} + C_{mol} = 1.01 \times 10^{-13} \cdot P_1 + 1.24 \times 10^{-11} \qquad [\mathrm{m^3\,s^{-1}}]. \tag{4.13}$$

Again, P_{QMS} was measured for different P_1, and C_{meas}/C_{theo} was plotted versus P_1 in Excel (see Figure 4.4). Fitting S_{eff} for the shorter capillary yielded again a value of $26.9\,\mathrm{L\,s^{-1}}$. The fitted Q_B of $4.41 \times 10^{-5}\,\mathrm{mbar\,L\,s^{-1}}$ is higher than before, as the high vacuum part of the setup has not been baked out since the earlier measurement and the background pressure has been rising slowly. These results indicate that the used approach is suited to determine S_{eff} and Q_B. In Figure 4.4 C_{meas}/C_{theo} is plotted versus the inlet pressure P_1 for the 1.68 m- and the 4 m-capillary, with and without background correction. At lower pressures P_{QMS}, Q_B accounts for a larger part of the throughput of the measurement chamber and increasingly distorts C_{meas} if not corrected. Figure 4.5 shows the fitted throughput Q_C for the 1.68 m-capillary for different inlet pressures. Additionally, it displays the pressure in the measurement chamber P_{QMS} and the expected pressure $P_{expected}$ in the chamber for an absence of the underground gas flow. $P_{expected}$ is calculated after Equation 4.12:

$$P_{expected} = \frac{Q_C}{S_{eff}}. \tag{4.14}$$

$P_{expected}$ is the minimum pressure which can be reached in the current setup for zero underground and long pumping times (when inflow and outflow are in equilibrium). P_{QMS} measured in the experiment is higher due to the presence of underground gases in the chamber. The measurements of P_{QMS} were performed with increasing and decreasing inlet pressures. As the spread in the data is negligible, the pumping times were sufficient, and in- and outflow seem to have approximately reached equilibrium.
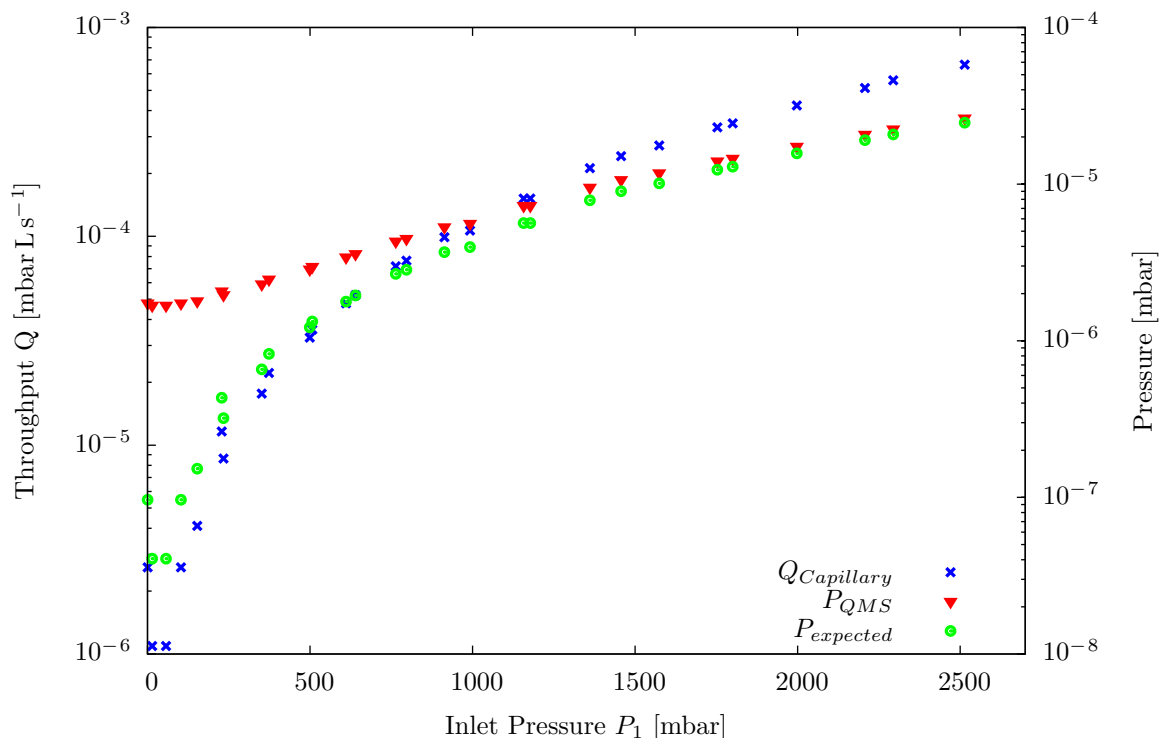
Figure 4.5: For different pressures P_1 at the inlet of the 1.68 m-capillary, the throughput $Q_{Capillary}$, the pressure P_{QMS} in the measurement chamber, and the expected pressure $P_{expected}$ in the chamber for an absence of the gas background are shown.

4.2 Tests of the Setup

4.2.1 Operation Procedure of the Argon Separation

This section is divided in three parts. First, a short overview of the different steps during the separation is given. Then the time consumed in each step is listed in Table 4.1. In the last part, every step is described in detail. A schematic of the setup is shown in Figure 4.1.

Overview of the Procedure

Initially, the entire setup is evacuated and all kinds of adsorbents are operational (i.e. have been regenerated prior to the separation). The separation follows the steps below:

- **Cooling of the columns:** The large dewar is partly filled with liquid nitrogen (LN) and lifted to the upper position, cooling the columns. The temperature controller is switched on, keeping the target temperature by slightly heating the columns once it is reached. The cryogenic water trap and the activated charcoal trap (ACT) are cooled with LN.

- **Loading of the columns:** When the target temperature of the columns is reached, the

sample air is frozen over to the required number of columns. When the pressure of the sample gas is falling only slowly, the separation can be started.

- **Separation:** The carrier gas helium coming from valve 5 runs through the columns via valves 7 and 9 to the ACT. Then via valve 12, it is pumped with the membrane pumps to the air outlet. After some minutes of flushing the pumps with helium, the carrier gas is recycled by connecting the outlet of the pumps via valve 6 with the inlet of the columns. On average, argon is adsorbed on the zeolite for a shorter period of time than nitrogen and oxygen. Hence it leaves the columns first and is trapped on the ACT. The composition of the gas leaving the columns is monitored with a quadrupole mass spectrometer, which is connected to the outlet of the columns via a capillary. Once the argon peak completely left the columns, the valves of the ACT are closed and one can start to regenerate the columns.

- **Regeneration of the columns:** The large dewar thermally isolating the columns is moved in the lower position. The columns are heated to 200–235 °C and pumped with the membrane pumps. When the end temperature is reached, the columns are flushed with helium for around 5 min, while still monitoring the composition of the gas leaving the columns. Then the columns are pumped with the piston pump in place of the membrane pumps for 1 h, as it reaches a better vacuum.

- **Helium pumping:** Still at LN temperature, helium is pumped out of the ACT for 1 h using the piston pump. After the regeneration of the columns, the system is well evacuated and the risk of the ACT drawing in any contamination is unlikely.

- **Release of the argon:** At closed valves, the ACT is heated to 100 °C in order to release the argon from the activated charcoal. The pressure in the ACT is monitored and the amount of argon calculated by using the factor f_{VSTP}, which is determined in Section 4.2.2. The argon is expanded to the capillary and the composition is measured with the quadrupole. During the argon release, the cryogenic water trap can be freed of water, the next air sample cylinder can be installed, and that part can already be evacuated for the next separation.

- **Freezing over of the argon:** The ACT is connected to the cryogenic trap, which is cooled with LN and serves as storage container for the argon.

- **Exchange of the cryogenic trap:** Once the argon is totally frozen over to the cryogenic trap, the valves of the trap are closed and it is replaced by a new trap. The new trap is regenerated at 100 °C, flushed repeatedly with helium, and pumped with the piston pump for around 1 h.

- **Regeneration of the ACT:** The ACT is kept on (or brought again to) 100 °C, then flushed for 5 min with helium, and pumped for 1 h with the piston pump.

Steps of the Separation in Detail The procedure for argon separation from sampled gas is composed of the following steps:

Step	Time Required
Cooling of the columns	40 min
Loading of the columns	10–20 min
Separation	25–40 min
Regeneration of the columns	90 min
Helium pumping	60 min
Release of the argon	50–90 min
Freezing over of the argon	30 min
Exchange of the cryogenic trap	70 min
Regeneration of the ACT	80 min
Total Time	7.6–8.7 h

Table 4.1: The time consumed during each step of the separation.

- Initially all valves except for the valves 7, 13 and 14 are closed. The zeolite columns, the activated charcoal trap (ACT), and the cryogenic trap, which also contains activated charcoal, were regenerated after the last separation and are operational.

- Liquid nitrogen (LN) is filled into the large dewar until the optimal filling level of 28 cm is reached[1]. The dewar is lifted to the top position, isolating thermally the columns from the laboratory. Then the fan inside the dewar is switched on to keep the nitrogen atmosphere well mixed to reach a preferably homogeneous temperature around the columns. The temperature of the columns is observed with the topmost sensor (3). Once the temperature falls below $0\,°C$, the temperature controller (ENDA EUC442) can be turned on. Above that temperature, comparing positive temperatures to the negative target temperature causes problems.

- The time during the cooling down can be used to search for leaks. The whole system was evacuated at the end of the last operation and after the connection of the sample cylinder. The pressure gauges P1, P2, P3, and P4 should display pressures of less than 5 mbar. Valve 2 is opened to check the pressure between the valves 1 and 4, and then closed again. Should any gauge indicate more than 5 mbar, the piston pump is connected to the system in place of the membrane pumps (as it reachs a better vacuum). The respective part is evacuated, isolated by valves, and the pressure is monitored. Without significant pressure increase one can continue and replace the piston pump again with the membrane pumps.

- Still during the cooling down, the dewar of the activated charcoal trap (ACT) is filled with LN, cooling it to $-196°C$. At the end of the cooling down of the columns, the dewar of the cryogenic water trap is also filled with LN. Not containing any adsorbent, the cryogenic

---

[1] At a liquid nitrogen (LN) level of 28 cm the columns are tipping into the LN for a maximum time, causing to cool the columns faster than just by the cold nitrogen atmosphere inside the dewar. At higher levels, the columns are still tipping into the LN when the end temperature is reached. The bottom parts of the columns are then cooled stronger than the top parts and the LN has to be partly evaporated by heating the columns. This is time consuming and a waste of LN. When filling the dewar to a LN level of only 25 cm, the cooling to $-130°C$ already takes around 45 min instead of 30 min for a LN level of 28 cm.

water trap takes less time to cool down and LN losses can be reduced by filling the dewar shortly before the start of the loading of the columns.

- When the target temperature of the columns is reached, the inlet valves of the required number of columns are opened. Then valve 1 is opened, and needle valve 4 is slowly opened. During the loading of the columns, the pressure before the columns (P1) should not exceed 600 mbar. At higher pressures, the different gas species do not have enough time to reach their respective adsorption places on the zeolite. Additionally, the sample gas advances further in the column, leaving less space for separation and causing broader peaks.

- Once P1 is visibly falling, valve 2 can be opened to monitor the pressure at a higher resolution using gauge P3. In the end, valve 4 can be closed shortly to check the pressure in the sample container.

- During the loading of the columns, the outlet of the membrane pumps is connected via valve 6 with the air outlet and the pumps are turned on to evacuate the pumping line.

- When P3 falls with less than $0.1\,\mathrm{mbar\,s^{-1}}$ (usually after 10 min), the valves 1,2, and 4 are closed. The outlets of the used columns and valve 9 are opened. Then the carrier gas helium is introduced into the columns via needle valve 5, which is also used to adjust the operation pressure P1. Shortly afterwards, after a pressure of around 1.5 bar built up in the ACT, contamination with ambient air from the pumping line is unlikely due to the overpressure, and the outlet of the ACT can be connected via valve 12 with the inlet of the pumps.

- After around 3 min, the volume of the pumps should be entirely flushed with helium and the recycling of the carrier gas can be started. Needle valve 5 is closed and immediately afterwards, the outlet of the membrane pumps is connected via valve 6 with the inlet of the columns. Then, some helium is fed into the system using needle valve 5 until the operation pressure P1 is reached again.

- The composition of the gas leaving the columns is monitored using the quadrupole mass spectrometer QMA200. The argon peak leaves the columns first, followed by the oxygen peak soon afterwards. At the end of the argon peak, in order to increase the signal of the gas leaving the columns with respect to the gas underground in the measurement chamber, valve 9 can be closed shortly. This causes pressure to build up, which increases the flow through the capillary to the measurement chamber. Once the whole argon peak left the columns and is trapped on the ACT, valves 9 and 12 are closed. Optionally, the distance of the oxygen from the argon peak can be determined by opening valve 8 partly, adjusting the pressures P1 and P2 to the operating conditions again. The flow resistance of the partly opened valve 8 takes over the resistance formerly caused by the ACT and the flow rate should be around the same as before.

- After the argon peak (or after the appearance of the oxygen peak) valve 8 is moved to (or left in) a partly open position to monitor more precisely the gases leaving the columns during the baking out. The outlet of the membrane pumps is connected via valve 6 with the air outlet. The large dewar isolating the columns is moved to the lower position and

the fan is switched off. Then the columns are heated to around 200–235 °C. When the end temperature is reached, valve 8 is fully opened and helium is fed into the system via needle valve 5, adjusting the pressure at gauge P1 to around 2 bar. The desorbing gases are flushed out of the columns and the gas composition is monitored. Usually flushing with helium for 5 min is sufficient. Some groundwater samples contained massive amounts of CO_2, requiring up to 10 min flushing. Then valve 8 is closed, causing to flood the columns with helium, and needle valve 5 is closed. The piston pump is connected to the system and switched on. Shortly afterwards, valve 8 is opened slowly, connecting the columns with the piston pump. The helium in the columns avoids infiltrating of ambient air from the pumping line. After around 2 min, valve 3 is also opened, enabling to pump the columns from both sides. Now, temperature and pumping are maintained for 1 h. Lesser pumping times proved to be insufficient, decreasing the adsorption capacity of the columns for the following separation.

- After one hour of pumping, the inlet and outlet valves of the columns, as well as valves 3 and 8 are closed. The heating of the columns is switched off. Then the outlet of the ACT is connected via valve 12 with the inlet of the piston pump and the helium still contained in the ACT is pumped out for 1 h. Since the pumping lines should be well evacuated after the regeneration of the zeolite columns and the helium from the ACT flushes additionally lines and pump, no contamination is expected to be drawn to the ACT (which is still cooled by LN). At $-196°C$, argon is strongly attracted to the activated charcoal and should still occupy adsorption places near the entrance of the ACT. As pumping takes places at the exit of the ACT, no argon should be lost.

- During the pumping of the helium, the old sample cylinder can be disconnected and the water in the cryogenic water trap can be removed using a hot air drier. By connecting the outlet of the membrane pumps via valves 4 and 6 with the water trap and by switching those pumps on, the water vapor can be flushed out. After the drying, the membrane pumps are switched off and valve 6 is closed again. Then the new sample cylinder can be connected.

- After the pumping of the helium, valve 12 is closed and the piston pump is connected via valve 3 to the inlet part of the setup. Valve 2 is opened and that entire part is evacuated for the next separation. The dewar containing LN is removed from the ACT and replaced by a dewar filled with water. The cryogenic trap is already immersed into a dewar containing LN to prepare the later argon transfer from the ACT to the cryogenic trap. In order to release the argon, the ACT is heated to around 100 °C using an immersion heater and the pressure of gauge P4 is recorded. Once P4 is not rising any higher, the factor f_{VSTP} determined in Section 4.2.2 can be used to calculate the amount n_{ACT} of argon contained in the trap. n_{ACT} is just the maximum pressure reached in the ACT multiplied by f_{VSTP} and multiplied by the purity of the separated argon. The latter is measured by closing valve 7 and opening valve 9, expanding the argon to the entrance of the capillary, which is the connection to the quadrupole mass spectrometer.

- Once the composition of the separated argon is determined, valve 11 is opened and the argon is frozen over to the cryogenic trap. The trap possesses a valve on its own (not shown on Figure 4.1) and serves as transport and storage container for later ATTA measurements.

When gauge P4 displays zero pressure, valve 11 is closed and additionally 5 min are waited for a possibly pressure increase. If none occurs, one can continue. Otherwise, valve 11 is opened again and the freezing over is continued.

- After the freezing over, valves 2, 3, 4, 11, and the valve of the cryogenic trap are closed. The cryogenic trap is disconnected from the setup and a new one is installed. The new trap is immersed into a dewar filled with water, which is heated to around 100 °C. Valves 8, 9, 11, and the valve of the new trap are opened to pump the gases desorbing from the activated charcoal of the new cryogenic trap. After the largest part of the gases in the trap have been pumped out (as indicated by the piston pump switching to a lower pump frequency), the trap is flushed with helium (valve 9 is closed, valve 10 is shortly opened to flood the trap with helium, then valve 9 is opened again). This is repeated 5 times. Then the trap is pumped for 20 min, flushed again 5 times with helium, and pumped for another 20 min. At the end, the valve of the cryogenic trap and valve 11 are closed.

- If not still at 100 °C, the ACT is heated until that temperature is reached. Then valve 9 is closed and the outlet of the ACT is connected via valve 12 with the inlet of the piston pump. The ACT is flushed for 5 min with helium, at a pressure of 50–100 mbar at gauge P4. After the flushing, valve 9 is opened and the ACT is pumped for 1 h. Then valves 8, 9 and 12 are closed, and the piston pump is switched off. The setup is again operational for another separation.

4.2.2 Determination of the Amount of Argon in the Activated Carbon Trap

This section is about linking the pressure P_{ACT} in the activated carbon trap (ACT) with the amount n_{ACT} of argon in the ACT (in mol), i.e. determining the factor f:

$$f = \frac{n_{ACT}}{P_{ACT}}, \tag{4.15}$$

with P_{ACT} being in equilibrium with the amount of argon adsorbed on the activated carbon at 100 °C (this temperature is applied during the argon release from the ACT). With the characteristic f of the ACT known, n_{ACT} can be easily determined after each gas separation by multiplying the equilibrium pressure P_{ACT} reached in the ACT during the argon release with f. In the experiment for the measurement of f, the ACT was also brought to 100 °C in order to provide for exactly the same conditions. Repeatedly, the ACT was totally pumped out and then connected to a known volume V containing pure argon. Then, n_{ACT} can be determined by looking at the amount $n_{V,1}$ in the volume before the connection and the amount $n_{V,2}$ after the connection:

$$n_{ACT} = n_{V,1} - n_{V,2} = (P_{V,1} - P_{V,2}) \cdot \frac{V}{RT_V}, \tag{4.16}$$

with the pressures $P_{V,1}$ and $P_{V,2}$ in the known volume V before and after the connection, the temperature T_V of V (in Kelvin), and the ideal gas constant R. n_{ACT} is composed of the unbound argon ($P_{ACT} \cdot V_{ACT}$) in the pore space V_{ACT} of the ACT and the amount n_{ad} of argon adsorbed in equilibrium on the activated carbon. In the Henry regime of low pressures, there is a linear

relation between n_{ad} and the pressure P_{ACT} in the ACT, with the Henry-coefficient K:

$$n_{ACT} = P_{ACT} \cdot \frac{V_{ACT}}{RT_{ACT}} + n_{ad} = P_{ACT} \cdot \frac{V_{ACT}}{RT_{ACT}} + P_{ACT} \cdot K \,. \tag{4.17}$$

As n_{ACT} is linearly proportional to P_{ACT}, f is a constant and should have the same value for every amount n_{ACT} of argon let in the ACT during the experiment:

$$f = \frac{n_{ACT}}{P_{ACT}} = \frac{V_{ACT}}{RT_{ACT}} + K \,. \tag{4.18}$$

Volume at standard pressure (P_{St}=1013.25 mbar) and standard temperature (T_{St}=273.15 K) per pressure are more useful dimensions for f. Equation 4.16 then reads:

$$f_{VSTP} = \frac{n_{ACT}}{P_{ACT}} \cdot \frac{RT_{St}}{P_{St}} = (P_{V,1} - P_{V,2}) \cdot \frac{T_{St}V}{T_V P_{St} P_{ACT}} \,. \tag{4.19}$$

The results of this experiment are summarized in Table 4.2. All errors are calculated using the Gaussian error propagation. Beside argon, also data for air and helium were taken. Argon and air have a higher f_{VSTP} than helium, meaning that, at the same pressure, the amount adsorbed on the ACT is higher for argon and air than for helium. For argon, f_{VSTP} is nearly the same for every n_{ACT}, confirming the linear relation between n_{ACT} and P_{ACT}. For higher P_{ACT}, f_{VSTP} is only slightly smaller than for lower P_{ACT}. Henry´s Law still seems to hold for the examined pressure range. In the experiments marked with Ar*, a known amount n_{ACT} of argon was frozen over to the ACT at liquid nitrogen temperature. Then the ACT was heated to 100 °C and P_{ACT} was recorded. This procedure is closer to the experiment, but is more time consuming. For these three experiments f_{VSTP} is only slightly higher than for the others. Apparently, adsorption equilibrium was not fully reached for the other experiments, but the difference is negligible. As during most separations between 500 ccSTP and 700 ccSTP argon are processed, 0.6 ccSTP/mbar is a good value to use for f_{VSTP}.

4.2.3   Determination of the Argon Recovery

Beside the purity of the separated argon, the argon recovery R is one of most important characteristics of the setup for argon separation. It is defined as the ratio of the amount n_p of purified argon at the end of the separation and the amount n_s of argon in the sample container before the separation:

$$R = \frac{n_p}{n_s} \,. \tag{4.20}$$

Losses of argon may occur when the gas is frozen over from the sample container to the zeolite columns and a residual pressure remains. During the separation, not all argon may be leaving the columns with the main peak. When pumping the helium from the activated carbon trap (ACT) at -196°C, some argon might be lost as well. All this is contained in R. The subsequent argon transfer from the ACT to the storage container is considered next to complete. The container is sufficiently filled with activated carbon to allow no significant residual pressure at -196°C during the transfer, while the ACT is heated to 100 °C and desorbs all argon.

Element	P_{ACT} [mbar]	n_{ACT} [ccSTP]	f_{VSTP} [ccSTP/mbar]
Ar	2638.0	1554.8	0.589 ± 0.01
Ar	2384.7	1377.1	0.577 ± 0.01
Ar*	1800	1054.0	0.586 ± 0.01
Ar	1381.3	815.5	0.590 ± 0.01
Ar	1284.7	758.4	0.590 ± 0.01
Ar*	1280	775.8	0.606 ± 0.01
Ar	1195.2	707.0	0.592 ± 0.01
Ar*	1155	696.6	0.603 ± 0.01
Ar	1111.1	662.3	0.596 ± 0.01
Ar	1033.3	614.3	0.595 ± 0.01
Ar	960.3	574.6	0.598 ± 0.02
Ar	893.2	533.2	0.597 ± 0.02
Ar	830.6	497.6	0.599 ± 0.02
Ar	772.2	463.6	0.600 ± 0.02
Ar	717.9	431.3	0.601 ± 0.02
Ar	667.0	403.2	0.604 ± 0.02
Ar	619.8	372.6	0.601 ± 0.02
Air	925.9	580.4	0.627 ± 0.02
He	1941.6	423.1	0.218 ± 0.007
He	1885.7	411.5	0.218 ± 0.008
He	1831.8	397.4	0.217 ± 0.008
He	1779.7	387.5	0.218 ± 0.008
He	1600.1	347.7	0.217 ± 0.009
He	1554.2	338.6	0.218 ± 0.009
He	1038.4	226.0	0.218 ± 0.014
He	1008.6	219.4	0.218 ± 0.014
He	979.7	212.8	0.217 ± 0.015
He	792.5	172.2	0.217 ± 0.018
He	769.9	175.5	0.228 ± 0.018
He	575.6	125.0	0.217 ± 0.025
He	559.2	121.7	0.218 ± 0.025
He	395.5	85.3	0.216 ± 0.036
He	384.3	82.8	0.215 ± 0.037
He	202.5	43.9	0.217 ± 0.070
He	196.7	43.1	0.219 ± 0.072
He	96.4	20.7	0.215 ± 0.147
He	93.6	20.7	0.221 ± 0.152
He	68.5	14.9	0.218 ± 0.207
He	66.5	14.9	0.224 ± 0.213
He	44.7	9.9	0.222 ± 0.317
He	43.5	9.1	0.209 ± 0.326
He	27.1	5.8	0.214 ± 0.523

Table 4.2: The results of the experiment conducted to determine f_{VSTP}, which is the amount of the gas (n_{ACT}) in the activated carbon trap (ACT) per pressure in the ACT (P_{ACT}). The first column lists the gas used in the experiment. Values for the Ar* were determined in experiments closer to the separation procedure (see text).

n_s [ccSTP]	p_{Ar} [%]	R_f [%]	R_V [%]
536	90.7	95.4 ± 3.0	95.9 ± 2.8
536	96.7	92.5 ± 3.0	94.7 ± 2.9
422	97.75	94.5 ± 3.5	99.6 ± 3.5
424	96.6	94.9 ± 3.5	96.5 ± 3.5
544	98	96.2 ± 3.0	99.4 ± 2.9
537	99.2	99.2 ± 3.1	96.8 ± 2.9

Table 4.3: The argon recovery R_f determined via the factor f_{VSTP}(see Section 4.2.2) and the recovery R_V determined via volume expansion for several separations. The total amount n_s of argon in the sample container before the separation and the purity p_{Ar} of the separated argon are also given.

Some separations were performed with laboratory air in order to determine R. The amount n_s of argon in the sample container before the separation is the percentage R_{Ar} of argon in the atmospheric air times the volume V_s and the pressure P_s of the sample container:

$$n_s = R_{Ar} \cdot V_s \cdot (P_s - P_{Water}) \cdot \frac{T_{St}}{T_s \cdot P_{St}} \, . \tag{4.21}$$

P_{Water} is the saturation pressure of water, which depends on the temperature during the sampling. Even for low relative humidities the saturation pressure is reached inside the container due to the compression. Any additional water vapor condenses. For sampling temperatures between 0 and 30 °C, P_{Water} ranges from 6 to 42 mbar [Buck, 1981]. The second fraction normalizes n_s to ccSTP, with the temperature of the sample T_s in Kelvin, the standard pressure P_{St}=1013.25 mbar, and the standard temperature T_{St}=273.15 K.
The amount n_p of purified argon at the end of the separation was determined in two ways. One way is to apply the factor f_{VSTP}, which was determined in Section 4.2.2. f_{VSTP} multiplied with the maximum pressure P_{ACT} reached in the ACT during the argon release and multiplied with the purity p_{Ar} of the separated argon yields n_p in ccSTP:

$$n_p = f_{VSTP} \cdot P_{ACT} \cdot p_{Ar} \, . \tag{4.22}$$

The second way of determining n_p is the expansion of the separated argon in a known volume V during the argon release from the ACT:

$$n_p = P \cdot p_{Ar} \cdot \left(V \cdot \frac{T_{St}}{T_V \cdot P_{St}} + f_{VSTP} \right) , \tag{4.23}$$

with the maximum pressure P reached in V and the temperature T_V of V. The second term in the brackets takes care of the argon still in the ACT at pressure P. As the first term in the brackets is around 14 times larger than f_{VSTP}, this method can still be considered independent from the first. Table 4.3 lists the argon recovery R_f determined via the factor f_{VSTP} and the recovery R_V determined via volume expansion for several separations. For all but one experiment R_f is slightly lower than R_V. The reason for this systematic deviation is unclear. However, the difference is small and the argon recovery is at a satisfying level.
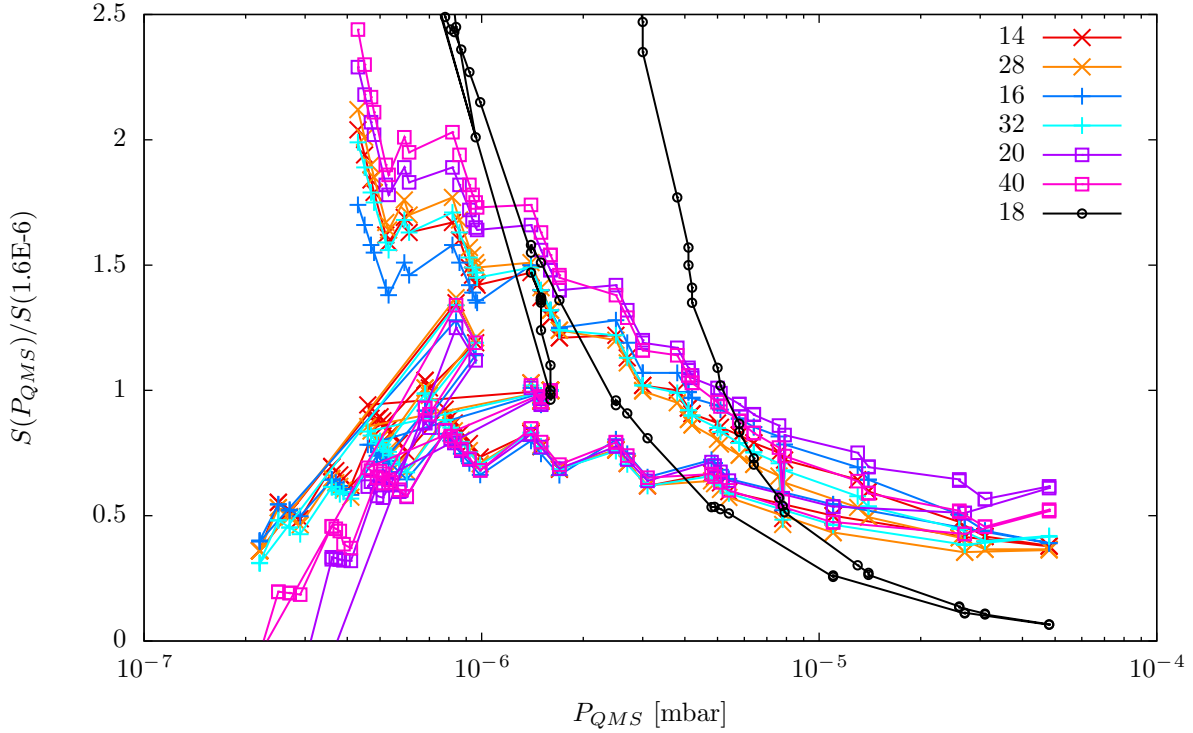
Figure 4.6: The sensitivities normalized to the corresponding sensitivity at 1.6×10^{-6} mbar for the respective masses. The pressure P_{QMS} in the measurement chamber was increased from 4.3×10^{-7} mbar to 4.8×10^{-5} mbar ("upper branch"), then decreased to 2.2×10^{-7} mbar ("lower branch"), then sharply increased to 8.4×10^{-7} mbar, then again decreased to 4.6×10^{-7} mbar. After that, it was once again sharply increased to 1.6×10^{-6} mbar. The spread is higher for the upper than for the lower branch. The steps arise from adjusting P_{QMS} by increasing or decreasing the pressure at the inlet of the capillary in increments.

4.2.4 Nonlinearity of the Quadrupole Mass Spectrometer

Wonneberger [2008] varied the pressure P_{QMS} in the measurement chamber and found that the signal of the employed quadrupole mass spectrometer (QMA200 from Pfeiffer Vacuum, Asslar, Germany) increases linearly with P_{QMS} only up to a pressure of 5×10^{-7} mbar and flattens at higher pressures. This nonlinearity was investigated in this thesis by measuring the ion currents of the relevant masses 14, 16, 18, 20, 28, 32, 40 as function of P_{QMS}. P_{QMS} was adjusted by varying the pressure of ambient air at the entrance of the capillary from 0 to 2250 mbar, thus keeping the gas composition at the entrance constant. In order to take care of possible hysteresis effects, starting from 0 mbar, measurements with increasing pressure were conducted up to the maximum pressure. Then measurements with decreasing pressure were performed. The sensitivity S_i of mass i can be defined as ion current I_i of that mass per total pressure P_{QMS} in the measurement chamber:

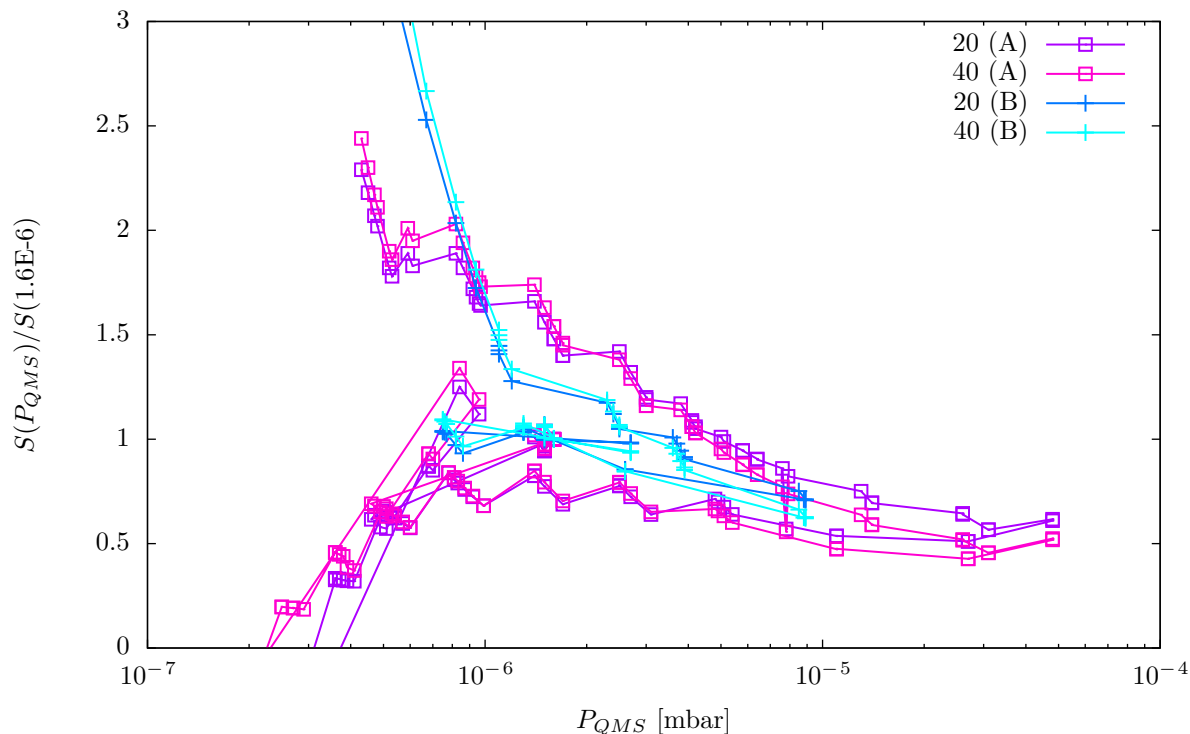$$S_i = \frac{I_i}{P_{QMS}}. \tag{4.24}$$

Figure 4.7: The sensitivities normalized to the corresponding sensitivity at 1.6×10^{-6} mbar for the respective masses. Squares denote the results of the experiment A with 2–4 min pressure adjustment time, triangles those from experiment B with 20–40 min adjustment time. The steps arise from adjusting P_{QMS} by increasing or decreasing the pressure at the inlet of the capillary in increments.

As the later aim is to derive gas concentrations from measured ion currents at various pressures, the sensitivity should behave in the same way for all measured masses at all pressures. A linear relation between sensitivity and pressure is not required, but any possible change in sensitivity with pressure should occur with the same factor for all masses. That means S_i normalized to the sensitivity of a certain fixed pressure P_{fix}, i. e. $S_i(P_{QMS})/S_i(P_{fix}) = \tilde{S}_i(P_{QMS})$, should match for all masses. Any spread in the normalized sensitivities would cause the concentrations derived from the measured ion currents to change with pressure (although the gas composition at the entrance of the capillary remains the same). Figure 4.6 shows $\tilde{S}_i(P_{QMS})$ as function of P_{QMS}. The upper branch contains the measurements performed at increasing pressures, the lower branch those at decreasing pressures. Water (mass 18), clearly deviates from the other masses. Constituting the biggest part of the gas background in the measurement chamber, during the experiment, it is increasingly replaced and flushed out by the ambient air entering the chamber through the capillary. During the argon separation, no water peak leaving the columns was found. Hence, including water in the concentration determination is as unnecessary as impossible. The splitting in two branches is not critical, the spread in the normalized sensitivities in each branch however is (this causes the concentrations derived from the ion currents to change with pressure). For the upper branch (measurements at increasing pressures), the spread is larger than for the lower branch. Overall, the spread is smaller at higher pressures than at lower ones.

The experiment was repeated after 4 days (experiment "B") and the results for the masses 20 and 40 are plotted in Figure 4.7 together with the results of the first experiment ("A"). Again, there is a split in two branches, with a higher spread for lower pressures and for the upper branch. During experiment A (squares), the pressure was changed every 2–4 min, while during B, it was changed every 20–40 min. The different pressure adjustment times seem to have effects on the shape and slope of the branches. How they affect the spread and thus the derived concentrations is discussed in the next section. The reason for the asymmetric behavior of $\tilde{S}_i(P_{QMS})$ regarding increasing or decreasing pressure remains unclear. In either case, the increase of the signal of the QMA200 with P_{QMS} is nonlinear, which confirms the observation of Wonneberger [2008]. The nonlinearity differing for the single masses causes a spread in the normalized sensitivities. The consequence of this spread is that any calibration will only be valid for a certain pressure range.

4.2.5   Calibration of the Quadrupole Mass Spectrometer

As the detection efficiency of the quadrupole mass spectrometer QMA200 is not the same for each mass and the ratio of single-ionized and double-ionized particles per molecule is also unknown, a calibration of the QMA200 is required in order to obtain concentrations from the measured ion currents. The built-in measurement method MCD (Multiple Concentration Detection) converts the measured ion currents into concentrations using a solution matrix, where the calibration factors are stored. To determine these factors, a gas of known concentration is required. The known concentration is entered in the calibration program, the gas is let into the measurement chamber, and the calibration program is started. The calibration factors are then calculated by the program and MCD is ready for use afterwards. In this work, MCD is mainly used to determine the composition of the separated argon. Beside argon, trace amounts of carbon dioxide, helium, nitrogen, and oxygen may be present. Since ambient air contains too little helium for the calibration, a gas mixture of ambient air and helium has to prepared.

Limits of the Calibration

Measuring the composition of the separated argon is possible with the current setup, however, within certain restrictions. As the possible impurities contain reactive gases as oxygen, the only option is to measure dynamically (having the sample gas flowing continually through a capillary into the measurement chamber while pumping the chamber[1]). For dynamic measurements, the relation of in- and outflow of the chamber is given by Equation 4.12:

$$S_{eff} \cdot P_{QMS} = Q_C(P_1) + Q_B \, ,$$

with the effective suction capacity of the turbo molecular pump at the chamber S_{eff}, the pressure at the chamber P_{QMS}, the flow through the capillary $Q_C \propto P_1^2 + P_1$, the pressure at the entrance of the capillary P_1, and the constant flow Q_B of background gases, which is by approximation independent of the pressure. The contributions to the total pressure in the chamber can also be

---

[1]During static measurements, the sample would be enclosed in the measurement chamber and the reactive gases would be increasingly depleted with time.

expressed in the following way:

$$P_{QMS} = \frac{Q_C(P_1)}{S_{eff}} + \frac{Q_B}{S_{eff}}. \tag{4.25}$$

The possibilities to maximize the first fraction while minimizing the second were nearly exhausted during this work. The background Q_B can be reduced by baking out the measurement chamber, which increases the wear if practiced too often. The chamber was baked out a few times during this thesis. Each time, the background recovered to the old value after few months, making baking out a short term improvement at the expense of equipment lifetime. But as the greatest part of Q_B seems to be diffusing through the turbo molecular pump into the measurement chamber, the reduction of Q_B by baking out is of minor importance. The outlet of the turbo molecular pump is connected via a flexible tubing with the membrane pump, which has atmospheric pressure at its outlet. Hence, the gas in this tubing (and at the outlet of the turbo molecular pump) is a mixture of the gas being pumped out of the measurement chamber and ambient air (which is to a part inevitably diffusing through the membrane pump). This greatly reduces the severeness of Q_B, as Q_B consists to a large part of the gas issuing from the capillary. The effective suction capacity of the turbo molecular pump at the chamber S_{eff} was maximized by directly flanging the chamber atop of the turbo molecular pump, without any additional flow resistances in between, such as valves or tubes. Q_C was increased by reducing the length of the 40 μm inner diameter capillary to 1.68 m, which is the minimum distance between the measurement chamber and the capillary port of the setup for argon separation. The highest pressure P_{QMS} the used quadrupole can tolerate is 1×10^{-4} mbar, which is currently reached at P_1 of around 5000 mbar. By using for example a 70 μm inner diameter capillary with a length of 2.5 m, 1×10^{-4} mbar would be already reached at a P_1 of 2000 mbar. This would increase the share of the gas directly issuing from the capillary to the total gas in the chamber from currently 41.5 % to 80.4 % for a P_1 of 500 mbar, and from currently 90.6 % to 98.3 % for a P_1 of 2000 mbar. But since a good part of the background gas flow Q_B contains gas issuing from the capillary (as explained above), the improvement will not be as big as the figures suggest. However, exchanging the capillary is one of the last options left to optimize the setup.
How Q_B effects the calibration and the later measurements is best seen in a calculation example. Let S be the total share of the gas issuing from the capillary, including contributions of Q_B. Then 1-S is the share of ambient air in the measurement chamber. C_{cal}^{Ar} is the actual argon concentration of the gas used to calibrate MCD. Taking into account that ambient air contains around 1 % argon, the actual argon concentration $C_{chamber}^{Ar}$ (in percent) in the measurement chamber is:

$$C_{chamber}^{Ar} = S \cdot C_{cal}^{Ar} + 0.01 \cdot (1 - S). \tag{4.26}$$

As for the different gases i the concentrations C_{cal}^i and not (the unknown) concentrations $C_{chamber}^i$ have to be used by MCD for the calibration, the calibration factors are falsified by a factor f^i:

$$f^i = \frac{C_{cal}^i}{C_{chamber}^i} = \frac{C_{cal}^i}{S_{cal} \cdot C_{cal}^i + 0.01 \cdot (1 - S_{cal})}, \tag{4.27}$$

with the total share S_{cal} during the calibration. When applying the calibration, instead of the actual concentration C_{sample}^{Ar} of the sample at the entrance of the capillary, the concentration

S	0.9	0.95	0.98	0.9	0.95	0.98	0.9	0.95	0.98
C_{cal}^{Ar}	0.005	0.005	0.005	0.01	0.01	0.01	0.5	0.5	0.5
f^{Ar}	0.95	0.95	0.95	1.00	1.00	1.00	1.05	1.05	1.05
C_{sample}^{Ar}	0.98	0.98	0.98	0.98	0.98	0.98	0.98	0.98	0.98
$C_{chamber}^{Ar}$	0.88	0.93	0.96	0.88	0.93	0.96	0.88	0.93	0.96
C_{meas}^{Ar}	0.84	0.89	0.91	0.88	0.93	0.96	0.93	0.98	1.01

Table 4.4: For different shares S of the gas issuing from the capillary of the total gas in the measurement chamber and different argon concentrations C_{cal}^{Ar} of the calibration gas and a sample argon concentration C_{sample}^{Ar} of 98 % at the entrance of the capillary, the following parameters were calculated: the factor f^{Ar}, by which the calibration factor of argon is falsified; the true argon concentration $C_{chamber}^{Ar}$ in the measurement chamber; and the measured argon concentration C_{meas}^{Ar}, when applying the calibration performed with the respective calibration gas.

C_{meas}^{Ar} will be given out by MCD:

$$C_{meas}^{Ar} = f^{Ar} \cdot C_{chamber}^{Ar} = f^{Ar} \cdot (S \cdot C_{sample}^{Ar} + 0.01 \cdot (1 - S)) . \qquad (4.28)$$

Table 4.4 lists the results for the calculations carried out with an assumed S_{cal} of 95 % and a purity of the argon sample C_{sample}^{Ar} of 98 %. The shares were varied around S_{cal} and three different calibration gases were analyzed, having C_{cal}^{Ar} of 0.5, 1, and 50 %. For the first calibration gas, C_{sample}^{Ar} is underestimated due to f^{Ar} and S, for the second, it is underestimated solely due to S, and for the third, C_{sample}^{Ar} is underestimated at lower S and overestimated at high S due to the high f^{Ar}. Judging from these figures, if S is really in the range of 90 %, C_{sample}^{Ar} tends to be underestimated with the determined concentration C_{meas}^{Ar}. Fortunately, this can be excluded. With calibrations, which were performed with a calibration gas having less than 1 % argon, argon concentrations of up to 98 % were measured. This means, the value of S must be close to 100 % and the gas mixture at the outlet of the turbo molecular pump consists nearly only of the gas pumped out of the measurement chamber.

The different calibrations performed in this thesis have been tested by measuring gases of known composition at different pressures P_1 before the capillary, resulting in different pressures P_{QMS} in the measurement chamber. To ensure any possible gas background effects wont be missed (although their occurrence seems unlikely after the calculations above), some of these tests were performed using gases different from ambient air. Other tests, as the one about the sensitivity in Section 4.2.4, were conducted with ambient air, to investigate solely the behavior of the quadrupole mass spectrometer. It is hard to distinguish this behavior from the effect that the turbo molecular pump, as the pump performance differs for the different gases, itself may affect the gas composition in the measurement chamber. Such pump or mass spectrometer effects may influence the measurement, depending on how much time passed between the measurement and the adjustment of the pressure to a specific value, or depending on if the previous measurement was conducted at a lower or higher pressure. To investigate these effects, the pressure P_1 of ambient air before the capillary was increased stepwise from a few mbar to 2250 mbar and then decreased stepwise to a few mbar again, while measuring gas concentration with MCD. Since the gas issuing from the capillary as well as the gas background have atmospheric composition, the measured gas composition should be atmospheric, too. Hence, when normalizing the measured concentrations to the atmospheric ones, the outcome should be unity. The experiment was performed twice. One time with pressure adjustment times between 2 and 4 min (experiment

"A"), and the other time with pressure adjustment times between 20 and 40 min (experiment "B"). Figure 4.8 shows the normalized concentrations as a function of P_{QMS}. As in the last section, the upper branch contains the measurements performed at increasing pressures, while the lower contains those at decreasing pressures. For both experiments, the upper branch is close to unity within 5 %. The deviations from unity are positive for experiment A and negative for B and seem to depend on the pressure adjustment time. Measuring concentrations with decreasing pressures should be avoided due to the large deviations from unity of the lower branch. What one can learn from these experiments is that measurements with the quadrupole should be performed preferably under the same conditions as the calibration. As the calibration can be considered having been performed at increasing pressures, the measurements of the upper branches clearly deviate less from unity than those of the lower branch. Choosing similar pressure adjustment times (if possible) can also help to minimize the deviations.
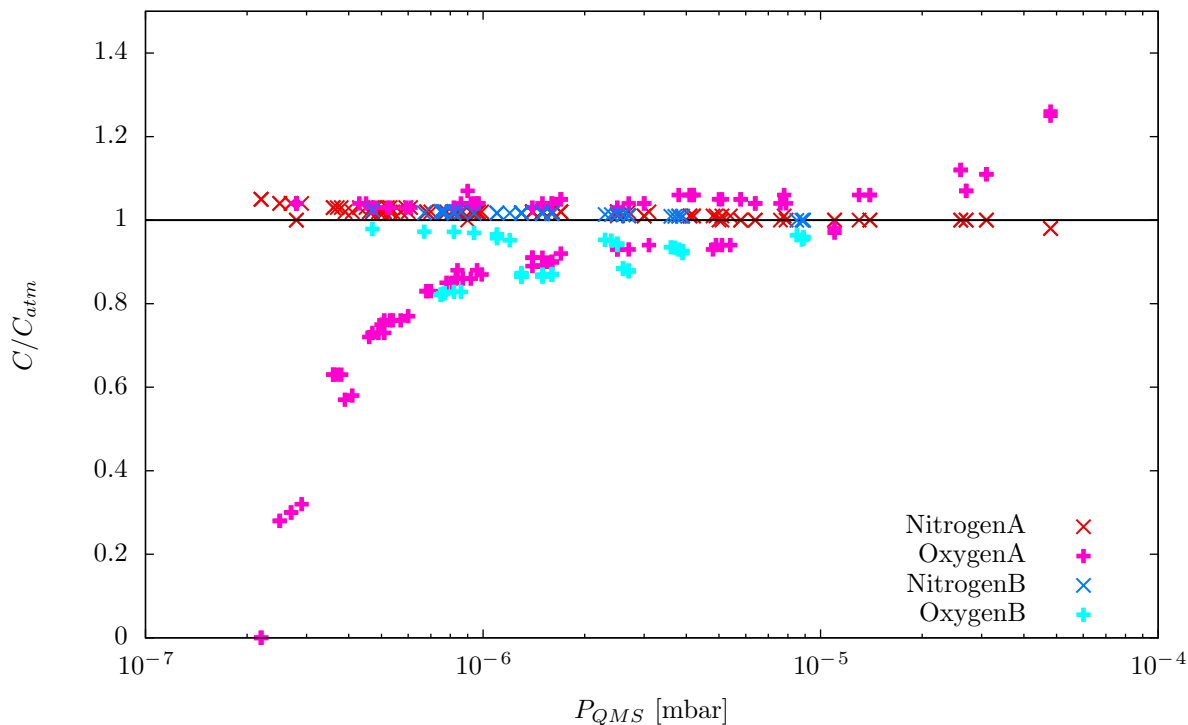
Figure 4.8: Verification of a calibration by measuring ambient air at different pressures. The gas concentrations normalized to the atmospheric values are plotted and should be unity. A denotes the measurements performed with 2–4 min pressure adjustment time, B those performed with 20–40 min pressure adjustment time. The upper branches was measured at increasing and the lower at decreasing pressure.

Latest Calibration

Taking krypton separation into account as a future application of the setup for argon separation, the latest calibration was performed using a calibration gas containing krypton. A container of around 9 L was used, having one port for krypton 4.0, one for helium 5.0, and one for pressurized ambient air. The container was filled with 25.3 mbar krypton, 99.9 mbar helium, and
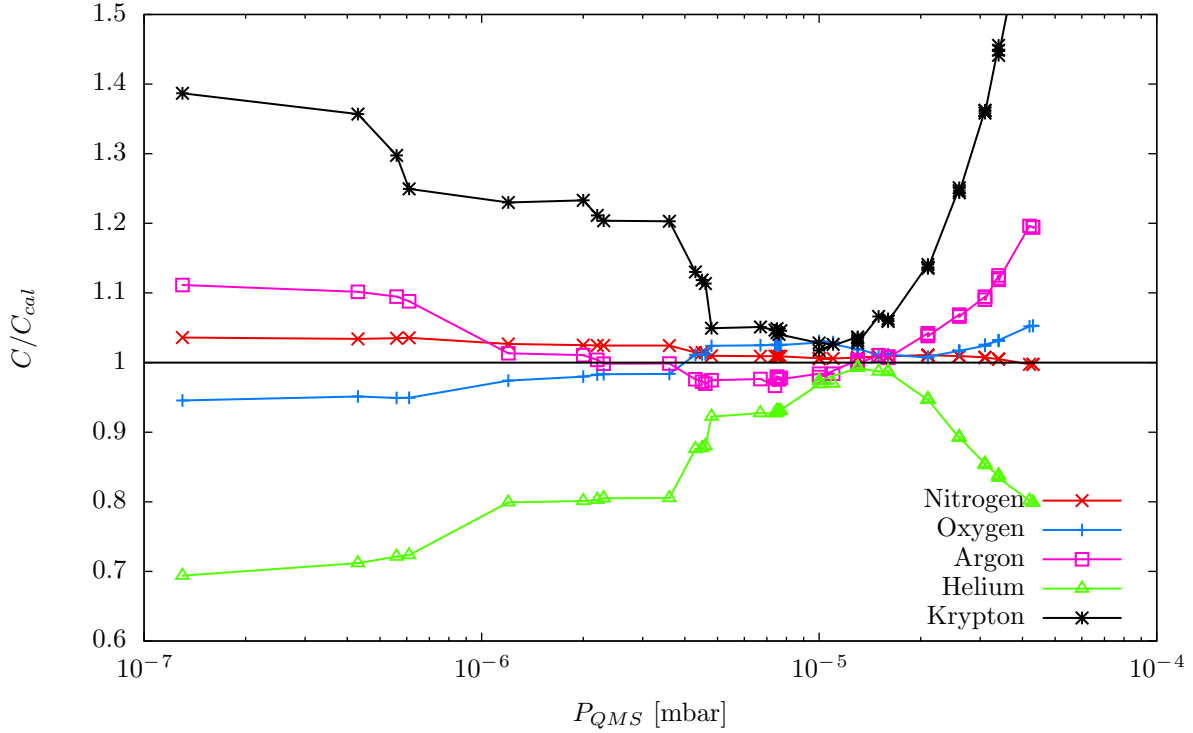
Figure 4.9: Verification of the latest calibration by measuring the calibration gas at different pressures P_{QMS} in the measurement chamber of the quadrupole mass spectrometer. The gas concentrations normalized to the respective concentrations of the calibration gas are plotted and should be unity. The calibration was performed at a pressure P_1 at the entrance of the capillary of around 1300 mbar (corresponding to a P_{QMS} of around 1.4×10^{-5} mbar). It seems to be only applicable for pressures P_1 ranging from 1000 to 1600 mbar, corresponding to pressures P_{QMS} lying between 6×10^{-6} and 2×10^{-5} mbar. This is the pressure range reached during the purity check of the separated argon of typical air samples of 30 to 63.6 LSTP.

2355.5 mbar ambient air, without the risk of any losses, as all gas sources had overpressure with respect to the gas in the container at the respective inlet. A Lex1 pressure gauge (Keller AG für Druckmesstechnik, Winterthur, Switzerland) was used for the pressure measurements (± 1.5 mbar precision). After the corrections for water vapor using the vapor pressure given by Buck [1981], one ends at the concentrations listed in Table 4.5. The calibration was performed at a pressure P_{cal} at the entrance of the capillary of 1293.4 mbar, which corresponds to a P_{QMS} of around 1.4×10^{-5} mbar. It was verified by varying the pressure of the calibration gas at the entrance of the capillary, hence using a gas different from the background of atmospheric air. The verification was conducted a day after the calibration at increasing pressures, to avoid effects of the lower branch described above. The measured concentrations normalized to the respective concentrations of the calibration gas, $\tilde{C}$, are shown in Figure 4.9 and should be unity. For pressures at the entrance of the capillary between 960 and 1600 mbar (which corresponds to a P_{QMS} between 6×10^{-6} and 2×10^{-5} mbar), the deviations from unity of the normalized concentrations $\tilde{C}$ are less than 1 % for nitrogen, less than 3 % for oxygen, less than 4 % for argon, less than 8 % for helium, and less than 14 % for krypton. Hence, inside this pressure

Species	Concentration [%]
Nitrogen	73.4024
Oxygen	19.6864
Helium	4.07
Krypton	1.019
Argon	0.878
Water	0.9085
CO_2	0.0357

Table 4.5: The composition of the gas mixture used for the latest calibration of the measurement method MCD (Multiple Concentration Detection) of the quadrupole mass spectrometer QMA200.

range, the composition of argon separated with the setup can be determined with sufficient precision. Outside the pressure range, the deviations from unity get much higher, especially for helium and krypton. Surprisingly, the behavior of the latter two is contrary to each other, which might be some kind of mass discrimination. No background gas effect, i.e. higher nitrogen and oxygen signals at lower pressures, can be clearly observed. Actually, for the two noble gases enriched with respect to atmospheric values (helium and krypton), one would have expected $\tilde{C}$ below unity for lower pressures, as the background has the highest influence there. This is only observed for helium, reaching even far lower $\tilde{C}$ than expected. The higher the pressure before the capillary becomes, the lower is the contribution of the gas background to the total gas in the measurement chamber. Because of that, at pressures higher than the one at which the calibration was performed (P_{cal}), one would have expected normalized concentrations slightly above unity for krypton and helium. However, $\tilde{C}$ of helium falls far below unity and the one of krypton rises higher than background effects could explain. After the simulation of the background performed in Section 4.1.6, the contribution of the capillary to the total gas in the chamber is around 80 % at P_{cal}. Considering that the background is a mixture of that gas and atmospheric air, the contribution of the capillary is even higher. That means, at higher pressures, there is no way to explain measuring 1.5 times the expected krypton concentration solely with the gas background and pump effects or effects of the QMA200 seem to play the major role. This also agrees well with the conclusions drawn from the calculations at the beginning of this section.

For a pressure P_1 before the capillary between 960 and 1600 mbar, the relative error of the argon concentration measurement is around ± 4 %, which is entirely sufficient for the determination of the purity of the separated argon. Should the actual impurities of the separated argon be 5 % or even 10 % higher than the measured ones, they still can be removed by the getter of the ATTA setup without causing intolerably high costs.

Longterm Stability of the Calibration

Seven weeks after the latest calibration, the longterm stability of the calibration was checked by measuring gas mixtures of known composition at different pressures P_{QMS} in the measurement chamber of the quadrupole mass spectrometer. Mixture A is ambient air with 10 % helium, and mixture B is ambient air with 14 % helium and 60 % argon (see Table 4.6). The measured concentrations normalized to the respective concentrations of the gas mixture are plotted in Figure 4.10. The pattern of the normalized concentrations of mixture A resembles those of
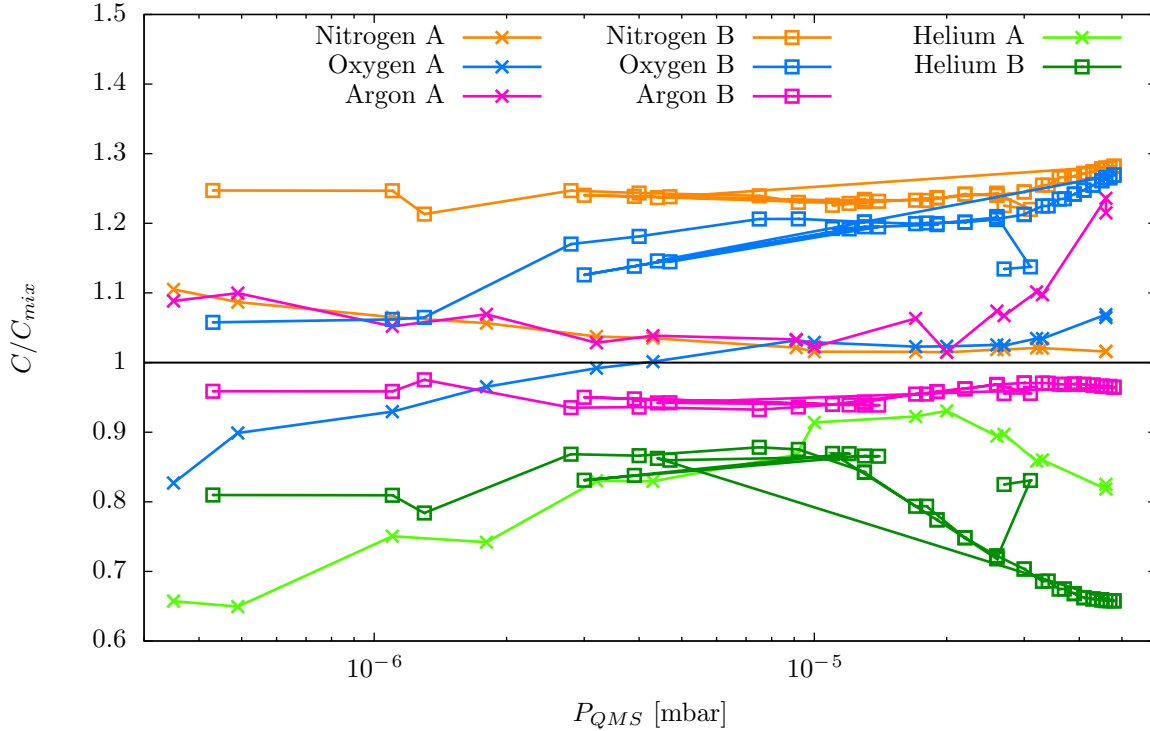
Figure 4.10: Check of the longterm stability of the latest calibration by measuring gas mixtures of known composition (A and B) at different pressures P_{QMS} in the measurement chamber of the quadrupole mass spectrometer seven weeks after the calibration. Mixture A is ambient air with 10 % helium, and mixture B is ambient air with 14 % helium and 60 % argon. The gas concentrations normalized to the respective concentrations of the gas mixture are plotted and should be unity. Judging from the little deviations from unity of the normalized argon concentration of both mixtures, at least for argon longterm stability seems to be granted .

the verification shown in Figure 4.9, which had been performed one day after the calibration. Nitrogen and argon are slightly overestimated, whereas oxygen is slightly and helium is heavily underestimated. Since mixture A is very similar to the gas used both for the calibration and the earlier verification, and around the same normalized concentrations were measured seven weeks after the calibration, longterm stability is granted. For mixture B, the higher deviations of the normalized concentrations from unity seem to be correlated with the composition of mixture B, which is very different from the gas used for the calibration. This time, nitrogen and oxygen both are heavily overestimated, and argon is slightly underestimated. Helium is again heavily underestimated, but slightly less than for mixture A. Fortunately, for both mixtures, argon is never under- or overestimated more than 7 % for pressures P_1 at the entrance of the capillary between 600 and 1800 mbar (which corresponds to a P_{QMS} ranging from around 2×10^{-6} to 3×10^{-5} mbar). For the application of controlling the purity of the separated argon, this is sufficient. By installing cylinders containing a calibration gases having compositions close to the expected composition of the gas which has to be controlled, one can perform calibrations shortly before measuring without great efforts. This would increase the accuracy of the determination of gas compositions.

92

Species	Concentration [%]	
Mixture	A	B
Nitrogen	69.64	19.82
Oxygen	18.68	5.29
Helium	10.02	14.18
Argon	0.833	60.69

Table 4.6: The main components of the gas mixtures used to investigate the longterm stability of the latest calibration of the measurement method MCD (Multiple Concentration Detection) of the quadrupole mass spectrometer QMA200.

4.2.6 Separations with one Column
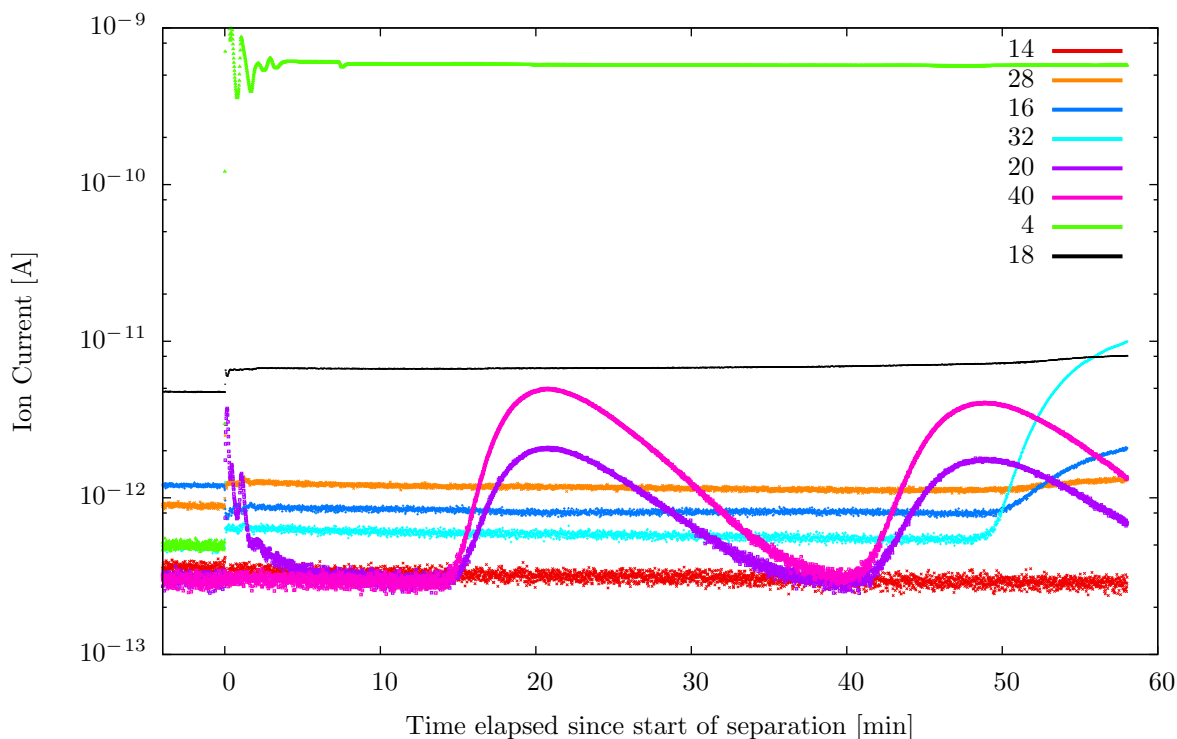
Figure 4.11: A successful separation of argon from air with one column (experiment 110503). The composition of the gas leaving the column was observed with the quadrupole mass spectrometer QMA200. Each curve consists of over 4000 measurements. At the first peak, from higher to lower ion currents, the following masses are represented by the curves: 4 (helium, green), 18 (water, black), 40 (argon, magenta), 20 (argon, purple), 28 (nitrogen, orange), 16 (oxygen, dark blue), 32 (oxygen, light blue), and 14 (nitrogen, red). During that experiment, the argon peak was not trapped in the activated carbon trap and traveled another time through the column, due to the recycling of the carrier gas helium. Only faint peak broadening occurs during the separation, the two argon peaks nearly have the same height and shape. The (first) argon peak is very well separated from the oxygen peak. The high levels of water, nitrogen, and oxygen result from the background gas in the measurement chamber. The rise in the mass 20 signal at the beginning of the experiment seems to be related with the inlet of helium in the measurement chamber and constitutes no real signal at that mass.

As first testing of the setup for argon separation, experiments with a single column were performed. Since each experiment took around 5 h, the testing was not excessive. This section is focused on the effects of the variation of the operation parameters, whereas the separation procedure is described in Section 4.2.1. As an example of a successful separation, the gas composition at the exit of the column monitored with the quadrupole mass spectrometer QMA200 during experiment 110503 is shown in Figure 4.11. At the start (t = 0), the flow of the carrier gas helium is started and adjusted. After some time, the argon peak appears. During the experiment shown, the argon was not trapped in the activated carbon trap (ACT) and consequently travels through the column another time, as it is recycled together with the carrier gas helium.

Around 8 min after the end of the (first) argon peak, the oxygen peak emerges. Had the argon been trapped in the ACT, a complete separation from oxygen would have been achieved. The apparently high levels of nitrogen and oxygen issue from the gas background in the measurement chamber and do not affect the purity of the separated argon. Due to the background gas, no statements about the argon purity can be made at this time of the experiment. However, one should note that even at the maximum of the argon peak, the mass 40 signal is still only around 1 % of the helium signal. With respect to the total signal issuing from the capillary (i.e. per approximation the helium signal), the background is acceptably low. Only because the share of nitrogen, oxygen, and argon of the gas coming from the capillary is so low, the gas background seems so high.

The results of the first tests are compiled in Table 4.7. For the times of the start and the end of a peak, the time when the signal rises from or falls back to the trend line of the background is taken in this work. The amount of sample gas in the container was always the same (5.8–5.9 LSTP), with the exception of experiment 110218 (6.8 LSTP). Knowing that Riedmann [2011] achieved a successful separation of argon from air at -120°C, the column temperature T_{top} (measured at the top of the column) was varied between -118 and -130°C. Another important parameter is the flow of the carrier gas through the column, affecting the duration of the separation. It can be adjusted by changing the pressures at the inlet (P_{in}) and outlet (P_{out}) of the columns. After Equation 2.59, the flow through the columns is proportional to $P_{in}^2 - P_{out}^2$. Lacking the constants required to calculate the absolute flow, one can define a parameter $\tilde{I}$, which is proportional to the flow:

$$\tilde{I} = (P_{in}^2 - P_{out}^2) \cdot 10^{-6} mbar^{-2}. \tag{4.29}$$

For the experiments with the same $\tilde{I}$ (for example all with $\tilde{I}$ around 1), the distance d_{O_2-Ar} between the argon and the oxygen peak increases for falling temperatures, resulting in a better separation. Looking back at equation for the selectivity S_{ik} (2.39), which describes how well two species i and k can be separated with a certain adsorbent, this temperature dependence was expected:

$$S_{ik} = \frac{n_i/p_i}{n_k/p_k} \propto \exp\frac{\Delta H_k - \Delta H_i}{RT} .$$

n_i is the amount adsorbed of species i at the partial pressure p_i above the adsorbent and at temperature T, ΔH_i is the the isosteric heat of adsorption, which is negative, and R is the ideal gas constant. Let species i be the one, which is preferentially adsorbed, i.e. with the more negative ΔH. Then the achieved separation gets better with increasing S_{ik}, i.e. with falling temperature. However, t_{Ar}^{start} and t_{Ar}^{end} also raise with falling temperature, increasing the time required for the separation (this is best seen when comparing the results at -120°C with those at -130°C).

The effects of the variation of the helium flow, which is proportional to $\tilde{I}$, are hard to interpret due to the low reproducibility. The first three experiments at -125°C have nearly the same t_{ads}, P_{res}, P_{in}, P_{out}, and thus $\tilde{I}$, but they differ in t_{Ar}^{start} within a range of 3 min, in t_{Ar}^{total} within a range of 5.5 min, and in d_{O_2-Ar} within a range of 2.5 min. The last three experiments at -125°C have the same t_{ads}, around the same P_{res} and $\tilde{I}$, but they differ in t_{Ar}^{start} within a range of 5 min, in t_{Ar}^{total} within a range of 17.5 min, and in d_{O_2-Ar} within a range of 13 min. Experiment 110419, the only with incomplete separation of the argon from the oxygen peak at -125°C, is

Experiment	T_{top} [°C]	t_{ads} [min]	P_{res} [mbar]	P_{in} [mbar]	P_{out} [mbar]	$\tilde{I}$ [1]	t_{Ar}^{start} [min]	t_{Ar}^{end} [min]	t_{Ar}^{total} [min]	d_{O_2-Ar} [min]
110318	-118	n.a.	49.3	1440	900	1.26	8	27	19	-4
110308	-120	13	67.7	1770	1413	1.14	13	39	26	0
110309	-120	16	50	1738	1380	1.12	12	39.5	27.5	-1.5
110310	-120	20	47.5	1822	1150	2.00	7	25.5	18.5	-2
110314	-120	14	58	1410	970	1.05	9.5	34	24.5	0
110218	-120	10	72.8	1400	1100	0.75	10	29	19	1
110317	-123	20	45	1420	1010	1.00	10.5	35	24.5	2
110316	-125	21	40	1420	980	1.06	12.5	36	23.5	10.5
110502	-125	20	41.5	1410	1010	0.97	11	40	29	10
110503	-125	20	41.5	1400	957	1.04	14	40	26	8
110419	-125	15	47	2000	1300	2.31	11.5	40	28.5	-5.5
110420	-125	15	47	2540	1940	2.69	11	31.5	20.5	7.5
110421	-125	15	57	2962	2544	2.30	16	54	38	5
110315	-130	28	65	1410	950	1.09	24	44	20	>6
110414	-130	15	45	2550	1645	3.80	12	35	23	4.5

Table 4.7: The testing parameters and results of the argon separations performed with a single column. Listed for each experiment is the temperature T_{top} measured at the top of the column, the time t_{ads} taken to freeze the sample from the container over to the column, the residual pressure P_{res} in the container after the freezing over, the pressures at the inlet (P_{in}) and outlet (P_{out}) of the columns during the separation, a figure $\tilde{I}$, which is proportional to the flow through the column, the times of the start and end of the argon peak (t_{Ar}^{start}, t_{Ar}^{end}), the total width t_{Ar}^{total} of the argon peak, and the distance d_{O_2-Ar} between the end of the argon and the start of the oxygen peak. In each experiment around 5.8–5.9 L of sample were separated, with the exception of experiment 110218 (6.8 L). d_{O_2-Ar} and thus the quality of the separation increases with falling temperature and seems to decrease with rising $\tilde{I}$.

likely an outlier, with other effects being responsible. The effect that each separation is different although having the same operation parameters, was also observed by Riedmann [2011]. What was expected and what can be seen (not clearly though) is that an increase in the helium flow causes t_{Ar}^{start} to decrease, as the peak travels faster through the column. However, the faster the gas species run through the column, the less is the adsorption equilibrium reached and the worse is the achieved separation. Compared to the drop of t_{Ar}^{start}, a lesser decrease of t_{Ar}^{end} and $t_{O_2}^{start}$ is expected, resulting in a broader peak width t_{Ar}^{total} and a lesser distance d_{O_2-Ar}. From the data, at least the decrease of d_{O_2-Ar} with increasing flow is distinctly observed.

Having seen that the argon separation is principally possible with one column and that the low reproducibility hampers the interpretation of the results, the experiments were continued with multi-column separations.

4.2.7   Separations with several Columns

This section is subdivided into several paragraphs. The first covers the earliest multi-column separations, the discovery of inequalities between the columns, the handling of these inequalities, and the dependence of the separations on the helium flow. The next paragraph is about the influence of different gas sample amounts and compositions on the argon separation, while the third treats the multi-column separations after the overheating of column 6. The last paragraph shortly deals with the nitrogen peak.

First Multi-Column-Separations
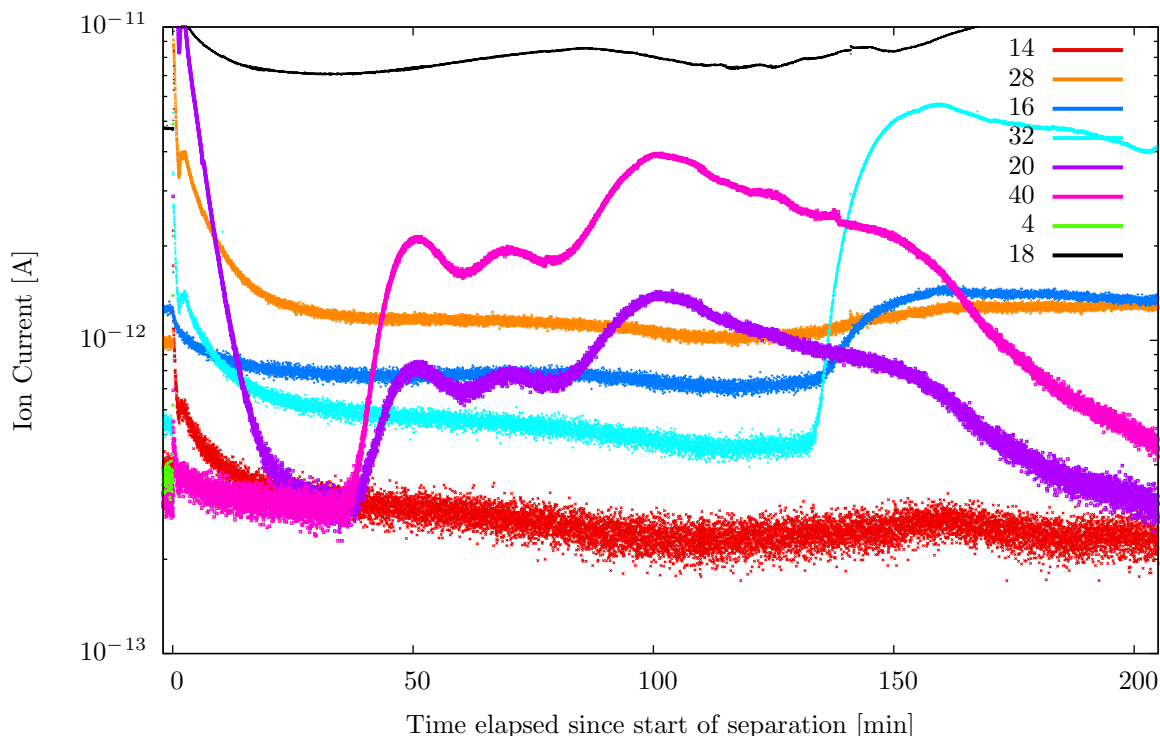
Figure 4.12: The first argon separation with all columns (experiment 110504). The rise in the mass 20 signal at the start of the experiment is again related to the simultaneous increase of the helium signal from 3.5×10^{-13} to 2×10^{-9} A. The column temperature was $-125°$C, the sample gas consisted of 50.3 LSTP ambient air, and $\tilde{I}$, which is proportional to the helium flow through the columns, was 0.6. The argon peaks of the single columns do not converge well and even merge with the oxygen peak of the "earliest" columns at these parameters.

The first argon separation with all columns (experiment 110504) is shown in Figure 4.12. The separation was performed at a column temperature of $-125°$C, an $\tilde{I}$ of 0.6, and with a sample gas amount of 50.3 LSTP ambient air. Differences of the single columns are clearly visible, as several distinct argon peaks can be distinguished. The latest argon peaks already converge with the earliest oxygen peaks, no complete separation is achieved. Possible reasons are variations in the density or the amount of the zeolite filling of the columns, or differences of the ohmic

97
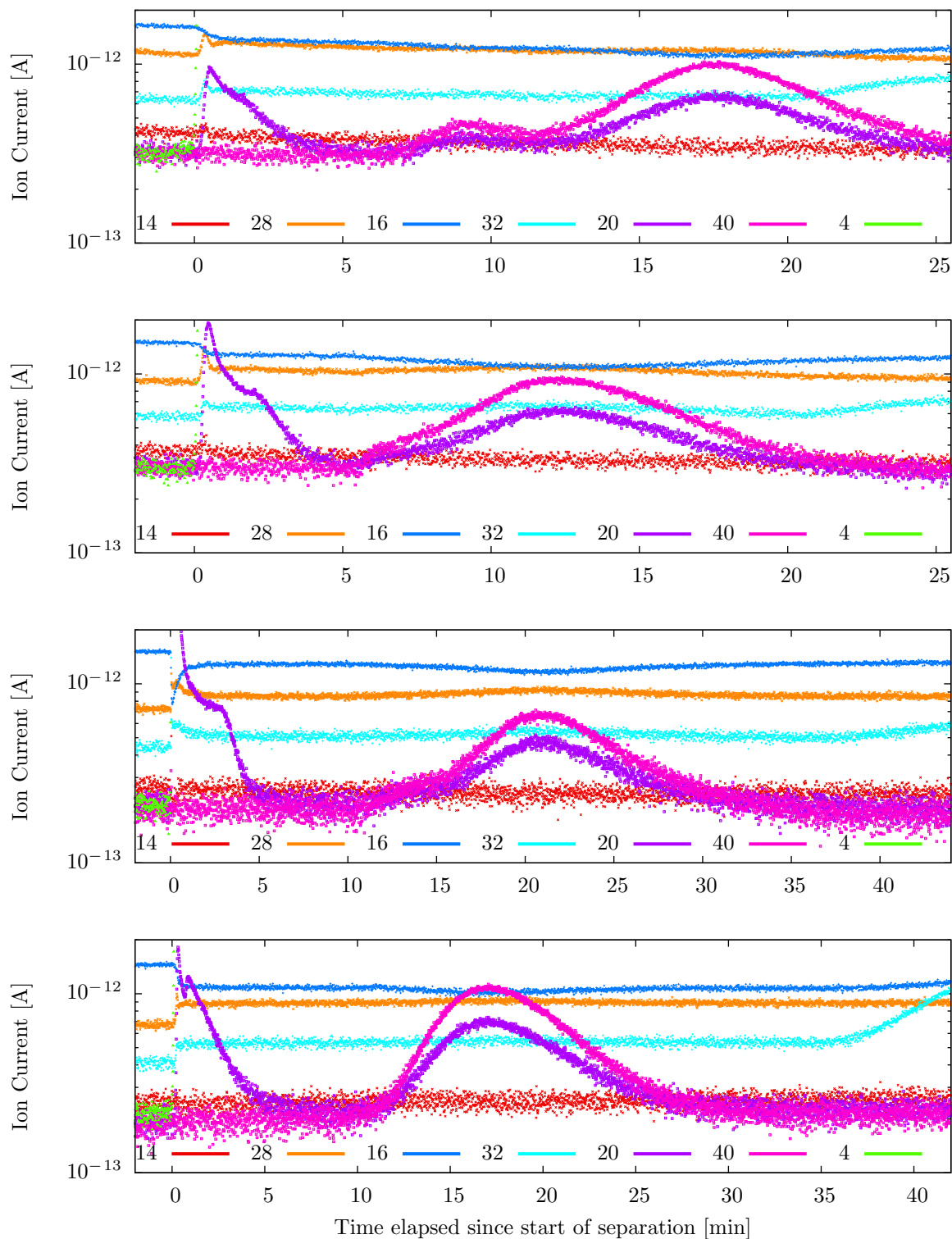
Figure 4.13: Multi-column separations of 58.5 LSTP ambient air with the following parameters: 1st: all columns, column "1" partly opened, T=− 125°C, $\tilde{I}$=1.7, 2nd: all but column "1", T=− 125°C, $\tilde{I}$=1.8, 3rd: all but column "1", column "6" partly opened, T=− 130°C, $\tilde{I}$=1.7, 4th: all but column "1", column "6" partly opened, T=− 130°C, $\tilde{I}$=3.6.

resistances of the columns. As the columns are tempered via their resistances R_i with electric current, differences in the R_i would cause the columns to have different temperatures, and hence to differ in the adsorption properties. In order to identify the columns differing the most from the rest, two separations were performed: one with half the columns, and one with the other half of the columns. In the first separation all argon peaks converged well, the second showed again distinct argon peaks. More separations were realized, cumulatively joining more columns of the second pack to the first pack. Columns C1 and C6 could be identified to cause the early peaks, with the difference of C1 to the rest being more severe. Further separations were performed to investigate how the maximum sample gas amount of around 59 LSTP can be separated. The latter is determined by the sample gas cylinder volume of around 9 L and the maximum outlet pressure of the pump used in the degassing setup (7 bar), and the normalization to standard conditions. To balance the shorter peak travel time through C1 and C6, the in- and outlet valves of these columns were only partly open, throttling the flow. The testing parameters and results of the most insightful of these experiments are summarized in Table 4.8, the corresponding chromatograms are shown in Figure 4.13. The difference between C1 and the rest is apparently too big to use this column in multi-column-separations. Its argon and oxygen peak are clearly apart from the main peak. When comparing the second separation (without C1, $-125°C$, $\tilde{I}$=1.8) with the third (without C1, C6 partly open, $-130°C$, $\tilde{I}$=1.7), one can see that d_{O_2-Ar} increases at deeper temperatures. However, the argon peak of C6 becomes more distinct, and possibly its oxygen peak, too. By increasing $\tilde{I}$ to 3.6 while retaining all other parameters from the third experiment, one achieves a very good separation (d_{O_2-Ar}=7.5 min). The effect of the higher flow is also visible when comparing the first multi-column-separation (all columns, $-125°C$, 50.3 LSTP ambient air, $\tilde{I}$=0.6, Figure 4.12) with the first experiment in Figure 4.13 (all columns, C1 partly opened, T=$-125°C$, 58.5 LSTP ambient air, $\tilde{I}$=1.7). Although the experiment with the higher flow also has a higher loading of the columns, only the argon peaks of C1 and C6 are separated from the main peak, which is also more Gaussian than the one in the experiment with the lower flow.

The reason for this behavior is unclear. As mentioned in the section about the one-column-separations, the adsorption equilibrium in the columns is the less complete, the higher the flow is. At higher flows, this effect may cause to decrease the differences between the columns. However, for the same reason, the distance of the main argon from the main oxygen peak becomes also less at higher flows. When comparing the third ($\tilde{I}$=1.7) to the forth ($\tilde{I}$=3.6) experiment in Figure 4.13, one can see that, at higher flows, the peaks become more compact and the prepeaks disappear. However, the main oxygen peak approaches the main argon peak. But since both peaks are more compact, the separation still is strongly improved.

To keep the experiments reproducible, "partly open" valves need to be defined. The used valves are fully open after a 90° twist and can be moved into a 45° ("partly open") position with sufficient reproducibility. Having both valves of C6 in this position, the flow through that column is throttled enough to balance the lesser filling or higher temperature of C6. The assumption that there is very little or no flow at all at this valve position through C6 and this is the cause for the better separation, can be excluded. During the experiments with the partly open C6, the ice forming from the ambient humidity at the outlet tube of C6 was growing at the same speed and to the same extend as on the outlet tubes of the other columns. This means, the outlet tube of C6 must be cooled by the flow to around the same temperature and the flow through C6 must have around the same order of magnitude as the flow through the other columns. During the regeneration of the columns no argon peak was observed either, which means that it already

Experi- ment	Unused columns	Partly open columns	T_{top} [°C]	$\tilde{I}$ [mbar^2]	t_{Ar}^{start} [min]	t_{Ar}^{end} [min]	t_{Ar}^{total} [min]	d_{O_2-Ar} [min]
110727	–	C1	-125	1.7	6	30	24	-10
110728	C1	–	-125	1.8	5	22	17	-1.5
110729b	C1	C6	-130	1.7	10	36.5	26.5	0
110729c	C1	C6	-130	3.6	8	28.5	20.5	7.5

Table 4.8: The testing parameters and results of the multi-column separations shown in Figure 4.13. Out of the 9 existing columns, the columns not used during the experiment and the ones, which were only partly open to regulate the flow and to compensate for inequalities, are listed. Beyond that, for each experiment the temperature T_{top} measured at the top of the column, a figure $\tilde{I}$, which is proportional to the flow through the columns, the times of the start and end of the argon peak (t_{Ar}^{start}, t_{Ar}^{end}), the total width t_{Ar}^{total} of the argon peak, and the distance d_{O_2-Ar} between the end of the argon and the start of the oxygen peak are compiled. In each experiment the same amount of ambient air was separated (58.5 LSTP). As for the separations with one column, d_{O_2-Ar} increases with falling temperature. However, unlike to the one column experiments, d_{O_2-Ar} increases with rising instead of falling $\tilde{I}$. The argon and oxygen peaks of the columns C1 and C6 appear earlier than the peaks of the rest, which causes the necessity of regulating the flow through these columns.

must have left C6 during the separation.

Multi-Column-Separations with Different Sample Amounts and Compositions

In order to investigate the impact of different sample amounts and compositions, further separations were performed. During all these experiments, the column temperature was $-130°C$, $\tilde{I}$ (which is proportional to the flow through the columns) ranged between 3.6 and 3.8, all columns but C1 were used, and the valves of column C6 were only partly open to compensate for inequalities. The sample gas was either ambient air or degassed air from groundwater, and the sample volume was varied between 32.2 and 58.5 LSTP. The varied test parameters are compiled in Table 4.9 together with the results. As expected, the distance d_{O_2-Ar} between the end of the argon and the start of the oxygen peak decreases with rising loading of the columns, as increasingly less favorable adsorption places with a lesser difference in the isosteric heat of adsorption for argon and oxygen have to be occupied. For 32.2 L ambient air, d_{O_2-Ar} ranges from 20 to 32.5 min, for 34.4 L ambient air, it ranges from 19.5 to 21 min, between 54.4 and 56.1 L ambient air, it ranges from 1.5 to 8 min, and between 57.1 and 58.5 L, it ranges from 0 to 8 min. Due to biologic activity, the air samples from degassed groundwater contain less oxygen than ambient air does. Hence, for these samples, the oxygen peak is narrower and d_{O_2-Ar} is much higher. Only during the first separation of degassed air, the start of the oxygen peak was waited for, which came 30 min after the end of the argon peak. All other separations of degassed air were canceled 10 to 20 min after the argon peak, without any trace of the oxygen peak. As all groundwater samples contained between 54.1 and 57.3 L gas, this is a huge difference compared to the separations of around 57 L ambient air. Thus, even if a separation of ambient air is only just possible with certain parameters, the separation of degassed air will still work fine with the same parameters, due to the lower oxygen content.

Experiment	V_s [LSTP]	t_{ads} [min]	P_{res} [mbar]	t_{Ar}^{start} [min]	t_{Ar}^{total} [min]	d_{O_2-Ar} [min]	Kind of sample
111013	32.2	16	18	15	25	30.5	Air
111014	32.2	9	16	13	24	21	Air
111017	32.2	10	16	12	24	22	Air
111018	32.2	14	19	13.5	24.5	20	Air
111019	32.2	10.5	15	18	26	32.5	Air
111201	34.4	16	16	14	22	21	Air
111202	34.4	20	15	13.5	22	19.5	Air
111010	54.9	15	92	8.5	21	8	Air
111020	55.3	22.5	37	8	22	1.5	Air
111021	55.3	16	21	7	22	3	Air
111026	54.3	21	22	9.5	20.5	5.5	Air
111027	55.7	21	39	9	20	5	Air
111117	54.4	17	62	7.5	21.5	1.5	Air
111118	55.1	19	56	8.5	18.5	4	Air
111129	56.1	15	62	7.5	21.5	4.5	Air
110729c	58.5	6	302	8	20.5	7.5	Air
110801	58.5	13	29	8	31	0	Air
111011	57.3	15	120	12	22	8	Air
120110	57.6	16	54	7.5	20.5	3.5	Air
120118	57.1	15	29	8	20	2	Air
120119	54.1	15	52	9	29	30	GW
120120	54.3	15	37	15	23	> 20	GW
120508	57.3	15	91	13	19	> 15	GW
120612	57.3	20	46.6	10	23	> 20	GW
120621	57.3	12	n.a.	6.5	30.5	> 10	GW

Table 4.9: The testing parameters and results of the multi-column separations performed to investigate the impact of different sample amounts and compositions. All separations were conducted at a column temperature of $-130°C$, an $\tilde{I}$ (which is proportional to the flow through the columns) between 3.6 and 3.8, using all columns but column C1, and having the valves of column C6 only partly open to compensate for inequalities. For each experiment, the total sample amount V_s, the time t_{ads} taken to freeze the sample from the container over to the columns, the residual pressure P_{res} in the container after the freezing over, the time t_{Ar}^{start} of the start of the argon peak, the total width t_{Ar}^{total} of the argon peak, the distance d_{O_2-Ar} between the end of the argon and the start of the oxygen peak, and the kind of sample (ambient air or air from degassed groundwater) are compiled. d_{O_2-Ar} decreases with higher loadings and is larger for groundwater samples than for separated ambient air, as the latter contain less oxygen than atmospheric air does.

Multi-Column-Separations after the Overheating of Column 6

As the columns are heated with electric power via their ohmic resistance and as always three columns are connected in series and the three triplets are connected in parallel circuit, the resistance should be the same for each column. This ensures that all columns have the same temperature and hence the same adsorption properties (equal filling with the zeolite provided). In addition, the resistance of each column should be as homogeneous as possible, to avoid hot spots. One of the clamps connecting C6 with the electric power acted as such a hot spot. With time, the clamp increasingly scaled, thus increasing its electrical resistance. The more it got scaled, the higher its resistance became and the higher the potential drop at the clamp got. This exponential process ended when the red glowing clamp was noticed. As only three columns are equipped with temperature sensors and these are installed at different heights, the overheating of C6 was not perceived earlier. The clamp was exchanged and the column was cleaned externally. After the overheating, in spite of the partly open valves of C6, again prepeaks of argon and oxygen were observed. The overheating seems to have damaged the filling of C6. Disassembling, refilling, and reinstalling the column would have caused one month´s worth of work for the institute´s workshop (before disassembling a single column, the clamping rings fixing all columns in a certain position and the teflon spacers electrically insulating the columns from each other have to be removed). To avoid this effort, the experiments summarized in Table 4.10 were performed to find a workaround. Each time, the column temperature was $-130°$C ($-135°$C for the last two separations) and the time taken to freeze the sample from the container over to the columns was 10 min. In the very last experiment degassed air from ground water was separated, and ambient air in all the other separations. Beside d_{O_2-Ar}, also the argon purity P and the argon recovery R were determined to evaluate the quality of the separation. In addition to C6, also the behavior of C1 was investigated again. It became apparent that the inequalities of these columns could not solely be handled by different valve positions. In the first seven experiments, closing the valves of C1 and C6 after their argon peaks left the columns was tried. However, either the purity or the recovery suffered during these separations. In the end, separations without C1 and C6 were performed. For sample amounts of around 46 LSTP, d_{O_2-Ar} ranged between 7.5 and 9.5 min, whereas for sample amounts of around 59 LSTP, d_{O_2-Ar} was 0. Despite the little distance between the end of the argon and the start of the oxygen peak, the purity ($>98\%$) as well as the recovery ($>96\%$) were excellent. Hence, one can separate the maximum sample amount of around 59 LSTP using all columns except C1 and C6 at a column temperature of $-130°$C. As seen in the paragraph about the impact of different sample compositions, d_{O_2-Ar} likely is even higher for degassed groundwater samples, due to the lower oxygen content. The residual pressure P_{res} in the sample container was a bit higher without C1 and C6 (54.3 and 82.6 mbar instead of around 30 mbar). This loss of around 1 % of the sample is still acceptable. At the cost of longer separation times, one can also go to deeper temperatures to increase d_{O_2-Ar} and reduce P_{res} even more, as demonstrated with the last two experiments in Table 4.10. With 26 min the argon peak width t_{Ar}^{total} of experiment 130226 is more than twice as wide as the one of experiment 130225. During separation 130226, air from degassed groundwater containing less oxygen than ambient air was processed, while during experiment 130225 ambient air was separated (all other parameters are the same for these separations). As more adsorption places with higher adsorption energies are available for argon when less are occupied by oxygen, the argon desorbs slower, which causes the argon peak width to increase.

Experiment	V_s [LSTP]	Unused columns	Partly used columns	P_{res} [mbar]	t_{Ar}^{start} [min]	t_{Ar}^{total} [min]	d_{O_2-Ar} [min]	$\tilde{I}$ [mbar^2]	P [%]	R [%]
120713	58.8	–	C1, C6	29.3	3	20	6.5	3.5	94.5	89.3
120815	57.9	–	C1, C6	30.3	4.5	17.5	7	3.5	97.5	87.5
120816	58.0	–	C1, C6	31	6	17	6	3.4	97.8	88.7
120817	57.8	–	C1, C6	32	5.5	19.5	2	3.6	95.3	91.5
120821	58.7	–	C1, C6	32	11	25	9	3.7	95.3	84.4
120911	58.0	–	C1, C6	35	5.5	24.5	8.5	3.6	90.7	95.4
120912	58.0	–	C1, C6	38.1	5.5	21.5	10	3.3	96.7	92.5
120913	45.7	C1, C6	–	34.7	8.5	14.5	9.5	3.9	97.8	94.5
120918	46.0	C1, C6	–	38.6	7	16.5	7.5	3.9	96.6	94.9
120919	58.9	C1, C6	–	82.6	2.5	12.5	0	3.6	98	96.2
120920	58.1	C1, C6	–	54.3	4	16	0	3.8	99.2	99.2
130225	58.7	C1, C6	–	39.6	10	11	10	3.7	98.5	95.5
130226	59.5	C1, C6	–	30.6	11	26	n. a.	3.7	99.6	n. a.

Table 4.10: The testing parameters and results for the multi-column separations performed after the overheating of column C6. All separations were conducted at a column temperature of -130°C (-135°C for the last two separations), after having the sample frozen over to the columns for 10 min. Ambient air was separated in each experiment but for the very last, where air from degassed groundwater was processed. Out of the 9 existing columns, the columns not used during the experiment and the ones which were only partly open to regulate the flow and to compensate for inequalities are listed. For each experiment, the total sample amount V_s of separated air, the residual pressure P_{res} in the container after the freezing over, the time t_{Ar}^{start} of the start of the argon peak, the total width t_{Ar}^{total} of the argon peak, the distance d_{O_2-Ar} between the end of the argon and the start of the oxygen peak, a figure $\tilde{I}$, which is proportional to the flow through the columns, as well as the purity P and recovery R of the separated argon are compiled. Only without columns C1 and C6 reliable results with both satisfying purity and recovery can be obtained.

About the Nitrogen Peak

In order to find out when the nitrogen peak emerges at $-130°$C, separation 120817 ($\tilde{I}$=3.6) was continued after the argon was trapped on the activated charcoal trap (ACT). The helium recycling was maintained, which also caused the oxygen peak to be recycled two and a half times during the experiment. If the repeated traveling of the oxygen peak through the column had had any effect at all, it would have caused the nitrogen peak to pass the column faster (as the oxygen may have occupied places no longer available for the nitrogen). Valve 8 (see Figure 4.1) was used to throttle the helium flow as substitution for the flow resistance formerly caused by the ACT, keeping $\tilde{I}$ and hence the flow at the same value. The argon peak appeared 5.5 min and the oxygen peak 27 min after the start of the separation. After 3 h without any trace of the nitrogen peak, the experiment was canceled. According to Yang [2003], the interaction energies between an isolated Li+ ion and argon, O_2, and N_2 are 21.5, 32, and 51 kJ mol^{-1}, respectively. As the used zeolite Li-LSX contains Li+ as extra framework ions, these forces should correlate in a certain manner to the peak travel times through the columns. Judging from the result of this experiment, the relation seems to be non-linear.

Chapter 5

First Field Trips

5.1 Hessisches Ried

5.1.1 Upper Rhine Graben
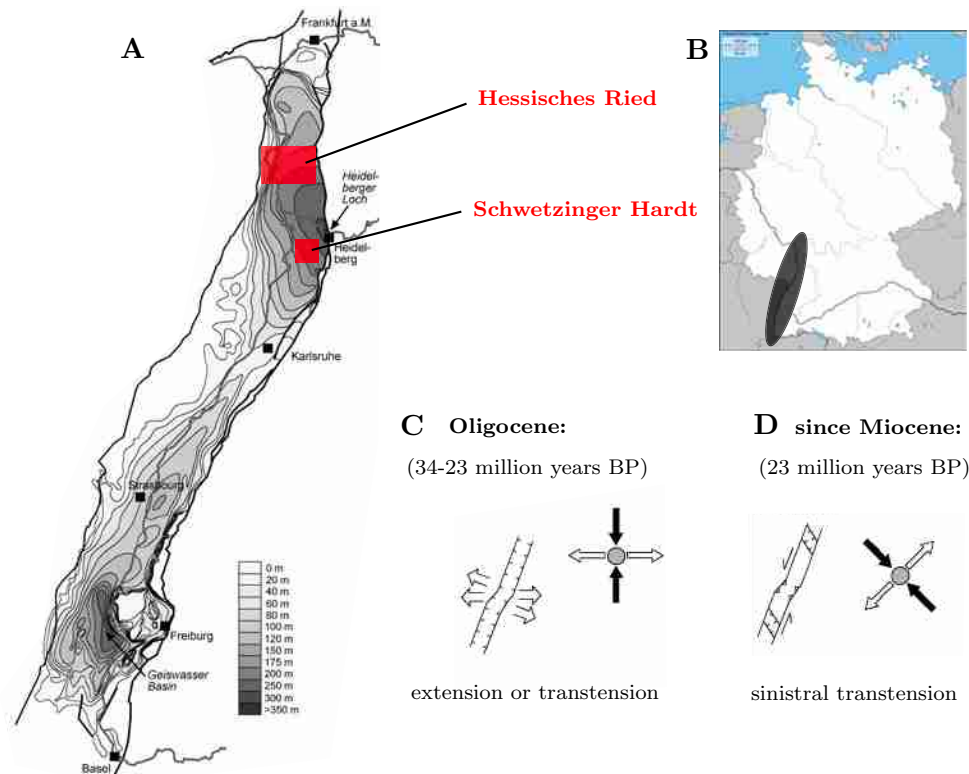
Figure 5.1: The depth contours (in meters below ground) of the base of the Quaternary deposits of the Upper Rhine Graben (URG) after Peters [2007] including the location of the study areas (A), the location of the URG (B), and past (C) and current (D) stress field after Peters [2007], leading to the evolution of the URG. The general map of Germany issues from Daniel Dalet (d-maps.com). The Quaternary deposits host the investigated aquifers.
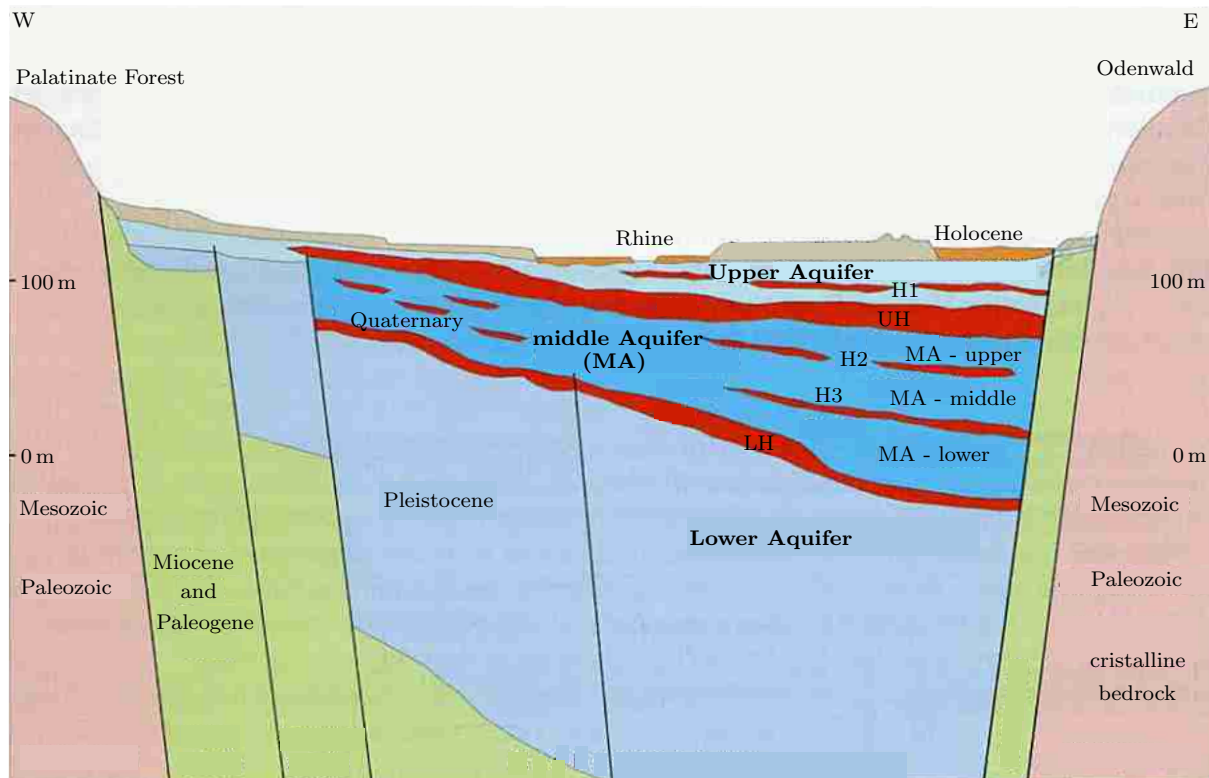
Figure 5.2: A schematic W-E-cross section of the Upper Rhine Graben in the Rhine-Neckar Region after HGK [1999]. The Upper Aquifer is separated from the Middle Aquifer (MA) by a 5-10 m thick layer of fine sands with silt and clay inclusions: the Upper Horizon (UH). The Lower Horizon (LH) is an around 10 m thick layer of comparable composition, separating the MA from the Lower Aquifer. The interim horizon H1 is neither developed in study area of the Hessisches Ried nor in the Schwetzinger Hardt. In the latter, the interim horizon H2 does not exist at all and the interim horizon H3 is only developed at well F18. A clear assignment of the interim horizons H2 and H3 is not possible in the Hessisches Ried due to a fan out in different layers and due to lack of data [HGK, 1999]. The composition of the different aquifers is sandy-gravelly.

The Hessisches Ried as well as the other study area Schwetzinger Hardt are situated in the Upper Rhine Graben (URG)(see Figure 5.1), which forms the central part of the European Cenozoic rift system (which extends from the North Sea to the Gulf of Lyon). The rift valley of the URG is around 300 km long and 30-40 km wide and opened during the Oligocene (34-23 million years before present) in consequence of an east-west oriented extensional to transtensional stress field. At the beginning of the Miocene (23-5 million years before present), the stress field reorientated, causing a persisting northwest-southeast orientated compression and northeast-southwest orientated extension of the URG [Peters, 2007]. Since then, the continuous actions of graben subsidence, uplift and erosion of the graben shoulders, as well as graben filling with sediments have shaped the URG [Illies, 1977].

The URG in the Rhine-Neckar Region

Both areas investigated in this study are located in the Rhine-Neckar Region, which is located

in the northern deposition center of the URG, where the thickness of the Quaternary sediment layers is especially high (see Figure 5.1). In the Quaternary (2.6 million years before present until now), the ongoing, relatively strong subsidence of the Heidelberger Loch resulted in the accumulation of fluvial sediments and the absence of terraces in this part of the URG [Peters, 2007]. Due to the tectonic tilt of the pre-Quaternary underground in the Rhine-Neckar Region, the thickness of the Quaternary layers increases from west to east (see Figure 5.2). The Quaternary sediments, hosting the investigated aquifers and described in HGK [1999], are an alternation of sandy-gravelly layers (the aquifers) and layers of fine sands with silt and clay inclusions (the horizons separating the aquifers). The earth surface is at around 90 to 100 m above mean sea level in this region. The base of the Upper Aquifer (UA) is at around 55–65 m above mean sea level and the UA is separated from the Middle Aquifer (MA) by the 5-10 m thick Upper Horizon (UH). The base of the MA is at around 50 m below mean sea level, where the Lower Horizon (LH) separates the MA from the Lower Aquifer (LA). In the areas investigated in this study, the smaller interim horizons H1 is not developed at all. In the Hessisches Ried, the interim horizons H2 and H3 can not be clearly assigned due to a fan out and due to the lack of data. In the Schwetzinger Hardt, H2 does not exist at all and the interim horizon H3 is only developed at well F18.
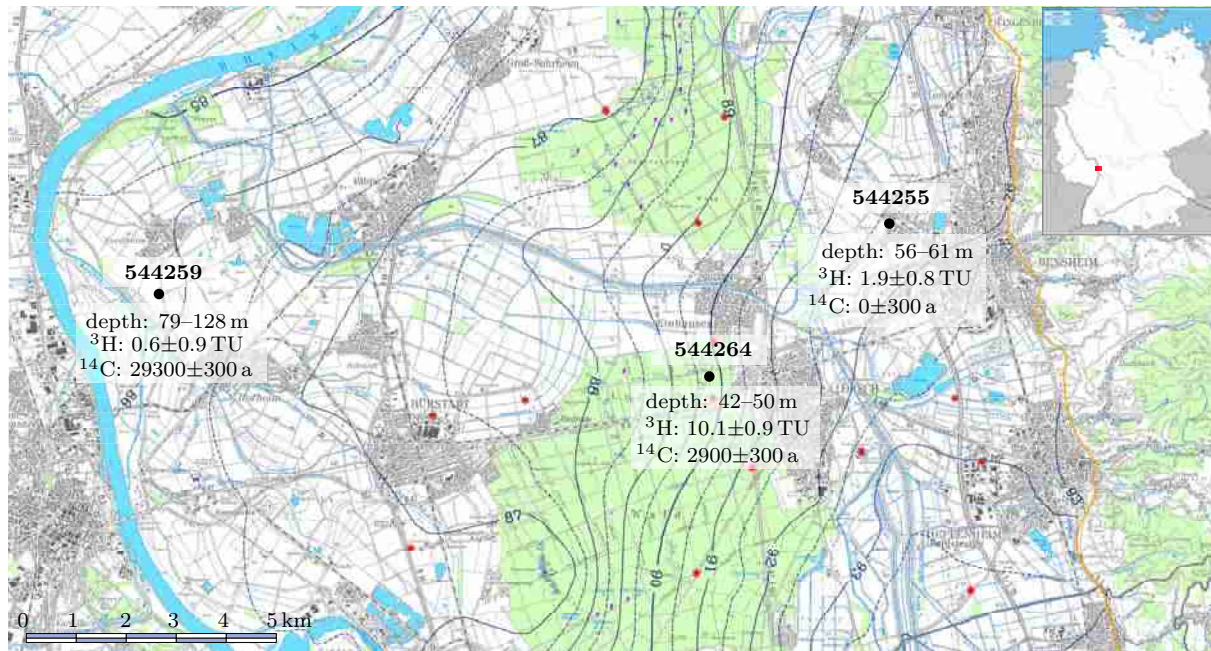
5.1.2 Study Area

Figure 5.3: A groundwater contour map (with the contour lines in meters above mean sea level) of 2012 of the study area in the Hessisches Ried, Germany, taken from the Hessisches Landesamt für Umwelt und Geologie (HLUG) and reworked. Based on the data of Krieger [2011] (see Table 5.2), the three wells were chosen for a first sampling trip for ATTA. The well numbers and depths of the well screens (in meters below ground) were provided by Krieger [2011]. ^{3}H and ^{14}C were sampled during the field trip in 2011 and measured at the IUP Heidelberg and the Klaus-Tschira-Labor für physikalische Altersbestimmung in Mannheim, respectively. The general map of Germany, where the location of the study area is indicated, issues from Daniel Dalet (d-maps.com).

For the purpose of testing the setup for water degassing in the field and for first ^{39}Ar-measurements with ATTA, three observation wells in the Hessisches Ried were chosen for sampling on basis of the data of Krieger [2011] (see Table 5.2). In the Hessisches Ried, the groundwater recharges via surface infiltration of precipitation, bank filtration of streams issuing from the Odenwald, and subsurface discharge of the Odenwald [HGK, 1999; Friedrich, 2007]. The groundwater flow is from the graben shoulder (Odenwald) in the east to the river Rhine in west-northwest direction (see Figure 5.3 for groundwater contour lines and well locations). After the investigation of the Niedersächsisches Landesamt für Bodenforschung in 1994 [Krieger, 2011], the water of the wells 544264 and 544255 tapping the Middle Aquifer (MA) have conventional ^{14}C-ages of 930 and 4500 years, respectively, and tritium concentrations of 1.8 and 3.4 TU, respectively. The dissolution of ^{14}C-free carbonates and the exchange of ^{14}C with the carbonates in the underground decreases the ^{14}C-concentration of the water and artificially increases the water age. The measurable tritium concentrations hint to a share of a younger water component. Taking this together, these two wells may have ^{39}Ar-ages falling in the range of 50-1000 years. Well 544259 (24400 years, 2.3 TU [Krieger, 2011]) taps the Lower Aquifer and might be ^{39}Ar-dead, depending on how reliable the provided tritium concentration is. The three wells do not lie directly on a

Well	F_{water} [L/min]	V_{gas}/V_{water} [ccSTP/L]	V_{gas} [LSTP]	V_{water} [L]	T_{water} [°C]	O_2 [mg/L]
HR 544255	24.9	36.8	54.2	1472	11.8	0.1
HR 544259	n. a.	24.1	53.9	2240	12.6	0.09
HR 544264	22.8	55.0	54.2	985	11	0.08

Table 5.1: The water flow rate F_{water}, the extracted gas amount per liter of water V_{gas}/V_{water}, the total extracted gas amount V_{gas}, the total amount of degassed water V_{water}, the temperature T_{water} of the groundwater, and the dissolved oxygen in the groundwater during the sampling trip in the Hessisches Ried 2011.

groundwater flow line and not all of them tap the same aquifer, but the overall expectation is that the ^{39}Ar-ages increase from the east to the west (544255 < 544264 << 544259).

5.1.3 Sampling

The sampling took place on September 20., 21., and 23., in 2011, sampling one well each day. At first at each well, the well was pumped until the borehole volume was at least exchanged once. As with the employed submersible water pump MP1 (Grundfos, Bjerringbro, Denmark), water flow rates of up to $25\,\mathrm{L\,min^{-1}}$ were realized, the pumping before sampling took between 1 and 2 h, depending on the inner diameter and the depth of the well. During the pumping, dissolved oxygen, electric conductivity, and pH of the water were measured with a multi probe (Multi 340i, from WTW, Weilheim, Germany). These parameters reached constant values even before the end of the pumping. Then, as much water was degassed as required to fill the 9 L sample gas cylinder with 6.5 bar (see Table 5.1). After the degassing, two 20 mL water samples for noble gas measurements were taken, using copper tubes as described in Wieser [2010]. Additionally, water samples for tritium (10 mL) and ^{14}C measurements (500 mL) were taken.

5.1.4 Results

The results of the field trip in the Hessisches Ried in 2011 are compiled in Table 5.2, together with the data provided by Krieger [2011] (issuing from an investigation of the Niedersächsisches Landesamt für Bodenforschung in 1994). The tritium samples taken during this study were measured at the IUP Heidelberg. For the wells 544255 and 544259, the tritium concentrations in 2011 ($1.87 \pm 0.83\,\mathrm{TU}$ and $0.63 \pm 0.90\,\mathrm{TU}$, respectively) are slightly lower than the ones in 1994 (3.4 TU and 2.3 TU, respectively). The difference is greater than radioactive decay could explain, yet still small. Mostly likely this is caused by the arrival of water with different tritium activities, which is certainly also the cause of the increase of the tritium concentration of well 544264 from 1.8 TU in 1994 to $10.09 \pm 0.90\,\mathrm{TU}$ in 2011. With the recent measurement, well 544259 can be considered ^{3}H dead.

The ^{14}C ages should be regarded rather qualitatively in the sense of younger and older water, as the dissolution of ^{14}C free carbonates and the exchange of ^{14}C with the carbonates strongly affects the ^{14}C concentration and may vary in space. The conventional ^{14}C ages measured in 2011 for this study by the Klaus-Tschira-Labor für physikalische Altersbestimmung in Mannheim cor-

		HR 544255	HR 544259	HR 544264
Tritium	[TU]	1.9 ± 0.8	0.6 ± 0.9	10.1 ± 0.9
Tritium [Krieger, 2011]	[TU]	3.4	2.3	1.8
$F^{14}C$		0.855 ± 0.004	0.025 ± 0.020	0.598 ± 0.004
conv. ^{14}C age	[a]	1260 ± 30	29790 ± 160	4120 ± 30
^{14}C age [Krieger, 2011]	[a]	930	24395	4515
Vogel ^{14}C age	[a]	0 ± 300	$29\,300 \pm 300$	2900 ± 300
^{39}Ar age	[a]			550 ± 460
Screen depth [Krieger, 2011]	[m]	56-61	79-128	42-50
T_{water}	[°C]	11.8	12.6	11
pH		6.6	7.3	6.9
DO$_2$	[mg/L]	0.10	0.09	0.08
κ_{25} [μS/cm]	[μS/cm]	905	425	1033
V_{gas}	[LSTP]	54.2	53.9	54.2
V_{water}	[L]	1472	2240	985
V_{sAr}	[ccSTP]	539.9	955.8	330.0
V_{gas}/V_{water}	[ccSTP/L]	36.8	24.1	55.0
V_{sAr}/V_{water}	[ccSTP/L]	0.37	0.43	0.34
V_{eAr}/V_{water}	[ccSTP/L]	0.42	0.49	0.38
V_{msAr}/V_{water} (sample 1)	[ccSTP/L]	0.423 ± 0.003	0.493 ± 0.004	0.408 ± 0.003
V_{msAr}/V_{water} (sample 2)	[ccSTP/L]	0.422 ± 0.003	0.490 ± 0.003	0.367 ± 0.003
NGT (sample 1)	[°C]	8.4 ± 0.8	5.3 ± 1.2	11.2 ± 1.1
NGT (sample 2)	[°C]	9.2 ± 0.9	4.3 ± 1.1	9.1 ± 0.3

Table 5.2: For the investigated wells in the Hessisches Ried, measurements performed in 2011 during this study together with data provided by Krieger [2011] (issuing from an investigation of the Niedersächsisches Landesamt für Bodenforschung in 1994) are compiled. For the samples taken during this study, tritium concentrations were measured at the IUP Heidelberg, while ^{14}C concentrations and ages were determined by the Klaus-Tschira-Labor für physikalische Altersbestimmung in Mannheim. The depths of the well screens are given in meters below ground. The ^{39}Ar age was measured by the ATTA group Heidelberg. The temperature T_{water}, the pH, the dissolved oxygen DO$_2$, and the electric conductivity κ_{25} of the well water were measured in the field. V_{gas} is the total amount of degassed air, V_{water} the amount of degassed water, V_{sAr} the amount of separated argon from the degassed air, V_{gas}/V_{water} the amount of degassed air per liter of water, V_{sAr}/V_{water} the amount of separated argon per liter of water, V_{eAr}/V_{water} the argon concentration in the water estimated via the argon degassing efficiency of 90.4 % and the argon recovery of 98 % of the separation, and V_{msAr}/V_{water} is the argon concentration measured with the MM5400. Noble gas concentrations were measured at the IUP with the sector field mass spectrometer MM5400 described in Friedrich [2007] and Wieser [2010]. The noble gas temperatures (NGTs) were fitted with the routine described in Jung et al. [2013] using the CE-model. For noble gas measurements, two samples were taken per well and both results for the NGTs are listed.

respond well with the conventional ^{14}C ages provided by Krieger [2011] and issuing from 1994. As in the data provided by Krieger [2011], the ages increase from the mountain range Odenwald in the east to the river Rhine in the west (1260 ± 30 years, 4120 ± 30 years, and 29790 ± 160 years for the wells 544255, 544264, and 544259, respectively). This fits to the groundwater flow, which is in west-northwest direction and perpendicular to the groundwater contour lines (see Figure 5.3). Using the Vogel model [Vogel, 1967, 1970] for the ^{14}C ages and regarding the ^{14}C concentration of well 544255 ($F^{14}C = 0.855 \pm 0.03$) as the modern for this region, one arrives at the following water ages: 0 ± 300 years for well 544255, 2900 ± 300 years for well 544264, and 29300 ± 300 years for well 544259. The error of $F^{14}C$ was adjusted to account for the uncertainty caused by assuming the same carbonate chemistry for the entire study area. One has to note that the screens of the wells 544255 and 544264 are in around the same depth (61-56 and 50-42 m below ground) and tap the Middle Aquifer, while the screen of well 544259 is located deeper (128-79 m below ground) and taps the Lower Aquifer. Hence, composition of the water flowing through the screen of well 544259 is likely very different from the other wells. However, possible inflows to the Lower from the Upper Aquifer through windows in the aquitard between can not be excluded. Measurable tritium concentrations in all wells also hint to a mixing of different waters. Following HGK [1999]; Friedrich [2007], the groundwater recharge in the Hessisches Ried happens via surface infiltration of precipitation, bank filtration of streams issuing from the Odenwald, and subsurface discharge of the Odenwald. [39]Ar-measurements can help to better understand this mixture, however, so far only well 544264 was preliminarily dated by the ATTA group Heidelberg (550 ± 460 years).

With around 0.1 mg/L, the dissolved oxygen (DO_2) is far from saturation (around 11 mg/L at that temperature) for all wells. The measured groundwater temperatures range from 11 to 12.6 °C and correlate with the depth of the well screens, with the deeper having higher temperatures. The pH of the well water is between 6.6 and 7.3, with the highest value for the deepest well (544259). With 425 μS/cm, the electric conductivity κ_{25} of the deepest well (544259) is much lower than for the other wells (905 μS/cm and 1033 μS/cm for the wells 544255 and 544264, respectively).

The overall gas content of well 544259 is by far the lowest and the water was color- and odorless, while the water of the other wells was red-brownish and had a hydrogen sulfide smell. To fill the sample gas cylinder with 54 LSTP, 2240 L of water had to be degassed for well 544259, whereas 1472 L for well 544255 and only 985 L for well 544264 had to be degassed (see Table 5.1). The degassed air per liter of water is 24.1 ccSTP/L for well 544259, 36.8 ccSTP/L for well 544255, and even 55.0 ccSTP/L for well 544264. As a non negligible quantity of gas would have been lost during a determination of the composition of the degassed air with the current setup for argon separation, such a determination was omitted. However, there are several indicators that the composition is non atmospheric. As mentioned above, there is virtually no oxygen dissolved in the well water. Additionally, during the regeneration of the separation columns, much higher CO_2 amounts were released by the zeolite as during the experiments performed with ambient air. Although the degassed air per liter of water is the lowest for well 544259, with 0.43 ccSTP/L the separated argon per liter of water (V_{sAr}/V_{water}) is the highest (compared to 0.37 ccSTP/L for well 544255 and 0.34 ccSTP/L for well 544264). It is unlikely that this is a consequence of decreased degassing efficiency η during the sampling of the latter two wells. The pressure at the gas ports of the membrane contactor, which is the main influence factor of η, was not significantly higher as during the sampling of well 544259. Furthermore, the argon recoveries of the separation vary only by a few percent, which can not cause these differences. The lesser

argon content of the other two wells could be rather a sign of naturally occurring degassing of the groundwater, as the overall gas content of the wells 544255 and 544264 is much higher and a portion might have already degassed, also causing the other gases (as argon) partly to degas. By dividing V_{sAr}/V_{water} by the argon degassing efficiency (around 90.4 %)and the argon recovery of the setup for argon separation (around 98 %), one can estimate the argon concentrations V_{eAr}/V_{water} of the well water. These estimated concentrations lie very close to the argon concentrations V_{msAr}/V_{water} determined with the sector field mass spectrometer MM5400 at the IUP (see Table 5.2), confirming the values for the degassing efficiency and argon recovery. As more water was degassed for well 544259 than for the other wells and the amount of degassed argon per liter was also the highest, with 955.8 ccSTP the total amount of separated argon V_{sAr} is also the highest for this well. For well 544255, V_{sAr} is 539.9 ccSTP, and for well 544264, V_{sAr} is even only 330 ccSTP.

Noble gas concentrations of both samples per well were measured at the IUP with the sector field mass spectrometer MM5400 described in Friedrich [2007] and Wieser [2010]. The noble gas temperatures (NGTs) were fitted with the routine described in Jung et al. [2013]. The CE-model yielded the best fits. The samples were measured during a time, when the precision of noble gas measurements with the MM5400 was lower than normally. This causes the determined NGTs of the two samples per well to deviate from each other. The NGTs determined for the younger wells are lower than the mean annual air temperatures of the period 1981-2010 of around 11 °C for this region (taken from the Deutscher Wetterdienst (DWD)), which agrees well with the measured temperature T_{water} of the well water during sampling (11.8°C for well 544255, and 11.0°C for well 544264). The NGTs for well 544255 are 8.4±0.8 °C and 9.2±0.9 °C, the ones for well 544264 11.2±1.1 °C and 9.1±0.3 °C. Since measurable tritium concentrations were found in the water of these wells, they contain at least a portion of young water infiltrated not much longer than 50 years ago. Hence, the offset between T_{water} and NGT is unexpected. This offset may be caused by oxygen depletion due to biology. If the depletion already occurs in the unsaturated zone and not at the water table, and if the lost partial pressure of oxygen is not replaced by the same amount of CO_2 (or other products), the pressure difference is replenished with more air (which also becomes depleted in oxygen). Hence, the partial pressures at the water table of the noble gases (and nitrogen) are increased, causing the gas concentrations in the water to also increase according to the Henry´s law. Without correction and still assuming the normal partial pressures at the water table, the NGTs obtained with the CE-model appear lower (as lower temperature also caused more gas to become dissolved in water). By adjusting the recharge altitude (and hence the partial pressures) for the CE-model, one could correct for this effect. However, it is highly uncertain if the oxygen depletion has always been the same in the past. In any case, the NGTs of these two wells are Holocene, while the NGTs of the oldest well (544259) are clearly glacial (5.3±1.2 °C and 4.3±1.1 °C). This also fits to the ^{14}C age of 29792 years for this well.

Conclusion

While the results obtained for the younger wells are hard to interpret due to the lack of [39]Ar ages and possibly occurring oxygen depletion, the water from deep well 544259 is of interest. A high ^{14}C age after the Vogel model (29300±300 years), a low tritium concentration (0.63±0.90 TU), and glacial NGTs indicate that this well may be dead in [39]Ar if subsurface production is neg-

ligible. ^{39}Ar free argon is required by ATTA for tests of the internal ^{39}Ar background and to prepare calibration gases (consisting of mixtures of modern and ^{39}Ar free argon). A sample of separated argon was sent to Bern for confirmation, but has not been measured so far.

5.2 Schwetzinger Hardt

5.2.1 Study Area

F10/2
depth: $55 - 88\,\text{m}$
^{3}H: $0.32\pm0.03\,\text{TU}$
^{14}C: $620\pm300\,\text{a}$

F10/3
depth: $120 - 147\,\text{m}$
^{3}H: $0.004\pm0.016\,\text{TU}$
^{14}C: $1200\pm300\,\text{a}$

F18/2
depth: $65 - 73\,\text{m}$
^{3}H: $7.4\pm0.2\,\text{TU}$
^{14}C: $0\pm300\,\text{a}$

GOE15/2
depth: $47 - 51\,\text{m}$
^{3}H: $0.01\pm0.02\,\text{TU}$
^{14}C: $1300\pm300\,\text{a}$

GOE15/3
depth: $108 - 112\,\text{m}$
^{3}H: $0.01\pm0.02\,\text{TU}$
^{14}C: $630\pm300\,\text{a}$
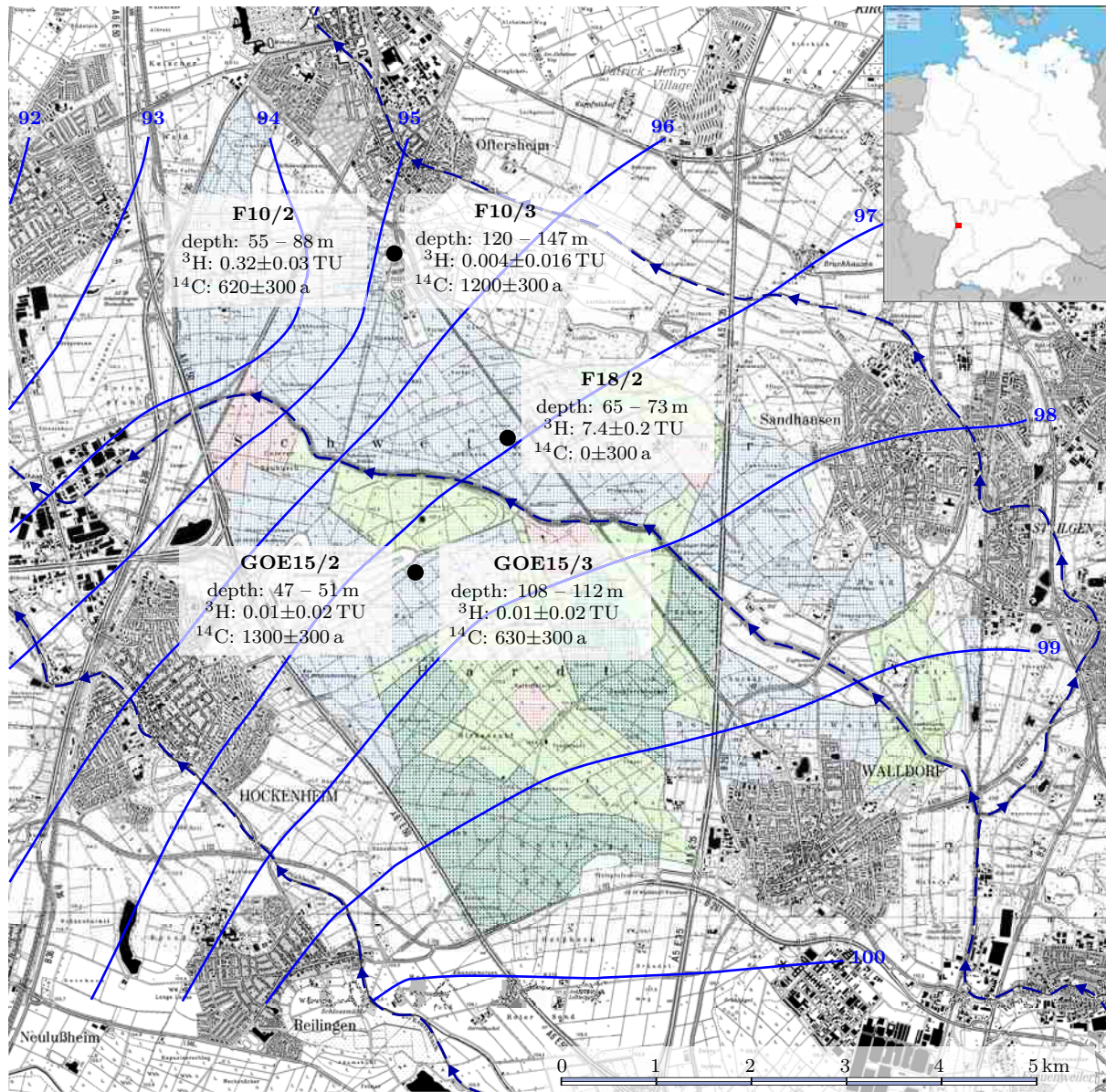
Figure 5.4: A map of the study area in the Schwetzinger Hardt. The well numbers, depths of the well screens (in meters below ground), ^{3}H concentrations, and ^{14}C ages are taken from Aeschbach-Hertig [2012]. On the basis of the the data of Aeschbach-Hertig [2012], these five wells were chosen for an investigation of ^{39}Ar ages and noble gas temperatures. The basic map issues from the Regierungspräsidium Freiburg (2012), the groundwater contour lines (solid lines) were redrawn after another map from the Regierungspräsidium Freiburg, issuing from 1990. Streams are represented by broken lines. The general map of Germany, where the location of the study area is indicated, is taken from Daniel Dalet (d-maps.com).

Well	F_{water} [L/min]	V_{gas}/V_{water} [ccSTP/L]	V_{gas} [LSTP]	V_{water} [L]	T_{water} [°C]
SH F10/2	36.1	21.8	59.7	2668	11.3
SH F10/3	27.5	23.4	59.3	2489	12.8
SH F18/2	29	23.9	59.7	2461	10.7
SH GOE15/2	29.4	22.3	59.7	2632	11.2
SH GOE15/3	28.8	27.1	59.3	2152	12.8

Table 5.3: The water flow rate F_{water}, the extracted gas amount per liter of water V_{gas}/V_{water}, the total extracted gas amount V_{gas}, the total amount of degassed water V_{water}, and the temperature T_{water} of the groundwater during the sampling trip in the Schwetzinger Hardt 2012.

The Schwetzinger Hardt, as the other study area Hessisches Ried, is located in the Rhine-Neckar Region in the Upper Rhine Graben (URG), which is described in Section 5.1.1. The groundwater flow is from the uplifted graben shoulder in the east (Odenwald) to the Rhine River in northwest direction (see Figure 5.4 for the groundwater contour lines and the location of the sampled wells). The five observation wells investigated during this study are a subset of more than 20 wells, which have been sampled for SF_6, tritium, ^{14}C, and stable isotopes in October 2011 [Aeschbach-Hertig, 2012], all tapping the Middle Aquifer (MA). The interim horizons H2 and H3, separating the MA in the Rhine-Neckar Region into an upper, middle, and a lower part, are poorly developed in the Schwetzinger Hardt (see HGK [1999]). H2 does not exist at all, and H3 was found only at well F18. Hence, the classification into a lower MA (lMA, 100-150 m below ground) and an upper MA (uMA, 50-100 m below ground) should be regarded with care. Overall, wells reaching the Middle Aquifer are tritium free and the water must have infiltrated prior to the first nuclear bomb tests in the 1950s. The wells F18/2 (7.4 ± 0.2 TU) and F10/2 (0.32 ± 0.03 TU) represent exceptions, with portions of younger waters. For ^{14}C dating of the water, Aeschbach-Hertig [2012] chose the Vogel model, which accounts for the dissolution of ^{14}C free carbonates by setting the initial ^{14}C concentration to a lower value than the atmospheric concentration ($F^{14}C=1$). Taking into account that a part of the ^{14}C-concentrations in the younger wells also issues from the bomb tests, Aeschbach-Hertig [2012] ended with an estimate of $F^{14}C=0.81 \pm 0.03$ for the initial ^{14}C activity. As the dissolution of ^{14}C free carbonates may vary in space and the exact part of the ^{14}C concentration arising from the bomb tests is unknown, the initial ^{14}C concentration of the water in the study area has a high uncertainty. This results in errors of at least ±300 years for the ^{14}C ages, which range from 0 to 1300 years for the five wells chosen for sampling during this study. ^{39}Ar dating of these wells can help to better constrain the water ages.

5.2.2   Sampling

In June 2012, together with a team from the University Bern, five wells in the Schwetzinger Hardt were sampled for comparison measurements between ATTA (Heidelberg) and the low level counting underground laboratory (Bern). The pumped water was split and both teams degassed in parallel. Hence, a complete comparison of the respective procedure of groundwater degassing, argon separation, and the eventual ^{39}Ar - measurement is possible. The wells F10/2, F10/3, and F18/2 were sampled on June 5th, while the wells GOE15/2 and GOE15/3 were

sampled on June 6th. At first at each well, the well borehole was pumped until the borehole volume was at least exchanged once. Then, as much water was degassed as required to fill the 9 L sample gas cylinder with 7 bar (see Table 5.3). This amount ranges from 2152 L for well GOE15/2 to 2668 L for well F10/2. After the degassing, two 20 mL water samples for noble gas measurements were taken, using copper tubes as described in Wieser [2010]. At the wells F10/2 and F10/3, for the determination of the degassing efficiency of different elements and isotopes (see Section 3.2.3), also two samples for noble gas measurements of the degassed water leaving the setup for water degassing were taken per well. At the exit of the setup, a T-piece was installed to avoid throttling of the water flow during the sampling. Instead of 20 mL, 40 mL water samples were taken to increase the precision of the noble gas measurement (as the degassed water contains less gas). Additionally, a 500 mL water sample for potential tritium or stable isotope measurement was taken per well (which were not measured so far).

5.2.3   Results

So far, only the samples from the wells F10/3 and GOE15/2 were measured with ATTA and the samples from the wells F10/2, F10/3, and F18/2 with LLC in Bern ([Purtschert, 2013]). The results together with the data from Aeschbach-Hertig [2012] (depths of the well screens, tritium, ^{14}C) and the noble gas temperatures (NGTs) determined in this study are compiled in Table 5.4. The age of the sample from well F10/3 measured with ATTA is 377±66 years, while LLC in Bern obtained 133±55 years. The causes of this deviation remain unclear. Contamination of the Bern sample with modern air is unlikely, as the extracted gas samples virtually do not contain any oxygen [Purtschert, 2013]. An overestimation of the count rate of ATTA appears possible. Before and after measuring the sample, the count rates of ATTA were determined with modern air. The higher one was used for the age calculation. If a lower count rate is correct, this may have the sample appear older than it is. The other well, GOE15/2, is 360±60 year old according to the ATTA determination. The LLC measurements of the samples from the wells GOE15/2 and GOE15/3 are still not terminated. For the wells F10/2 and F18/2, LLC yielded ages of 50±44 and 54±45 years, respectively. Except for well F18/2, the received ^{39}Ar ages are lower than the ^{14}C age estimated with the Vogel model by Aeschbach-Hertig [2012]. As expected, the employing ^{39}Ar helped to further constrain the groundwater age.

The NGTs range from 6.8°C to 9.0°C, which is significantly lower than the mean annual air temperature (MAAT) of around 11°C of this region (the average MAAT of the period 1981-2010 taken as a basis, provided by the Deutscher Wetterdienst (DWD)). The water temperatures T_{water} measured in this study of the shallower wells range from 10.7°C to 11.3°C, perfectly reflecting the MAAT. Especially for the youngest wells F10/2 and F18/2 this deviation of the NGTs from MAAT and T_{water} is unexpected. A dominant contribution of groundwater recharged at higher elevations of the mountain range in the east (colder recharge temperature) is unlikely judging from the young groundwater ages. However, the dissolved oxygen concentration of all wells is less than 0.4 mg/L (see [Aeschbach-Hertig, 2012]). Like in the Hessisches Ried, oxygen depletion may have the NGTs appear colder. When oxygen is already consumed by biology in the unsaturated zone (and not just at the water table) and not replaced by an equivalent amount of CO_2 (or other products), the pressure difference is replenished with more air (which also becomes depleted in oxygen). This results in an increase of the partial pressures of the noble gases (and nitrogen) at the water table, causing the dissolved noble gas concentrations also to

Well	Depth [m]	Tritium [TU]	^{14}C age [a]	^{39}Ar age ATTA [a]	^{39}Ar age LLC [a]	NGT [°C]
SH F10/2	53 − 88	0.32 ± 0.03	620 ± 300		50 ± 44	6.8 ± 0.7
SH F10/3	120 − 147	0.004 ± 0.016	1200 ± 300	377 ± 66	133 ± 55	9.0 ± 0.8
SH F18/2	65 − 73	8.5 ± 0.2	0 ± 300		54 ± 45	7.8 ± 0.6
SH GOE15/2	47 − 51	0.01 ± 0.02	1300 ± 300	360 ± 68		8.5 ± 0.7
SH GOE15/3	108 − 112	0.01 ± 0.02	630 ± 300			7.6 ± 0.7

Table 5.4: A compilation of the measurement results of trip in the Schwetzinger Hardt 2012, together with data from Aeschbach-Hertig [2012] (issuing from 2011). The depths of the well screens (in meters below ground), the tritium concentrations and the ^{14}C ages are taken from Aeschbach-Hertig [2012]. The ^{39}Ar ages determined so far by the ATTA group Heidelberg and by LLC in Bern ([Purtschert, 2013]) are listed. Noble gas concentrations were measured with the sector field mass spectrometer MM5400 described in Friedrich [2007] and Wieser [2010]. The noble gas temperatures (NGTs) were fitted with the routine described in Jung et al. [2013] using the CE-model.

increase. If not corrected for by adjusting the partial pressures in the CE-model via a decrease of the recharge altitude, the higher dissolved noble gas concentrations are misinterpreted as lower NGTs. Such a correction was omitted as it is not certain, if the oxygen depletion has always been the same in the past. Having NGT uncertainties between 0.6 and 0.8°C, offsets possibly caused by oxygen depletion (which do not have to be the same for all wells), and only small variations in the NGTs, it is hard to interpret the NGTs. The relative Neon excess lies between 20% and 25% for all wells, giving no additional hints. There is no clear correlation to depth or location. The only observed correlation is that the potentially oldest waters from wells F10/3 and GOE15/2 have the highest NGTs (9.1±0.9°C and 8.5±0.8°C, respectively).

Table 5.5 compiles for the sampled wells the extracted gas amount V_{gas}/V_{water} per liter of water, the amount V_{sAr}/V_{water} of separated argon per liter of water, the argon concentrations V_{eAr}/V_{water} in the water estimated by dividing V_{sAr}/V_{water} by the argon degassing efficiency of 90.4 % and the argon recovery of 98 % of the separation, and the argon concentrations V_{msAr}/V_{water} in the water measured at the IUP Heidelberg with the sector field mass spectrometer. As for the campaign in the Hessisches Ried, V_{eAr}/V_{water} and V_{msAr}/V_{water} agree well. The underestimated argon content for the wells F10/3 and F18/2 is very likely caused by an underestimation of the amount V_{sAr} of separated argon. Apparently, the equilibrium pressure in the activated charcoal trap (ACT) was not reached during the argon release when the pressure was read out to determine V_{sAr} by applying the factor f_{VSTP} (see Section 4.2.2)[1]. The spread in V_{gas}/V_{water} is lesser in the Schwetzinger Hardt than in the Hessisches Ried. At the majority of the wells, between 22 and 24 ccSTP were degassed per liter of water. Only well GOE15/3 is an exception, with 27.1 ccSTP degassed per liter of water.

---

[1]The argon transfer from the ACT to the storage container is unaffected by reading out the pressure before the equilibrium pressure is reached in the ACT and starting the transfer earlier. The transfer is still complete.

Well	V_{gas}/V_{water} [ccSTP/L]	V_{sAr}/V_{water} [ccSTP/L]	V_{eAr}/V_{water} [ccSTP/L]	V_{msAr}/V_{water} [ccSTP/L]
SH F10/2	21.8	0.41	0.46	0.454±0.004
SH F10/3	23.4	0.37	0.41	0.436±0.003
SH F18/2	23.9	0.32	0.36	0.436±0.003
SH GOE15/2	22.3	0.38	0.43	0.432±0.003
SH GOE15/3	27.1	0.39	0.44	0.432±0.003

Table 5.5: The extracted gas amount V_{gas}/V_{water} per liter of water, the amount V_{sAr}/V_{water} of separated argon per liter of water, the argon concentration V_{eAr}/V_{water} in the water estimated by dividing V_{sAr}/V_{water} by the argon degassing efficiency of 90.4 % and the argon recovery of 98 % of the separation, and the argon concentration V_{msAr}/V_{water} in the water measured at the IUP Heidelberg with the sector field mass spectrometer MM5400 described in Friedrich [2007] and Wieser [2010].

Chapter 6

Summary

6.1 Conclusion

During this work, a setup for water degassing and a setup for argon separation from air have been developed, with the aim of dating groundwaters of intermediate age with ^{39}Ar, using atom trap trace analysis (ATTA). To enable comparison measurements between the Heidelberg ATTA group and the underground lab of Bern, which requires more than $0.5\,$LSTP of pure argon, and as the argon consumption of ATTA currently is in the same order, the setup for water degassing was constructed for degassing thousands of liters of water and the setup for argon separation was constructed to process tens of liters of gas.

The setup for water degassing consists of a commercial membrane contactor (Liqui-Cel 6x28 Extra Flow, Membrana, Charlotte, North Carolina), two membrane pumps serving as vacuum pump and compressor, respectively (KNF Neuberger GmbH, Freiburg, Germany), various pressure and temperature sensors to control the procedure (WIKA Alexander Wiegand SE & Co. KG, Klingenberg, Germany), two water filters to protect the contactor from suspended particles (Infiltec GmbH, Speyer, Germany), and sample gas cylinders for collection and storage of the degassed air. During the degassing, the pressure at the gas and water ports of the contactor, the water temperature, and the pressure in the sample cylinder are read out and logged using a laptop running LabView software (National Instruments Germany GmbH, Munic, Germany). Tests in the lab and in the field (Hessisches Ried, Schwetzinger Hardt, Paris Basin) were performed. As a membrane contactor with a high maximum water flow rate ($183\,$L/min) was chosen and generally only much lower flow rates can be realized in the field (around $35\,$L/min), the water flow rate is not a restrictive parameter with respect to the degassing efficiency. Higher flow rates will decrease the residence time of the water in the contactor and thus should decrease the degassing efficiency. Due to the oversizing this effect was not observed at the flow rates realized so far. In a master thesis, Kollefrath [2011] investigated the influence of water temperature and the pressure at the gas port of the contactor on the degassing efficiency and found that this pressure is the critical parameter of the setup. While water temperature has no effects in the investigated range of 10-20°C, the degassing efficiency rapidly decreases with increasing pressure at the gas ports of the contactor. In this work, the degassing efficiencies of the setup were determined for different gas species. Noble gas measurements of the sample water before

and after degassing were performed. The efficiencies differ for the gas species (around 88 % for oxygen, 84 % for helium, 87 % for neon, 90 % for argon, 87 % for krypton, and 82 % for xenon). However, judging from the data, isotope fractionation is negligible (such a fractionation could have altered the ^{39}Ar/^{40}Ar-ratio and hence distorted the ^{39}Ar-age).

A setup for argon separation from air similar to the one constructed by Riedmann [2011] was developed in this work. It consists of nine gas chromatographic columns filled with zeolite Li-LSX as selective adsorbent, a quadrupole mass spectrometer (QMA200, Pfeiffer Vacuum, Asslar, Germany) to observe the composition of the gas leaving the columns, an activated charcoal trap to catch the argon, a water trap, and several pressure sensors. The membrane pumps of the setup for water degassing are used to recycle the carrier gas helium. Argon leaves the columns first as the interaction energy between argon and Li-LSX is weaker than between oxygen or nitrogen and the zeolite. When the entire argon peak is caught on the activated charcoal trap, the separation is stopped and the columns can be regenerated. The separation of argon from oxygen and nitrogen strongly depends on temperature, with temperatures between -130 and -135°C being the most favorable. These low temperatures are realized by immersing the columns in the vapor above a surface of liquid nitrogen and controlled by heating the steel columns by leading an electrical current through their walls. The complete separation procedure consisting of cooling and loading of the columns, separation, trapping and further processing of argon, as well as regeneration of the columns and traps takes about 8 hours. Samples of ambient air and air from degassed groundwater of more than 63 LSTP can be processed with the setup, achieving argon purities ranging from 98 to 99.6 % and argon recoveries between 96.5 and 99.2 %. As for the degassing procedure, no isotope fractionation was observed for the argon separation. Furthermore, it was found that air from degassed groundwater is far less critical to separate than atmospheric air, due to the lower oxygen content.

First field trips with the setup for water degassing were conducted, sampling aquifers not far away from Heidelberg. In the Hessisches Ried, three wells were investigated. Preliminary dating of one of these wells (544264) with ATTA yields an age of 550±460 years. In the water of the two youngest wells (544255 and 544264) measurable tritium concentrations were detected (1.9±0.8 TU and 10.1±0.9 TU, respectively). Hence, these wells contain at least a portion of young water. The obtained noble gas temperatures (NGTs) for these wells are significantly lower than the mean annual air temperature of this region and the measured well water temperature, which may be a result of oxygen depletion due to biology in the unsaturated zone. The third investigated well (544259) in the Hessisches Ried is a deep well tapping the Lower Aquifer. The determined activities of tritium (0.6±0.9 TU) and ^{14}C (F^{14}C=0.598±0.004) indicate that the well may be ^{39}Ar dead if sub-surface production is negligible. The calculated NGTs of that well (4.3±1.1°C and 5.3±1.2°C) are clearly glacial and further support the estimation that the well may be dead in ^{39}Ar. One argon sample of that well was sent to Bern for a final confirmation, but has not been measured so far. Finding a well with zero ^{39}Ar activity in the surroundings of Heidelberg is important for providing the ATTA group with ^{39}Ar free argon. This gas is needed to measure the ^{39}Ar background of the ATTA setup, which was optimized with the help of argon highly enriched in ^{39}Ar. Another application of the ^{39}Ar dead argon is the preparation of mixtures of known ^{39}Ar activity for calibration of ATTA.

In order to enable a direct comparison between the setups of Bern and Heidelberg including all steps from degassing to the final ^{39}Ar measurement, a joint field trip in the Schwetzinger Hardt was conducted. Both teams degassed groundwater simultaneously using their respective equipment. So far, the samples from the wells F10/3 and GOE15/2 were measured with ATTA

and the samples from the wells F10/2, F10/3, and F18/2 with LLC, enabling only a comparison for the obtained ages of well F10/3. The age determination for that well with ATTA yielded 377 ± 66 years, while LLC obtained an age of 133 ± 55 years. A contamination of the Bern sample is unlikely and the overestimation of the count rate of ATTA seems to be the reason for the difference. The determined NGTs for the wells in the Schwetzinger Hardt are significantly lower than the mean annual air temperature of this region. Like for the NGTs in the Hessisches Ried, oxygen depletion in the unsaturated zone seems to be the cause.

6.2 Outlook

Once the Heidelberg ATTA group will have solved the background problem issuing from the tests performed with argon highly enriched in ^{39}Ar for adjusting purposes, recycling of the argon samples during the ATTA measurement will be possible, resulting in a reduction of the sample size to less than 1 ccSTP of argon (corresponding to about 100 ml of air, 2.5 L of water or 1 kg of ice). This will enable comfortable dating of glacier ice and ocean water with ^{39}Ar at a fraction of today´s effort, which is caused by the huge sample sizes required for LLC. Also, the efforts of groundwater sampling for ^{39}Ar will be heavily reduced. Today, ^{39}Ar-dating is still a cumbersome technique, which is, if employed at all, often applied to only a few samples or not available at all for many research groups. ATTA is on the way of making ^{39}Ar-dating the standard tool for the investigation of waters in the intermediate age range of 50-1000 years. A range, which is not covered by any other reliable tracer. In the context of the Heidelberg ATTA collaboration, Schwefel [2011] already developed a simpler method to separate argon from small amounts of gas. Unlike as for huge samples of several tens of liters of gas, the removal of reactive gases by irreversible chemisorption (gettering) is economically possible for samples in that size range. Schwefel [2011] found titanium sponge to absorb 60 ccSTP of reactive gases per gram of getter material with reasonably high absorption rates at operating temperatures of around 800°C. He developed a system for degassing of ice samples and for subsequent argon separation by gettering, which he successfully applied on alpine glacier ice.

In the context of using ^{85}Kr as indicator for atmospheric contamination of argon samples and employing ^{81}Kr or ^{85}Kr as age tracer, the feasibility of using the setup for argon separation also for krypton separation is currently investigated by Kersting [2013]. A krypton trap was installed and successfully tested. As the order of the gas peaks leaving the columns is Ar, O_2, Kr, and N_2, an additional oxygen trap is being built. This way it will be possible to obtain separate argon and krypton fractions from one sample in a single separation process. First tests of Kersting [2013] show that at the end of such a separation, the krypton of several tens of liters of air sample is contained in a few ccSTP of mixture of O_2 and N_2. The mixture can readily be purified with the getter setup developed by Schwefel [2011]. This may be an elegant alternative to the krypton separation by cryogenic distillation and subsequent gas chromatographic treatment as performed by Yokochi et al. [2008].

Another improvement of the setup for argon separation can be achieved by installation of some additional tube connections and a reservoir containing a calibration gas. Routine determination of the composition of the sample air degassed from groundwater would then be possible without great efforts and without sample gas losses.

Appendix A

Noble Gas Data

Sample	He	err He	Ne	err Ne	Ar	err Ar
HR 544255/1	5.99E-08	8E-10	2.34E-07	1E-09	4.23E-04	3E-06
HR 544255/2	5.95E-08	8E-10	2.35E-07	2E-09	4.22E-04	3E-06
HR 544259/1	1.83E-06	3E-08	2.76E-07	2E-09	4.93E-04	4E-06
HR 544259/2	1.82E-06	3E-08	2.75E-07	2E-09	4.90E-04	4E-06
HR 544264/1	5.94E-08	8E-10	2.41E-07	2E-09	4.08E-04	3E-06
HR 544264/2	3.51E-08	5E-10	1.64E-07	1E-09	3.67E-04	3E-06
Sample	Kr	err Kr	Xe	err Xe	^{3}He	err ^{3}He
HR 544255/1	1.00E-07	2E-09	1.29E-08	6E-10	9.11E-14	5E-15
HR 544255/2	9.73E-08	2E-09	1.29E-08	6E-10	8.91E-14	5E-15
HR 544259/1	1.16E-07	2E-09	1.49E-08	8E-10	7.02E-13	4E-14
HR 544259/2	1.16E-07	2E-09	1.57E-08	8E-10	6.87E-13	4E-14
HR 544264/1	9.39E-08	2E-09	1.23E-08	6E-10	2.30E-13	1E-14
HR 544264/2	8.96E-08	2E-09	1.26E-08	6E-10	1.83E-13	1E-14
Sample	^{3}He/^{4}He	err ^{3}He/^{4}He	^{20}Ne/^{22}Ne	err ^{20}Ne/^{22}Ne	^{40}Ar/^{36}Ar	err ^{40}Ar/^{36}Ar
HR 544255/1	1.52E-06	9E-08	9.79E+00	9E-02	3.07E+02	6E+00
HR 544255/2	1.50E-06	9E-08	9.77E+00	9E-02	2.95E+02	6E+00
HR 544259/1	3.85E-07	2E-08	9.76E+00	9E-02	2.93E+02	5E+00
HR 544259/2	3.77E-07	2E-08	9.79E+00	9E-02	2.86E+02	6E+00
HR 544264/1	3.87E-06	2E-07	9.91E+00	9E-02	2.81E+02	5E+00
HR 544264/2	5.23E-06	3E-07	9.79E+00	1E-01	3.19E+02	1E+01

Table A.1: The results of the noble gas measurements of the samples from the Hessisches Ried, performed with the MM5400 at the IUP Heidelberg (in ccSTP/g, except for ratios).

Sample	He	err He	Ne	err Ne	Ar	err Ar
SH F10/2	6.10E-08	9E-10	2.60E-07	1E-09	4.54E-04	4E-06
SH F10/3	6.89E-08	1E-09	2.56E-07	1E-09	4.36E-04	3E-06
SH F18/2	6.01E-08	6E-10	2.52E-07	2E-09	4.36E-04	3E-06
SH GOE15/2	6.26E-08	6E-10	2.45E-07	1E-09	4.32E-04	3E-06
SH GOE15/3	7.72E-08	8E-10	2.37E-07	2E-09	4.32E-04	3E-06
Sample	Kr	err Kr	Xe	err Xe	^{3}He	err ^{3}He
SH F10/2	1.05E-07	1E-09	1.49E-08	3E-10	1.02E-13	2E-15
SH F10/3	1.01E-07	1E-09	1.37E-08	3E-10	8.92E-14	2E-15
SH F18/2	1.01E-07	1E-09	1.42E-08	3E-10	2.03E-13	8E-15
SH GOE15/2	1.01E-07	1E-09	1.38E-08	3E-10	8.62E-14	3E-15
SH GOE15/3	1.02E-07	1E-09	1.42E-08	3E-10	8.32E-14	3E-15
Sample	^{3}He/^{4}He	err ^{3}He/^{4}He	^{20}Ne/^{22}Ne	err ^{20}Ne/^{22}Ne	^{40}Ar/^{36}Ar	err ^{40}Ar/^{36}Ar
SH F10/2	1.67E-06	5E-08	9.77E+00	5E-02	2.99E+02	6E+00
SH F10/3	1.30E-06	4E-08	9.79E+00	5E-02	2.99E+02	6E+00
SH F18/2	3.37E-06	1E-07	9.82E+00	1E-01	2.97E+02	5E+00
SH GOE15/2	1.38E-06	5E-08	9.80E+00	7E-02	2.95E+02	4E+00
SH GOE15/3	1.08E-06	4E-08	9.80E+00	1E-01	2.94E+02	5E+00

Table A.2: The results of the noble gas measurements of the samples from the Schwetzinger Hardt, performed with the MM5400 at the IUP Heidelberg (in ccSTP/g, except for ratios).

Sample	He3M	He3Merr	He4F	He4Ferr
SH F10/2 well water	1.02E-13	2E-15	6.10E-08	9E-10
SH F10/3 well water	8.92E-14	2E-15	6.89E-08	1E-09
SH F10/2 degassed water(1)	1.67E-14	5E-16	1.03E-08	1E-10
SH F10/2 degassed water(2)	1.47E-14	5E-16	9.55E-09	1E-10
SH F10/3 degassed water(1)	1.37E-14	4E-16	1.11E-08	2E-10
SH F10/3 degassed water(2)	1.33E-14	4E-16	1.10E-08	2E-10

Sample	Ne20F	Ne20Ferr	Ne22F	Ne22Ferr
SH F10/2 well water	2.35E-07	1E-09	2.41E-08	8E-11
SH F10/3 well water	2.32E-07	1E-09	2.37E-08	8E-11
SH F10/2 degassed water(1)	3.12E-08	1E-10	3.17E-09	1E-11
SH F10/2 degassed water(2)	2.92E-08	1E-10	2.97E-09	1E-11
SH F10/3 degassed water(1)	2.99E-08	1E-10	3.03E-09	1E-11
SH F10/3 degassed water(2)	2.90E-08	1E-10	2.95E-09	2E-11

Sample	Ar36F	Ar36Ferr	Ar40F	Ar40Ferr
SH F10/2 well water	1.51E-06	3E-08	4.52E-04	1E-06
SH F10/3 well water	1.45E-06	3E-08	4.34E-04	1E-06
SH F10/2 degassed water(1)	1.61E-07	4E-09	4.45E-05	1E-07
SH F10/2 degassed water(2)	-5.82E-09	-4E-09	4.09E-05	1E-07
SH F10/3 degassed water(1)	1.44E-07	4E-09	4.35E-05	1E-07
SH F10/3 degassed water(2)	1.43E-07	5E-09	4.15E-05	1E-07

Sample	Kr84M	Kr84Merr	Xe132M	Xe132Merr
SH F10/2 well water	5.99E-08	8E-10	4.01E-09	9E-11
SH F10/3 well water	5.77E-08	8E-10	3.67E-09	8E-11
SH F10/2 degassed water(1)	7.79E-09	1E-10	7.16E-10	2E-11
SH F10/2 degassed water(2)	6.97E-09	1E-10	6.59E-10	1E-11
SH F10/3 degassed water(1)	7.47E-09	1E-10	7.14E-10	2E-11
SH F10/3 degassed water(2)	7.28E-09	1E-10	6.70E-10	2E-11

Sample	Ne20F/Ne22F	Ne20F/Ne22Ferr	Ar40F/Ar36F	Ar40F/Ar36Ferr
SH F10/2 well water	9.78	0.004	297	2
SH F10/3 well water	9.79	0.004	296	2
SH F10/2 degassed water(1)	9.82	0.004	296	2
SH F10/2 degassed water(2)	9.81	0.004	296	2
SH F10/3 degassed water(1)	9.82	0.004	296	2
SH F10/3 degassed water(2)	9.83	0.005	294	2

Sample	Ar36F/Ar40F	Ar36F/Ar40Ferr	He4/He3	He4/He4err
SH F10/2 well water	3.34E-03	7E-05	6.0E+05	2E+04
SH F10/3 well water	3.34E-03	7E-05	7.7E+05	2E+04
SH F10/2 degassed water(1)	3.63E-03	9E-05	6.2E+05	2E+04
SH F10/2 degassed water(2)	-1.43E-04	9E-05	6.5E+05	2E+04
SH F10/3 degassed water(1)	3.30E-03	8E-05	8.1E+05	3E+04
SH F10/3 degassed water(2)	3.44E-03	1E-04	8.2E+05	3E+04

Table A.3: The results of the noble gas measurements of water degassed with the setup for water degassing, performed with the MM5400 at the IUP Heidelberg (in ccSTP/g, except for ratios).

Sample	He3M	He3Merr	He4F	He4Ferr
HR 544255 degassed air(1)	2.38E-13	7E-15	1.43E-07	2E-09
HR 544255 degassed air(2)	9.53E-13	3E-14	5.40E-07	7E-09
HR 544259 degassed air	2.10E-11	6E-13	5.03E-05	7E-07
HR 544264 degassed air	2.66E-11	1E-11	1.74E-05	2E-07
P4 degassed air	6.34E-12	2E-13	3.98E-06	5E-08
P5 degassed air(1)	2.37E-12	7E-14	1.61E-06	2E-08
P5 degassed air(2)	4.09E-12	1E-13	2.87E-06	4E-08
HR 544255 separated argon	3.45E-10	1E-11	1.95E-03	3E-05
HR 544259 separated argon	2.19E-10	6E-12	1.29E-03	2E-05
HR 544264 separated argon	8.64E-10	3E-11	5.45E-03	8E-05

Sample	Ne20F	Ne20Ferr	Ne22F	Ne22Ferr
HR 544255 degassed air(1)	5.76E-07	3E-09	5.88E-08	8E-10
HR 544255 degassed air(2)	2.03E-06	8E-09	2.08E-07	9E-10
HR 544259 degassed air	7.27E-06	3E-08	7.42E-07	2E-09
HR 544264 degassed air	5.49E-05	2E-07	5.60E-06	2E-08
P4 degassed air	1.55E-05	6E-08	1.59E-06	8E-09
P5 degassed air(1)	6.58E-06	3E-08	6.74E-07	2E-09
P5 degassed air(2)	1.11E-05	4E-08	1.13E-06	3E-09
HR 544255 separated argon	6.58E-07	3E-09	6.76E-08	8E-10
HR 544259 separated argon	3.75E-07	2E-09	3.78E-08	7E-10
HR 544264 separated argon	2.66E-06	1E-08	2.76E-07	1E-09

Sample	Ar36F	Ar36Ferr	Ar40F	Ar40Ferr
HR 544255 degassed air(1)	2.40E-05	6E-07	7.04E-03	4E-05
HR 544255 degassed air(2)	8.49E-05	1E-06	2.51E-02	1E-04
HR 544259 degassed air	4.97E-05	7E-07	1.45E-02	8E-05
HR 544264 degassed air	1.20E-04	2E-06	3.50E-02	2E-04
P4 degassed air	8.96E-05	1E-06	2.66E-02	2E-04
P5 degassed air(1)	3.82E-05	7E-07	1.08E-02	6E-05
P5 degassed air(2)	6.15E-05	8E-07	1.82E-02	1E-04
HR 544255 separated argon	1.58E-04	2E-06	4.50E-02	3E-04
HR 544259 separated argon	1.80E-04	2E-06	5.06E-02	3E-04
HR 544264 separated argon	1.84E-04	2E-06	5.12E-02	3E-04

Sample	Kr84M	Kr84Merr	Xe132M	Xe132Merr
HR 544255 degassed air(1)	1.38E-07	2E-09	9.08E-09	2E-10
HR 544255 degassed air(2)	4.85E-07	8E-09	2.80E-08	5E-10
HR 544259 degassed air	1.82E-06	3E-08	1.09E-07	2E-09
HR 544264 degassed air	2.79E-06	4E-08	1.13E-07	2E-09
P4 degassed air	3.33E-06	5E-08	1.65E-07	4E-09
P5 degassed air(1)	1.33E-06	2E-08	8.02E-08	2E-09
P5 degassed air(2)	2.22E-06	3E-08	1.33E-07	3E-09
HR 544255 separated argon	3.98E-09	6E-10	2.34E-11	5E-11
HR 544259 separated argon	6.12E-10	5E-10	-8.49E-11	-3E-11
HR 544264 separated argon	7.90E-09	5E-10	-2.74E-11	-3E-11

Table A.4: The results of the noble gas measurements of degassed air and separated argon, performed with the MM5400 at the IUP Heidelberg (in ccSTP).

Sample	Ne20F/Ne22F	Ne20F/Ne22Ferr	Ar40F/Ar36F	Ar40F/Ar36Ferr
HR 544255 degassed air(1)	9.80	0.006	295	1
HR 544255 degassed air(2)	9.80	0.005	295	1
HR 544259 degassed air	9.78	0.005	293	1
HR 544264 degassed air	9.80	0.005	296	1
P4 degassed air	9.77	0.005	296	1
P5 degassed air(1)	9.77	0.005	279	1
P5 degassed air(2)	9.78	0.005	296	1
HR 544255 separated argon	9.77	0.006	296	1
HR 544259 separated argon	9.96	0.006	297	1
HR 544264 separated argon	9.65	0.005	296	1

Sample	Ar36F/Ar40F	Ar36F/Ar40Ferr	He4/He3	He4/He4err
HR 544255 degassed air(1)	3.39E-03	1E-05	6.0E+05	2E+04
HR 544255 degassed air(2)	3.39E-03	1E-05	5.7E+05	2E+04
HR 544259 degassed air	3.42E-03	1E-05	2.4E+06	8E+04
HR 544264 degassed air	3.38E-03	1E-05	6.5E+05	2E+05
P4 degassed air	3.38E-03	1E-05	6.3E+05	2E+04
P5 degassed air(1)	3.59E-03	1E-05	6.8E+05	2E+04
P5 degassed air(2)	3.37E-03	1E-05	7.0E+05	2E+04
HR 544255 separated argon	3.38E-03	1E-05	5.7E+06	2E+05
HR 544259 separated argon	3.37E-03	1E-05	5.9E+06	2E+05
HR 544264 separated argon	3.38E-03	1E-05	6.3E+06	2E+05

Table A.5: The continuation of the results of the noble gas measurements of degassed air and separated argon, performed with the MM5400 at the IUP Heidelberg.

Bibliography

[Aeschbach-Hertig 2004]   AESCHBACH-HERTIG, W.: Solubility of gases in water (internal document). (2004)

[Aeschbach-Hertig 2012]   AESCHBACH-HERTIG, W.: Bericht zu isotopenhydrologischen Untersuchungen im Gebiet des Wasserwerkes Schwetzinger Hardt für den Zweckverband Wasserversorgung Kurpfalz. (2012)

[Aeschbach-Hertig et al. 2002]   AESCHBACH-HERTIG, W. ; BEYERLE, U. ; HOLOCHER, J. ; PEETERS, F. ; KIPFER, R.: Excess air in groundwater as a potential indicator of past environmental changes. *Study of Environmental Change Using Isotope Techniques, C& S PapersSeries 13, IAEA Vienna* (2002), 174–183

[Aeschbach-Hertig et al. 2008]   AESCHBACH-HERTIG, W. ; EL-GAMAL, H. ; WIESER, M. ; PALCSU, L.: Modeling excess air and degassing in groundwater by equilibrium partitioning with a gas phase. *Water Resources Research* 44 (2008), W08449

[Aeschbach-Hertig et al. 1999]   AESCHBACH-HERTIG, W. ; PEETERS, F. ; BEYERLE, U. ; KIPFER, R.: Interpretation of dissolved atmospheric noble gases in natural waters. *Water Resources Research* 35 (1999), No. 9, 2279–2792

[Aeschbach-Hertig and Solomon 2013]   AESCHBACH-HERTIG, W. ; SOLOMON, D. K.: Noble Gas Thermometry In Groundwater Hydrology. BURNARD, P. (Ed.): *The Noble Gases as Geochemical Tracers.* Berlin Heidelberg : Springer, 2013 (Advances in Isotope Geochemistry), 81–122

[Andrews et al. 1989]   ANDREWS, J. N. ; DAVIS, S. N. ; FABRYKA-MARTIN, J. ; FONTES, J-Ch. ; LEHMANN, B. E. ; LOOSLI, H. H. ; MICHELOT, J-L. ; MOSER, H. ; SMITH, B. ; WOLF, M.: The in situ production of radioisotopes in rock matrices with particular reference to the Stripa granite. *Geochimica et Cosmochimica Acta* 53 (1989), 1803–1815

[Bender et al. 2008]   BENDER, M. L. ; BARNETT, B. ; DREYFUS, G. ; PORCELLI, D.: The contemporary degassing rate of ^{40}Ar from the solid Earth. *Proc. Natl. Acad. Sci. USA* 105 (2008), No. 24, 8232–8237

[Benson and Krause Jr. 1980]   BENSON, B. B. ; KRAUSE JR., D.: Isotopic Fractionation of Helium During Solution: A Probe for the Liquid State. *Journal of Solution Chemistry* 9 (1980), No. 12, 895–909

[Beyerle et al. 2000]   BEYERLE, U. ; AESCHBACH-HERTIG, W. ; IMBODEN, D. M. ; BAUR, H. ; GRAF, T. ; KIPFER, R.: A Mass Spectrometric System for the Analysis of Noble Gases and Tritium from Water Samples. *Environ. Sci. Technol.* 34 (2000), 2042–2050

[Bourg 2008]   BOURG, G.: Isotopic fractionation of noble gases by diffusion in liquid water: Molecular simulations and hydrologic applications. *Geochimica et Cosmochimica Acta* 72 (2008), No. 9, 2237–2247

[Buck 1981]   BUCK, A. L.: New Equations for Calculating Vapor Pressure and Enhancement Factor. *Journal of Applied Meteorology* 20 (1981), 1527–1532

[Cey 2009]   CEY, B. D.: On the accuracy of noble gas recharge temperatures as a paleoclimate proxy. *Journal of Geophysical Research* 114 (2009), D04107

[Chakraborty et al. 2006]   CHAKRABORTY, A. ; SAHA, B. B. ; KOYAMA, S. ; NG, K. C.: On the thermodynamic modeling of the isosteric heat of adsorption and comparison with experiments. *Appl. Phys. Lett* 89 (2006). – id. 171901

[Chen et al. 1999]   CHEN, C. Y. ; LI, Y. M. ; BAILEY, K. ; O´CONNOR, P. O. ; YOUNG, L. ; LU, Z.-T.: Ultrasensitive Isotope Analysis with a Magneto-Optical Trap. *Science* 286 (1999), 1139–1141

[Clever 1979]   CLEVER, H. L.: *Krypton, xenon, and radon - gas solubilies.* Oxford : Pergamon Press, 1979

[Collon et al. 2004]   COLLON, P. ; BICHLER, M. ; CAGGIANO, J. ; DEWAYNE CECIL, L. ; MASRI, Y. E. ; GOLSER, R. ; JIANG, C. L. ; HEINZ, A. ; HENDERSON, D. ; KUTSCHERA, W. ; LEHMANN, B. E. ; LELEUX, P. ; LOOSLI, H. H. ; PARDO, R. C. ; PAUL, M. ; REHM, K. E. ; SCHLOSSER, P. ; SCOTT, R. H. ; SMETHIE JR., W. M. ; VONDRSEK, R.: Development of an AMS method to study oceanic circulation characteristics using cosmogenic ^{39}Ar. *Nuclear Instruments and Methods in Physics Research Section B: Beam Interaxtions with Materials and Atoms* 223 (2004), 428–434

[Corcho Alvarado et al. 2009]   CORCHO ALVARADO, J. A. ; BARBECOT, F. ; PURTSCHERT, R. ; GILLON, M. ; AESCHBACH-HERTIG, W. ; KIPFER, R.: European climate variations over the past half-millennium reconstructed from groundwater. *Geophysical Research Letters* 36 (2009), L15703

[Corcho Alvarado et al. 2011]   CORCHO ALVARADO, J. A. ; LEUENBERGER, M. ; KIPFER, R. ; PACES, T. ; PURTSCHERT, R.: Reconstruction of past climate conditions over central Europe from groundwater data. *Quaterny Science Reviews* 30 (2011), 3423–3429

[Corcho Alvarado et al. 2007]   CORCHO ALVARADO, J. A. ; PURTSCHERT, R. ; BARBECOT, F. ; CHABAULT, C. ; RUEEDI, J. ; SCHNEIDER, V. ; AESCHBACH-HERTIG, W. ; KIPFER, R. ; LOOSLI, H. H.: Constraining the age distribution of highly mixed groundwater using ^{39}Ar: A multiple environmental tracer (^{3}H/^{3}He, ^{85}Kr, ^{39}Ar, and ^{14}C) study in the semiconfined Fontainebleau Sands Aquifer (France). *Water Resources Research* 43 (2007), W03427

[Cussler 2005]   CUSSLER, E. L.: *Diffusion - Mass Transfer in Fluid Systems.* Cambridge : Cambridge University Press, 2005

[DIC Corporation, 2007]   DIC CORPORATION,: *Separel PF-F Series.* Chuo-Ku Tokyo, 2007.
– document "D60 Rev 9 03/06"

[Do 1998]   DO, D. D.: *Series on Chemical Engineering.* Vol. 2: *Adsorption Analysis: Equilibria and Kinetics.* London : Imperial College Press, 1998

[Dockweiler AG, 1993]   DOCKWEILER AG,: *Rohrbogen - DN 2605 R.* 19306 Neustadt-Glewe, 1993

[Dockweiler AG, 2009]   DOCKWEILER AG,: *Personal Communication.* 19306 Neustadt-Glewe, 2009

[Ebser 2012]   EBSER, S.: *Optimierung und Stabilisierung von ^{39}Ar-ATTA bis hin zur erstmaligen Anwendung auf die Datierung natürlicher Wasserproben*, University Heidelberg, Diploma Thesis, 2012

[Ettre et al. 1996]   ETTRE, L. S. ; HINSHAW, J. V. ; ROHRSCHNEIDER, L.: *Grundbegriffe und Gleichungen der Gaschromatographie.* Heidelberg : Hüthig Verlag, 1996

[Famiglietti et al. 2011]   FAMIGLIETTI, J. S. ; LO, M. ; HO, S. L. ; BETHUNE, J. ; ANDERSON, K. J. ; SYED, T. H. ; SWENSON, S. C. ; LINAGE, C. R. de ; RODELL, M.: Satellites measure recent rates of groundwater depletion in California´s Central Valley. *Geophysical Research Letters* 38 (2011), February, No. Issue 3

[Feng et al. 2013]   FENG, W. ; ZHONG, M. ; LEMOINE, J.-M. ; BIANCALE, R. ; HSU, H.-T. ; XIA, J.: Evaluation of groundwater depletion in North China using Gravity Recovery and Climate Experiment (GRACE) data and ground-based measurements. *Water Resour. Res.* 49 (2013)

[Florkowski and Rozanski 1986]   FLORKOWSKI, T. ; ROZANSKI, K.: Radioactive Noble Gases in the Terrestrial Environment. FRITZ, P. (Ed.) ; FONTES, J.-Ch. (Ed.): *Handbook of Environmental Geochemistry* Vol. 2b. New York : Elsevier Science, 1986, 481–506

[Forster et al. 1983]   FORSTER, M. ; MOSER, M. ; LOOSLI, H. H.: Isotope hydrological study with carbon-14 and argon-39 in the bunter sandstone of the Saar region. *Isotope Hydrology* 270 (1983), No. 29, 515–533

[Friedrich 2007]   FRIEDRICH, R.: *Grundwassercharakterisierung mit Umwelttracern: Erkundung des Grundwassers der Odenwald-Region sowie Implementierung eines neuen Edelgas-Massenspektrometersystems*, University Heidelberg, Dissertation, 2007

[Galbiati et al. 2008]   GALBIATI, C. ; ACOSTA-KANE, D. ; ACCIARRI, R. ; AMAIZE, O. ; ANTONELLO, M. ; BAIBUSSINOV, B. ; CEOLIN, M. B. ; BALLENTINE, C. J. ; BANSAL, R. ; BASGALL, L. ; BAZARKO, A. ; BENETTI, P. ; BENZIGER, J. ; BURGERS, A. ; CALAPRICE, F. ; CALLIGARICH, E. ; CAMBIAGHI, M. ; CANCI, N. ; CARBONARA, F. ; CASSIDY, M. ; CAVANNA, F. ; CENTRO, S. ; CHAVARRIA, A. ; CHENG, D. ; COCCO, A. G. ; COLLON, P. ; DALNOKI-VERESS, P. ; HAAS, E. de ; DI POMPEO, F. ; FIORILLO, G. ; FITCH, F. ; GALLO, V. ; GAULL, M. ; GAZZANA, S. ; GRANDI, L. ; GORETTI, A. ; HIGHFILL, R. ; HIGHFILL, T. ; HOHMAN, T. ; IANNI, A. ; IANNI, A. ; LACAVA, A. ; LAUBENSTEIN, M. ; LEE, H. Y. ; LEUNG, M. ; LOER, B. ; LOOSLI, H. H. ; LYONS, B. ; MARKS, D. ; McCARTY, K. ; MENG, G. ; MONTANARI,

C. ; Mukhopadhyay, S. ; Nelson, A. ; Palamara, O. ; Pandola, L. ; Pietropaolo, F. ; Pivonka, T. ; Pocar, A. ; Purtschert, R. ; Rappoldi, A. ; Raselli, G. ; Resnati, F. ; Robertson, D. ; Roncadelli, M. ; Rossella, M. ; Rubbia, C. ; Ruderman, J. ; Saldanha, R. ; Schmitt, C. ; Scott, R. ; Segreto, E. ; Shirley, A. ; Szelc, A. M. ; Tartaglia, R. ; Tesileanu, T. ; Ventura, S. ; Vignoli, C. ; Visnjic, C. ; Vondrasek, R. ; Yushkov, A.: Discovery of underground argon with low level of radioactive ^{39}Ar and possible applications to WIMP dark matter detectors. *Nuclear Instruments and Methods in Physics Research A* 587 (2008), 46–51

[Gerthsen et al. 1977]   Gerthsen, C. ; Kneser, H. O. ; Vogel, H.: *Physik: ein Lehrbuch zum Gebrauch neben Vorlesungen.* Berlin Heidelberg New York : Springer-Verlag, 1977

[Gill 1982]   Gill, A. E.: *Atmosphere - Ocean Dynamics.* New York : Academic Press, 1982

[Grob 1995]   Grob, R. L.: *Modern practice of gas chromatography.* New York : Wiley, 1995

[Hach Company, 2006]   Hach Company,: *Hydrolab DS5X, DS5, and MS5 Water Quality Multiporbes - User Manual.* Loveland, CO, 2006

[HGK 1999]   HGK: *Hydrogeologische Kartierung und Grundwasserbewirtschaftung Rhein-Neckar-Raum, Fortschreibung 1983 - 1998.* Stuttgart Wiesbaden Mainz : Ministerium für Umwelt und Verkehr Baden-Württemberg, Hessisches Ministerium für Umwelt, Landwirtschaft und Forsten, Ministerium für Umwelt und Forsten Rheinland-Pfalz, 1999

[Illies 1977]   Illies, J.H.: Ancient and recent rifting in the Rhinegraben. Frost, R. T. C. (Ed.) ; Dikkers, A. J. (Ed.): *Fault tectonics in N.W. Europe* Vol. 56. Utrecht : Netherlands Journal of Geosciences, 1977, 329–350

[Infiltec GmbH, 2010a]   Infiltec GmbH,: *Datenblatt zu CAUSAPURE Tiefenfilterkerzen.* D 67346 Speyer, 2010

[Infiltec GmbH, 2010b]   Infiltec GmbH,: *Datenblatt zu CAUSAPURE Tiefenfilterkerzen.* D 67346 Speyer, 2010

[Infiltec GmbH, 2010c]   Infiltec GmbH,: *Datenblatt zu Kunststoff-Filtergehäuse Causa Typ PP-Blue.* D 67346 Speyer, 2010

[IUPAC 2001]   IUPAC: Retention Parameters in Chromatography (IUPAC Recommendations 2001). *Pure Appl. Chem.* 73 (2001), No. 6, 969–992

[Jähne et al. 1987]   Jähne, B. ; Heinz, G. ; Dietrich, W.: Measurement of Diffusion Coefficients of Sparingly Soluble Gases in Water. *Journal of Geophysical Research* 92 (1987), No. C10, 10767–10776

[Jiang et al. 2011]   Jiang, W. ; Williams, W. ; Bailey, K. ; Davis, A. M. ; Hu, S.-M. ; Lu, Z.-T. ; O´Connor, T. P. ; Purtschert, R. ; Sturchio, N. C. ; Sun, Y. R. ; Mueller, P.: ^{39}Ar Detection at the 10^{-16} Isotopic Abundance Level with Atom Trap Trace Analysis. *Phys. Rev. Lett* 106 (2011), No. Issue 10, 103001–1–103001–4

[Jousten 2005]   Jousten, K.: *Wutz Handbuch Vakuumtechnik.* Wiesbaden : Vieweg+Teubner, 2005

[Jung et al. 2013]   JUNG, M. ; WIESER, M. ; OEHSEN, A. von ; AESCHBACH-HERTIG, W.: Properties of the closed-system equilibration model for dissolved noble gases in groundwater. *Chem. Geol.* 339 (2013), 291–300

[Kartohardjono and Chen 2005]   KARTOHARDJONO, S. ; CHEN, V.: Mass Transfer and Fluid Hydrodynamics in Sealed End Hydrophobic Hollow Fiber Membrane Gas-liquid Contactors. *J. Applied Membrane Science & Technology* 2 (2005), 1–12

[Keller and Staudt 2005]   KELLER, J. U. ; STAUDT, R.: *Gas Adsorptiom Equilibria - Experimental Methods and Adsorptive Isotherms.* Boston : Springer Science + Business Media, Inc, 2005

[Kersting 2013]   KERSTING, A.: *Personal Communication.* Heidelberg : Institute of Environmental Physics, 2013

[Keulemans and Cremer 1959]   KEULEMANS, A. I. M. ; CREMER, E.: *Gas-Chromatographie.* Weinheim an der Bergstraße : Verlag Chemie, 1959

[KNF Neuberger GmbH, 2008]   KNF NEUBERGER GMBH,: *Datenblatt D030.* D 79112 Freiburg, 2008

[KNF Neuberger GmbH, 2009]   KNF NEUBERGER GMBH,: *Datenblatt D059.* D 79112 Freiburg, 2009

[Kollefrath 2011]   KOLLEFRATH, A.: *Test einer Entgasungsanlage*, University Heidelberg, Bachelor Thesis, 2011

[Krieger 2011]   KRIEGER, C.: *Personal Communication.* Wiesbaden : Hessisches Landesamt für Umwelt und Geologie, 2011

[Kurzhals 2009]   KURZHALS, R.: *Personal Communication.* Bitterfeld : Süd Chemie Zeolites GmbH, 2009

[Langmuir 1918]   LANGMUIR, I.: The Adsorption of gases on plane surfaces of glass, mica and platinum. *Journal of the American Chemical Society* 40 (1918), 1361–1403

[Lehmann and Purtschert 1997]   LEHMANN, B. E. ; PURTSCHERT, R.: Radioisotope dynamics - the origin and the fate of nuclides in groundwater. *Applied Geochimistry* 12 (1997), 727–738

[Loosli 1983]   LOOSLI, H. H.: A dating method with ^{39}Ar. *Earth and Planetary Science Letters* 63 (1983), 51–62

[Loosli 1989]   LOOSLI, H. H.: Argon-39: A Tool to Investigate Ocean Water Circulation and Mixing. FRITZ, P. (Ed.) ; FONTES, J. C. (Ed.): *Handbook of Environmental Isotope Chemistry: The Marine Environment, A* Vol. 3. Amsterdam : Elsevier, 1989, 385–392

[Loosli 1992]   LOOSLI, H. H.: Applications of ^{37}Ar, ^{39}Ar and ^{85}Kr in hydrology, oceanography and atmospheric studies: Current state of the art. *Isotopes of Noble Gases as Tracers in Environmental Studies* (1992), 75–84

[Loosli et al. 1989]   Loosli, H. H. ; Lehmann, B. E. ; Balderer, W.: Argon-39, argon-37 and krypton-85 isotopes in Stripa groundwaters. *Geochimica et Cosmochimica Acta* 53 (1989), 1825–1829

[Loosli et al. 2001]   Loosli, H.H. ; Aeschbach-Hertig, W. ; Barbecot, F. ; Blaser, P. ; W.G., Darling ; Dever, L. ; Edmunds, W.M. ; Kipfer, R. ; Purtschert, R. ; Walraevens, K.: Isotopic methods and their hydrogeochemical context in the investigation of palaeowaters. Edmunds, W.M. (Ed.) ; Milne, C.J (Ed.): *Palaeowaters of Coastal Europe: Evolution of Groundwater Since the Late Pleistocene.* London : Geological Society, 2001, 193–212

[Lu et al. 2012]   Lu, Z.-T. (Ed.) ; Schlosser, P. (Ed.) ; Smethie, W. (Ed.) ; Sturchio, N. (Ed.): *Tracer Applications of Noble Gas Radionuclides in the Geosciences.* 2012

[Lu and Wendt 2003]   Lu, Z.-T. ; Wendt, K. D. A.: Laser-based methods for ultrasensitive trace-isotope analyses. *Review of Scienticfic Instruments* (2003), 1169–1179

[Melin and Rautenbach 2007]   Melin, T. ; Rautenbach, R.: *Membranverfahren.* Berlin : Springer, 2007

[Membrana 2007a]   Membrana: *10 x 28 EXTRA-FLOW PRODUCT DATA SHEET.* Charlotte, 2007. – document "D61 Rev18 10x28 07-07"

[Membrana 2007b]   Membrana: *4 x 28 EXTRA-FLOW PRODUCT DATA SHEET.* Charlotte, 2007. – document "D60 Rev 9 03/06"

[Membrana 2007c]   Membrana: *6 x 28 EXTRA-FLOW PRODUCT DATA SHEET.* Charlotte, 2007. – document "D67 Rev.12 09-06)"

[Membrana 2012]   Membrana: *Design & Operation Guidelines for Liqui-Cel Extra-Flow Membrane Contactors.* Charlotte, 2012. – document "OP151-Rev.15 Operating Procedures"

[Miller et al. 1987]   Miller, G. W. ; Knaebel, K. S. ; Ikels, K. G.: Equilibria of Nitrogen, Oxygen, Argon and Air in Molecular Sieve 5A. *AIChE Journal* 33 (1987), No. 2, 194–201

[Möller 2003]   Möller, D.: *Luft: Chemie, Physik, Biologie, Reinhaltung, Recht.* Berlin : Walter de Gruyter, 2003

[Mook and de Vries 2001]   Mook, W. G. ; Vries, J. J. de: Introduction: Theory, Methods, Review. Mook, W. G. (Ed.): *Environmental Isotopes in the Hydrological Cylce – Principles and Applications* Vol. I. Vienna : IAEA, 2001, 125–142

[Newman et al. 2010]   Newman, B. D. ; Osenbrück, K. ; Aeschbach-Hertig, W. ; Solomon, K. D. ; Cook, P. ; Rozanski, K. ; Kipfer, R.: Dating of 'young' groundwaters using environmental tracers: advantages, applications, and research needs. *Isotopes in Environmental and Health Studies* 46 (2010), No. 3, 259–278

[Nolte et al. 2006]   Nolte, E. ; Rühm, W. ; Loosli, H. H. ; Tolstikhin, I. ; Kato, K. ; Huber, T. C. ; Egbert, S. D.: Measurements of fast neutrons in Hiroshima by use of ^{39}Ar. *Radiat. Environ. Biophys.* 44 (2006), 261–271

[Ohta et al. 2009]   OHTA, T. ; MAHARA, Y. ; MOMOSHIMA, N. ; INOUE, F. ; SHIMADA, J. ; IKAWA, R. ; TANIGUCHI, M.: Separation of dissolved Kr from a water sample by means of a hollow fiber membrane. *Journal of Hydrology* 376 (2009), September, 152–158

[Peng et al. 2008]   PENG, Z. G. ; LEE, S. H. ; ZHOU, T. ; SHIEH, J. J. ; CHUNG, T. S.: A study on pilot-scale degassing by polypropylene (PP) hollow fiber membrane contactors. *Desalination* 234 (2008), No. 1, 316–322

[Peter et al. 2011]   PETER, S. A. ; MOHARIR, A. S. ; JASRA, R. V.: Sr^{2+} Exchanged Zeolite X as an Adsorbent Material for Chromatoghraphic Separation of Argon-Oxgyen Gaseous Mixture. *Separation Science and Technology* 46 (2011), No. 3, 500–506

[Peters 2007]   PETERS, G.: *Active tectonics in the Upper Rhine Graben - Integration of paleoseismology, geomorphology and geomechanical modeling*, Vrije Universiteit Amsterdam, Dissertation, 2007

[Porcelli et al. 2002]   PORCELLI, D. ; BALLENTINE, C. ; WIELER, R.: *Rev. Mineral. Geochem..* Vol. 47: *Noble gases in geochemistry and cosmochemistry.* Washington, DC : Mineralogical Society of America, Geochemical Society, 2002

[Probst 2007]   PROBST, R.and Sturchio N. C.: Method for Extraction of Dissolved Gases from Groundwater for Radiokrypton Analysis, 2007, 69–70

[Purtschert 2013]   PURTSCHERT, R.: *Personal Communication.* Bern : University Bern, 2013

[Purtschert et al. 2001]   PURTSCHERT, R. ; BEYERLE, U. ; AESCHBACH-HERTIG, W. ; KIPFER, R. ; LOOSLI, H.H.: Paleowaters from the Glatt Valley, Switzerland. EDMUNDS, W.M. (Ed.) ; MILNE, C.J (Ed.): *Palaeowaters of Coastal Europe: Evolution of Groundwater Since the Late Pleistocene.* London : Geological Society, 2001, 193–212

[Reichel 2009]   REICHEL, T.: *Optimierung eines Verfahrens zur Radonmessung in Wasser*, University Heidelberg, Diploma Thesis, 2009

[Reitzel 2010]   REITZEL, T.: *Personal Communication.* D 79112 Freiburg : KNF Neuberger GmbH, 2010

[Richardt 2009]   RICHARDT, K.: *Personal Communication.* Puchheim : Gardner Denver Thomas GmbH, 2009

[Riedmann 2011]   RIEDMANN, R. A.: *Separation of Argon from atmospheric air and Measurements of ^{37}Ar for CTBT purposes*, University Bern, Dissertation, 2011

[Rodell et al. 2009]   RODELL, M. ; VELICOGNA, I. ; FAMIGLIETTI, J. S.: Satellite-based estimates of groundwater depletion in India. *Nature* 460 (2009), 999–1002

[Rossweiner GmbH & Co. oHG,]   ROSSWEINER GMBH & CO. OHG,: *Wohnungswasserzähler Typ ETK/ETW Modularis*

[Ruthven 2006]   RUTHVEN, D. M.: Fundamentals of Adsorption Equilibrium and Kinetics in Microporous Solids. KARGE, H. G. (Ed.) ; WEITKAMP, J. (Ed.): *Adsorption and Diffusion* Vol. 7. Berlin Heidelberg : Springer, 2006, 1–18

[Sano et al. 2013]   SANO, Y. ; MARTY, M. ; BURNARD, P.: Noble Gases in the Atmosphere. BURNARD, P. (Ed.): *The Noble Gases as Geochemical Tracers.* Berlin Heidelberg : Springer, 2013 (Advances in Isotope Geochemistry), 17–24

[Schäfer 2009]   SCHÄFER, S.: *Personal Communication.* Heidelberg, 2009

[Schlosser et al. 1995]   SCHLOSSER, P. ; BÖNISCH, G. ; KROMER, B. ; LOOSLI, H. H. ; BÜHLER, R. ; BAYER, R. ; BONANI, G. ; KOLTERMANN, K. P.: Mid-1980s distribution of tritium, ^{3}He, ^{14}C and ^{39}Ar in the Greenland/Norwegian Seas and the Nansen Basin of the Arctic Ocean . *Prog. Oceanog.* 35 (1995), 1–28

[Schlosser et al. 1994]   SCHLOSSER, P. ; KROMER, B. ; WEPPERNIG, R. ; LOOSLI, H. H. ; BAYER, R. ; BONANI, G. ; SUTER, M.: The distribution of ^{14}C and ^{39}Ar in the Weddell Sea. *Journal of Geophysical Research* 99 (1994), No. C5, 10275–10287

[Schwefel 2011]   SCHWEFEL, R.: *Methoden zur Probenaufbereitung von Eis- und Grundwasser- proben zur ^{39}Ar-Datierung mittels "atom trap trace analysis"*, University Heidelberg, Diploma Thesis, 2011

[Simgen 2003]   SIMGEN, H.: *Hochempfindlicher Nachweis radioaktiver Edelgasnuklide und natürlicher Radionuklide aus der Uran-Zerfallsreihe*, University Heidelberg, Dissertation, 2003

[Sing et al. 1985]   SING, K. S. W. ; EVERETT, D. H. ; HAUL, R. A. W. ; MOSCOU, L. ; PIEROTTI, R. A. ; ROUQUEROL, J. ; SIEMIENIEWSK, T.: Reporting Physisorption Data for Gas/Solid Systems with Special Reference to the Determination of Surface Area and Porosity. *Pure and Applied Chemistry* 57 (1985), No. 4, 603–619

[Sips 1948]   SIPS, R.: On the Structure of a Catalyst Surface. *J. Chem. Phys.* 16 (1948), No. 5, 490–495

[Sültenfuss et al. 2011]   SÜLTENFUSS, J. ; PURTSCHERT, R. ; FÜHRBÖTER, J.: Age structure and recharge conditions of a coastal aquifer (northern Germany) investigated with ^{39}Ar, ^{14}C, ^{3}H, He isotopes and Ne. *Hydrogeology Journal* 19 (2011), 221–236

[Stanojevic et al. 2003]   STANOJEVIC, M. ; LAZAREVIC, B. ; RADIC, D.: Review of membrane contactors designs and applications of different modules in industry. *FME Transactions* 31 (2003), No. 2, 91–98

[Sturchio et al. 2004]   STURCHIO, N. C. ; DU, X. ; PURTSCHERT, R. ; LEHMANN, B. E. ; SULTAN, M. ; PATTERSON, L. J. ; LU, Z.-T. ; MÜLLER, P. ; BIGLER, T. ; BAILEY, K. ; O´CONNOR, T. P. ; YOUNG, L. ; LORENZO, R. ; BECKER, R. ; EL ALFY, Z. ; EL KALIOUBY, B. ; DAWOOD, Y. ; ABDALLAH, M. A.: One million year old groundwater in the Sahara revealed by krypton-81 and chlorine-36. *Geophysical Research Letters* 31 (2004), L05503

[Sun et al. 2010]   SUN, T. ; HALL, M. ; CASTRO, M. C.: Statistical properties of groundwater noble gas paleoclimate models: Are they robust and unbiased estimators? *Geochem. Geophys. Geosyst.* 11 (2010), Q02002

[Ulbricht, R. 2009]   ULBRICHT, R.: *Personal Communication.* Charlotte : Membrana, 2009

[Vogel 1967]   VOGEL, J. C.: Investigation of groundwater with Radiocarbon. *Isotopes in Hydrology, International Atomic Energy Agency* (1967), 355–368

[Vogel 1970]   VOGEL, J. C.: Carbon-14 dating of groundwater. *Isotopes in Hydrology, International Atomic Energy Agency* (1970), 225–240

[von Holzen, W. 2009]   VON HOLZEN, W.: *Personal Communication.* Uetikon, Switzerland : Zeochem AG, 2009

[Voss et al. 2013]   VOSS, K. A. ; FAMIGLIETTI, J. S. ; LO, M. ; LINAGE, C. de ; RODELL, M. ; SWENSON, S. C.: Groundwater depletion in the Middle East from GRACE with implications for transboundary water management in the Tigris-Euphrates-Western Iran region. *Water Resour. Res.* 49 (2013), 904–914

[Weiss 1970]   WEISS, R. F.: The solubility of nitrogen, oxygen and argon in water and seawater. *Deep-Sea Research* 17 (1970), 721–735

[Weiss 1971]   WEISS, R. F.: Solubility of Helium and Neon in Water and Seawater. *Journal of Chemical and Engineering Data* 16 (1971), No. 2, 235–241

[Weiss and Kyser 1978]   WEISS, R. F. ; KYSER, T. K.: Solubility of Krypton in Water and Seawater. *Journal of Chemical and Engineering Data* 32 (1978), No. 1, 69–72

[Welte 2011]   WELTE, J.: *Atom Trap Trace Analysis of ^{39}Ar*, University Heidelberg, Dissertation, 2011

[Welte et al. 2010]   WELTE, J. ; RITTERBUSCH, F. ; STEINKE, I. ; HENRICH, M. ; AESCHBACH-HERTIG, W. ; OBERTHALER, M. K.: Towards the realization of atom trap btrace analysis for ^{39}Ar. *New Journal of Physics* 12 (2010), 065031

[Welte et al. 2009]   WELTE, J. ; STEINKE, I. ; HENRICH, M. ; RITTERBUSCH, F. ; OBERTHALER, M. K. ; AESCHBACH-HERTIG, W. ; SCHWARZ, W. H. ; TRIELOFF, M.: Hyperfine spectroscopy of the $1s_5$-$2p_9$ transistion of ^{39}Ar. *Review of Scientific Instruments* 80:113109 (2009)

[Wieser 2010]   WIESER, M.: *Imprints of climatic and environmental change in a regional aquifer system in an arid part of India using noble gases and other environmental tracers*, University Heidelberg, Dissertation, 2010

[Wiesler 1996]   WIESLER, F.: Membranes, Membrane Contactors: An Introduction to the Technology. *Ultrapure Water* (1996), May/June, 28–31

[WIKA Alexander Wiegand SE & Co. KG, 2009a]   WIKA ALEXANDER WIEGAND SE & CO. KG,: *Druckmessumformer für allgemeine industrielle Anwendungen Typ A-10.* D 63911 Klingenberg, 2009. – document "WIKA Datenblatt PE 81.60"

[WIKA Alexander Wiegand SE & Co. KG, 2009b]   WIKA ALEXANDER WIEGAND SE & CO. KG,: *Widerstandsthermometer Typ TR30, Kompaktausführung.* D 63911 Klingenberg, 2009. – document "WIKA Datenblatt TE 60.30"

[Wonneberger 2008]   WONNEBERGER, A.: *Novel Methods of Water Sample Preparation for ^{39}Ar Analysis*, University Heidelberg, Diploma Thesis, 2008

[WTW GmbH & Co. KG, 2002]   WTW GmbH & Co. KG,: *CellOx325 Operating manual.* D Weilheim, 2002

[Yang 2003]   Yang, R. T.: *Adsorbents - Fundamentals and Applications.* Hoboken, New Jersey : John Wiley and Sons, Inc, 2003

[Yokochi et al. 2008]   Yokochi, R. ; Heraty, L. J. ; Sturchio, N. C.: Method for Purification of Krypton from Environmental Samples for Analysis of Radiokrypton Isotopes. *Analyical Chemistry* 80 (2008), No. 22, 8688–8693

[Zuber et al. 2011]   Zuber, A. ; Rozanski, K. ; Kania, J. ; Purtschert, R.: On some methodological problems in the use of environmental tracers to estimate hydrogeologic parameters and to calibrate flow and transport models. *Hydrogeology Journal* 19 (2011), 53–69

Acknowledgements

I am deeply indebted to many people who contributed either directly or indirectly to the successful outcome of this work.

I owe my special thanks to my first PhD advisor Prof. Werner Aeschbach-Hertig who enabled this research project and allowed for independently working towards designated targets. He always found time for discussing results and targets, although having an overfull schedule. The supervision was rather guidance than monitoring and his advice were always insightful. I greatly appreciate the enjoyable climate in his working group, encouraging teamwork and exchange of ideas.

Furthermore, I want to thank the head of the ATTA group Heidelberg and my second PhD advisor Prof. Markus K. Oberthaler for the enjoyable group meetings and discussions in his office, and for always pushing the Heidelberg ATTA collaboration to new targets.

Also, I thank my second referee Prof. Augusto Mangini for assuming the assessment of this work and the hopefully coming fruitful discussions.

Moreover, I want to express my thanks and great esteem for the work of the institute´s workshop, who constructed the setup for water degassing and the setup for argon separation. I´m especially indebted to Heribert Sommer for his patience, always finding elegant solutions, all the delicate artifacts he manufactured, his interest, and for fixing the old alternating current generator.

I thank Robert Schwefel for having been the main discussion partner concerning the argon separation, for the assistance in the lab and in the field, for his easygoingness, and the encouragement.

Beyond, I owe my special thanks to Robin Riedmann and Roland Purtschert, who greatly hastened the development of the setup for argon separation by showing and explaining me the respective setup in Bern. I thank you for the good communication and the measurement of several ^{39}Ar samples.

I want to thank Tillmann Kaudse, Martin Wieser, Florian Freundt, and Tim Schneider for the help in the field and for introducing me to and helping me with the noble gas measurements. I particularly thank Tillmann Kaudse for proofreading of my thesis.

I thank Michael Jung for the introduction in his software for evaluation of noble gas data and for the enjoyable discussions in the lunch breaks.